The Pennsylvania State University

The Graduate School

Department of Energy and Geo-Environmental Engineering

NUMERICAL MODELING OF GAS RECOVERY FROM METHANE HYDRATE RESERVOIRS

A Thesis in

Petroleum and Natural Gas Engineering

by

Suntichai Silpngarmlert

Submitted in Partial Fulfillment
of the Requirements
for the Degree of

Doctor of Philosophy

May 2007

The thesis of Suntichai Silpngarmlert was reviewed and approved* by the following:

Turgay Ertekin
Program Chair and Professor of Petroleum and Natural Gas Engineering
George E. Trimble Chair in Earth and Mineral Sciences
Chair of Graduate Program
Thesis Co-Advisor
Co-Chair of Committee

Luis Ayala
Assistant Professor of Petroleum and Natural Gas Engineering
Thesis Co-Advisor
Co-Chair of Committee

Michael Adewumi
Professor of Petroleum and Natural Gas Engineering
Quentin E. and Louise L. Wood University Endowed Fellow in Petroleum and Natural Gas Engineering

Zuleima Karpyn
Assistant Professor of Petroleum and Natural Gas Engineering

Derek Elsworth
Professor of Energy and Geo-Environmental Engineering

*Signatures are on file in the Graduate School

ABSTRACT

Class 1 hydrate deposits are characterized by a hydrate bearing layer underlain by a two phase, free-gas and water, zone. A Class 1 hydrate reservoir is more preferable than class 2 and class 3 hydrate accumulations because a small change of pressure and temperature can induce hydrate dissociation. In this study, production characteristics from class 1 methane-hydrate reservoirs by means of conventional depressurization technique are studied. In this work, the production characteristics and efficiency from different production strategies (mainly focused on a constant bottom-hole pressure production scheme) such as well-completion locations, well spacing, and production scheduling are investigated.

In the production of conventional gas reservoirs using a constant bottom-hole pressure production scheme, both gas and water production rates exponentially decrease with time. However, for methane-hydrate reservoirs, gas production rate exponentially declines with time whereas water production rate increases with time because methane hydrate dissociation increases water saturation of the reservoir.

The effects of well-completion locations on the production performances are examined. The simulation results indicate that the moving well completion location strategy provides better gas production performance than the fixed completion location strategy. The optimum well-completion location (using a moving completion location strategy) is at the middle of free-gas zone. Due to the effects of hydrate saturation on formation permeability, one should not complete a well in the hydrate zone.

The effect of well spacing on the production efficiency is also investigated. As expected, smaller well-spacing system yields more total gas production and it can dissociate gas-hydrate more rapidly than the larger well-spacing system. However, the number of wells increases when the well-spacing decreases resulting in the increase of the capital investment of the project. Based on this study, when the well-spacing increased about 100 percent (from 45.0 acres to 74.38 acres) the cumulative gas production decreased about 8.4 percent at 1,000 days of production. Therefore, once the similar simulation study for a particular reservoir has been performed, the optimum well spacing for a specific reservoir can be determined.

The effect of well scheduling on the production performance is also examined. In multiple-well systems, starting all production wells at the same time provides faster hydrate dissociation. However, based on this study, starting production wells at different times yields more produced gas (about 10 percent by volume) even though less gas-hydrate dissociates. Therefore, starting production wells in the multiple-well system at different times could help in improving the gas production efficiency.

TABLE OF CONTENTS

LIST OF FIGURES

LIST OF TABLES

NOMENCLATURE

a	=	shape parameter
A	=	hydrate decomposition and formation rate constant
A_{dec}	=	specific surface area per unit bulk volume
A_{HS}	=	specific area of hydrate particles
b	=	hydrate cap temperature/shape parameter
B	=	hydrate decomposition and formation rate constant
B_g	=	formation volume factor of free-gas phase
B_w	=	formation volume factor of aqueous phase
B_x	=	incomplete beta function
c_H	=	concentration of hydrate
C_{ij}	=	Langmuir constant of hydrate former i in cavity type j
CMB	=	cumulative material balance
c_p	=	average hydrate cap heat capacity including rock, hydrate, water, and gas
c_{pg}	=	heat capacity of gas
c_{pi}	=	heat capacity of phase i at standard pressure
c_{pr}	=	heat capacity of rock
c_{pw}	=	heat capacity of water
D_γ^ζ	=	diffusion-dispersion tensor of component ζ in phase γ
E	=	activation energy
EB	=	energy balance

E_H = gas hydrate formation factor

f_e = fugacity of gas at T and P_e

f_i = gas phase fugacity of hydrate guest component i

f_g = fugacity of gas at T and P_g

$\overline{F}^i$ = mass flux of component i

$\overline{F}^E$ = heat flux

F_γ = advective mass flux vector in phase γ

g = gravitational acceleration

G_f = initial free gas-in-place

G_g = cumulative gas generation at standard condition

G_p = cumulative gas production at standard condition

H = hydrate zone thickness

h_g = gas enthalpy at pressure P_g

h_g^{ig} = gas enthalpy at standard pressure

h_l = molar enthalpy of phase l

H_l = enthalpy of phase l

H_m = Henry constant

IMB = incremental material balance

J_γ^ζ = diffusive mass flux vector of component ζ in phase γ

J_{gk} = productivity index of gas phase for well block layer k

J_{wk} = productivity index of aqueous phase for well block layer k

k = permeability at ϕ

K = three-phase (water-hydrate-vapor) equilibrium value

k_{cr} = thermal conductivity of cap and base rocks

k_d = decomposition rate constant

k_d^0 = intrinsic decomposition rate constant

K_h = heat conductivity of formation

k_{rg} = relative permeability to free-gas phase

k_{ra} = relative permeability to aqueous phase

k_0 = permeability at ϕ_0

$\bar{k}$ = average permeability

n_A, n_c, n_g = exponential parameters

N_m = number of methane molecule in methane hydrate

N_w = number of water molecule in methane hydrate

P_{ce0} = entry capillary pressure at the reference porosity, ϕ_0

P_e = dissociation pressure

p_e = gas entry pressure

P_g = gas phase pressure

p_i = initial reservoir pressure

P_w = water phase pressure

$P_{wf,\mathrm{k}}$ = sandface pressure of the well block layer k

$P_{wb,k}$ = well block pressure (layer k)

P^{υ} = water vapor pressure

$\bar{p}$ = average reservoir pressure

Q_{dis} = heat of hydrate dissociation

Q_E = external heat source

Q_{fus} = heat of fusion of ice

$\dot{Q}_H$ = heat of hydrate decomposition per unit volume

$\dot{Q}_{in}$ = direct heat input per unit volume

q_g^k = gas flow rate from layer *k*

$\dot{q}_{ml}$ = mass production rate of phase *l* per unit volume

q_w = water production rate

q_w^k = water flow rate from layer *k*

R = universal gas constant

R_H = hydrate recovery

r_w = wellbore radius

S = skin factor of a well

S_a = aqueous saturation

S_a^* = normalized aqueous saturation

S_g = gas saturation

S_{gr} = irreducible gas saturation

S_g^* = normalized free gas phase saturation

S_h = hydrate saturation

S_I = ice saturation

S_{irA} = irreducible aqueous saturation

S_s	=	solid (hydrate and/or ice) saturation
S_w	=	water saturation
S_{wirr}	=	irreducible water saturation
T	=	temperature
T_o	=	reference temperature (273.15 K)
T_{se}	=	hydrate cap temperature
u_γ	=	internal energy of phase γ
V_b	=	elementary volume
V_k^∞	=	volume of gas component *k* in water at infinite dilution
W_{ij}	=	cell potential for guest component *i* in cavity *j*
x_k	=	mole fraction of dissolved gas component *k* in water-rich phase
x_m	=	mole fractions of methane in aqueous phase
x_w	=	mole fraction of water in water rich phase
y_m	=	mole fractions of methane in free gas phase
Z	=	gas compressibility factor
z_i	=	compressibility pressure at initial pressure and temperature
β	=	hydrate equilibrium curve constant
μ_a	=	aqueous viscosity
μ_g	=	gas viscosity
μ_H	=	chemical potential of water in hydrate phase
μ_w	=	chemical potential of water in water rich (or ice) phase

Δc_{pw} = heat capacity difference between water (or ice) and empty-hydrate lattice

Δc_{pw}^{o} = reference heat capacity difference

Δh_{w} = enthalpy difference between water (or ice) and empty-hydrate lattice

Δh_{w}^{o} = reference enthalpy difference between water (or ice) and empty-hydrate lattice

ΔP_{ref} = pressure gradient of the referent layer

γ_{w} = activity coefficient of water rich phase

$\Delta \mu_{w}^{o}$ = chemical potential difference between the empty-hydrate lattice and water phase at the reference state (0 kPa, 273.15 K)

ρ_{l} = mass density of phase *l*

ρ_{r} = rock density

$\overline{\rho}_{g}$ = molar density of free gas phase

$\overline{\rho}_{a}$ = molar density of aqueous phase

ϕ = rock porosity

ϕ_{c} = critical permeability at which permeability is reduced to zero

θ_{dry} = dry thermal conductivity

ϕ^{e} = effective porosity

ϕ_{0} = rock porosity (ice- and hydrate-free porosity)/ reference porosity

θ_{I} = thermal conductivity of ice

θ_{wet} = wet thermal conductivity

v_l	=	velocity of phase *l*
ω	=	acentric factor
ω_γ^ζ	=	mass fraction of component ζ in phase γ
λ	=	effective thermal conductivity/ hydrate equilibrium curve constant
χ_γ^ζ	=	mole fraction of component ζ in phase γ

ACKNOWLEDGEMENTS

The author expresses his sincere appreciation and gratitude to his academic advisors, Dr. Turgay Ertekin and Dr. Luis Ayala, for their professional guidance. The author also would like to extend his gratitude to Dr. Derek Elsworth, Dr. Michael Adewumi, and Dr. Zuleima Karpyn for their interest in serving as committee members, and to Irene Gullapalli for her suggestion. Their suggestions, insights, and contribution to this work are greatly appreciated.

The author expresses his sincere appreciation to his fellow graduate students, friends and family especially his sister, Nuntawan Silpngarmlers, and his mother, Siriporn Chunsirikanjanawat, for their encouragement and support.

CHAPTER 1

INTRODUCTION

The demand of natural gas as a clean source of energy is rapidly increasing in the world. Natural gas hydrates are drawing attention worldwide as an unconventional source of energy because of the vast availability of this resource of energy and the foreseen increase in the demand of natural gas[1]. The estimates on the amount of natural gas being trapped within gas hydrate deposits vary within the limits of 10^{15} to 10^{19} standard m^3. It has been assessed that the current world energy consumption could be sustained for 180 years only by recovering one tenth of this class of trapped gas [1].

In order to produce gas from hydrate reservoir, it is necessary to destroy the crystalline water structure which traps the hydrocarbons. From a technical point of view, all potential schemes of gas production from hydrate reservoirs need to achieve at least the following three objectives:

- bring the pressure and temperature around hydrate particles outside the hydrate-stability zone
- sustain the energy required for endothermic dissociation reaction of hydrates
- provide the means to transfer of gas from the dissociation to production wells

According to these requirements, three possible basic gas recovery mechanisms have been suggested[2]: (1) depressurization, (2) thermal stimulation, and (3) inhibitor injection.

There are a number of challenges associated with producing gas from hydrate reservoirs. The gas hydrate phase is immobile and impairs flow conditions within the reservoir. This could slow down the depressurization rate within the reservoir and consequently reduce the rate of hydrate dissociation. Another issue is that the sensible energy within the reservoir may not be enough to provoke hydrate dissociation at an economical rate. The temperature drop due to dissociation process could slow down the dissociation rate. Additionally, after dissociation, released free water may freeze and end up as ice which obstructs the flow in porous media (even without freezing, the free water impairs gas production).

The complete numerical modeling of this type of reservoir is still at its developing stages. The reservoir modeling of this type of reservoir is still not clear because its dynamics and the role of parameters that control these dynamics have not been fully understood. Therefore, the need of the development as a tool that can further our understanding of the complication of this type of reservoirs and provide guidance for their exploitation is considered almost critical.

CHAPTER 2

LITERATURE REVIEW

2.1 A Historical Perspective

The history of natural gas hydrates has evolved over three major periods as described below[3]:

Period I: Hydrate as a Laboratory Curiosity

Natural gas hydrates were first discovered by Sir Humphrey Davy in the early 1800s. Throughout the remaining of the century, scientists attempted to identify all of the compounds which form hydrates as a first priority. They wished to quantitatively describe the compounds, their compositions, and physical properties. Since then, much work has been done for cataloging the various molecules that could co-exist as host (lattice-formers) and guests (hydrate-formers), and the various conditions at which each variety was stable. However, during this period, the subject of hydrates remained largely an academic curiosity because natural occurrences were not known.

Period II: Hydrate as a Problem to the Natural Gas Industry

In mid-1930's, Hammerschmidt determined that natural gas hydrates were responsible for blocking natural gas transmission lines, particularly at temperatures above freezing point of water. This discovery was crucial in bringing more attention to gas hydrates, and thereafter led to the regulation of the water content in natural gas

transmission lines. Many workers including Hammerschmidt (1939), Deaton and Frost (1946), Bond and Russell (1949), Kobayashi et al. (1951), and Woolfolk (1952) studied the effects of inhibitors, such as several chloride salts, on hydrate formation. In order to prevent and alleviate the hydrate appearance problem, methanol became one of the most popular inhibitors because it becomes concentrated in the free water phase after being vaporized into the gas at some upstream points.

Period III: Hydrate as a potential energy resource

In the late 1960s, the global view of clathrate science began to change dramatically when methane hydrate was observed as a naturally-occurring constituent of subsurface sediments in the giant gas fields of the Western Siberia basin. Thereafter, hydrate was also found in shallow, sub-permafrost sediments on the North Slope of Alaska. In 1972, hydrate cores and a full well log suite were retrieved at the Arco-Exxon NW Eileen well number 2 in West Prudhoe Bay, Alaska. A limited production test was also conducted, which recovered 92% methane at the surface from a hydrate bearing sandstone at an approximate depth of 2,200 feet. The estimated production rate (~4 mcf/d) was clearly not economical, and there were no further tests in the region.

By the mid-1970s, scientists began to consider that the low temperature/high pressure conditions necessary for hydrate formation should exist extensively around the globe, not only in permafrost regions, but also under deep oceans. In 1974, Soviet scientists recovered large hydrate nodules from the floor of the Black Sea. Then, in the early 1980s, the research vessel Glomar Challenger traveled the globe collecting cores of ocean bottom sediments as part of a renewed round of Deep Sea Drilling Project tests.

Many of the samples found chemical evidence for hydrate. However, one core taken off the coast of Guatemala included a one-meter long core composed almost entirely of methane hydrate.

2.2 Classification of Gas Hydrate Accumulations

In term of depositional characteristics, hydrate accumulations can be categorized into three classes as follows [4]:

Class 1 Accumulation: This class of accumulation comprises two layers: the hydrate interval (often exhibiting very low permeability due to the presence of large hydrate saturation in pore space), and an underlying two-phase fluid zone with free gas. In this class of accumulation, the bottom of hydrate stability zone (BHSZ) typically coincides with the bottom of hydrate interval because pressure increases with depth and temperature also increases with depth (under sea floor) due to geothermal energy. Thus, hydrate phase becomes unstable below a particular level (called the BHSZ) under sea floor as shown in Figure 2-1.

Class 2 Accumulation: This class of hydrate accumulation features two zones: a hydrate-bearing interval, and overlying a mobile water zone with no free gas (e.g., an aquifer). Figure 2-2 shows the conditions of class 2 hydrate accumulation.

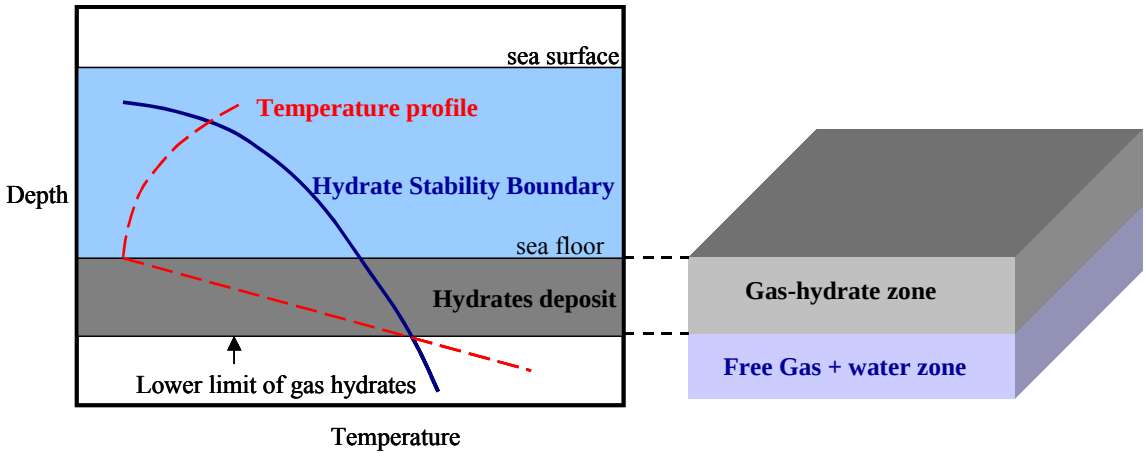

Figure 2-1: Class 1 hydrate accumulation

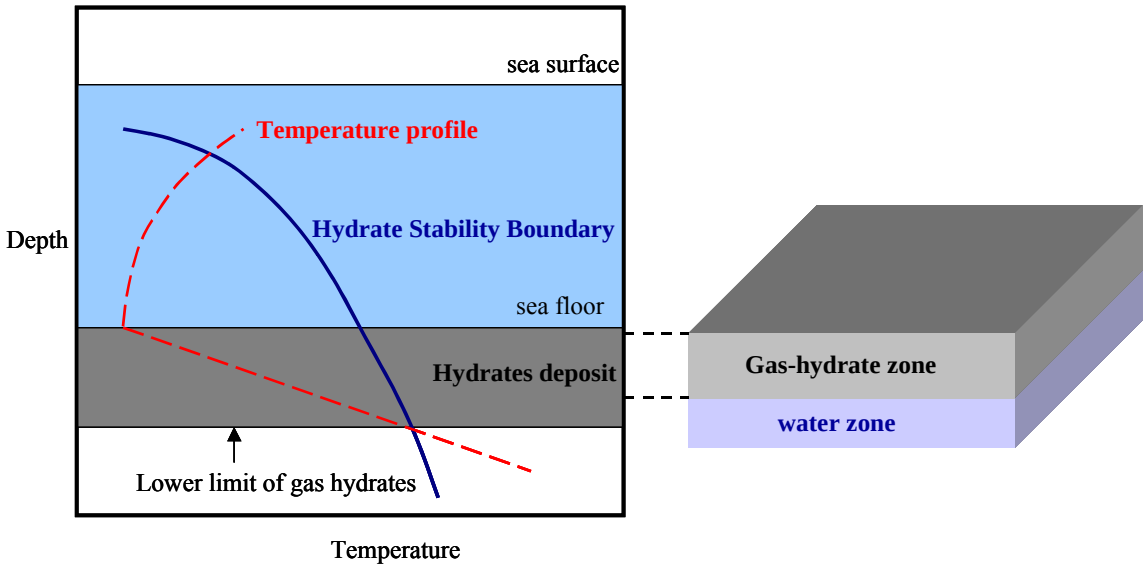

Figure 2-2: Class 2 hydrate accumulation

Class 3 Accumulation: This class of hydrate accumulation is composed of a single zone, the hydrate interval, and is characterized by the absence of an underlying zone of mobile fluids. The conditions for class 3 hydrate accumulation is shown in Figure 2-3.

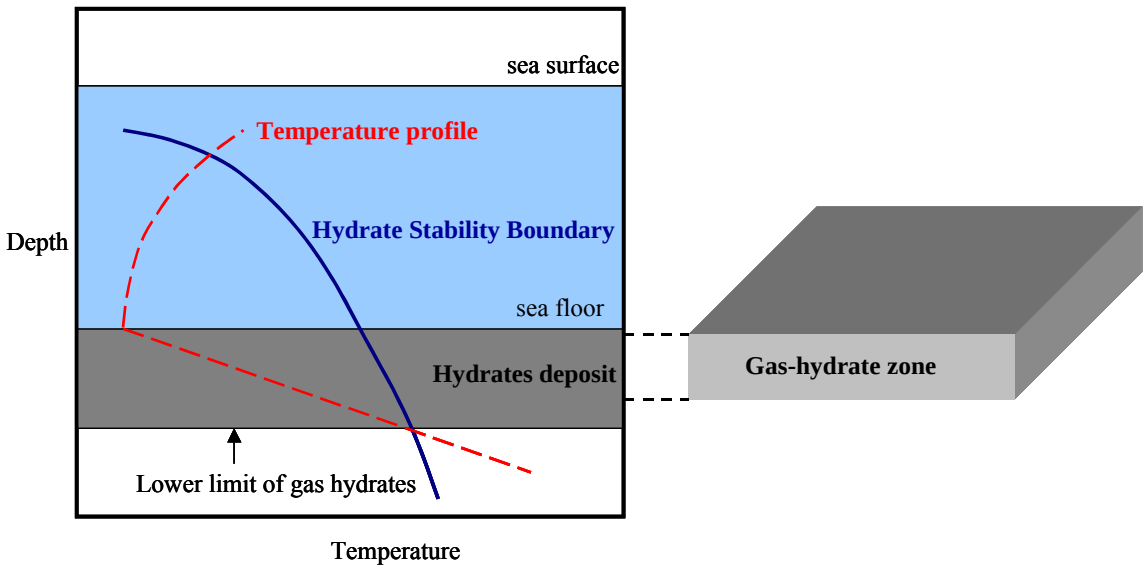

Figure 2-3: Class 3 hydrate accumulation

In classes 2 and 3 hydrate accumulations, the entire hydrate interval may be well within the hydrate stability zone. This means that the bottom of hydrate interval does not mark the bottom of hydrate stability zone (BHSZ).

The desirability of class 2 and class 3 hydrate accumulations as for gas production target is less well defined than for class 1 deposits[15]. This is because the bottom of hydrate stability zone (BHSZ) in class 1 deposits typically coincides with the bottom of hydrate interval. Therefore, it requires only small changes in pressure and temperature to induce dissociation process. Whereas the bottom of hydrate interval in class 2 and class 3 typically be within the hydrate stability zone. Consequently, it requires a larger pressure and temperate changes to induce the dissociation process.

2.3 Production Methods for Gas Hydrate Reservoirs

In order to produce gas from gas-hydrate reservoirs, it is necessary to destroy the crystalline water structure which traps hydrocarbon gas molecules inside the crystalline cavities. From a technical point of view, three potential gas production schemes for gas-hydrate reservoirs have been suggested[2] as discussed in the following sections.

2.3.1 Depressurization

In this method, the gas phase pressure around hydrate lattice is reduced across the hydrate stability zone. The depressurization can be achieved by removing gas and water from the reservoir through production wells. Gas-hydrates in the reservoir may not immediately start dissociating at the early stage of the production because reservoir pressure is still higher than the hydrate dissociation pressure at the reservoir temperature. Since hydrate dissociation is an endothermic reaction, a decrease in reservoir temperature is likely to be observed. So, the path of pressure and temperature changes for the depressurization process is actually the red line shown in Figure 2-4.

2.3.2 Thermal Stimulation

In thermal stimulation technique, a hot fluid such as hot water is injected into the reservoir in order to increase reservoir temperature. Hydrate phase becomes unstable when the reservoir conditions cross the stability boundary. Typically, average reservoir pressure decreases during the production. Thus, the change of reservoir conditions for

thermal stimulation is likely to follow the path shown in Figure 2-5. This production technique has a disadvantage as a significant portion of the energy introduced into the system is lost in the injection path and surroundings. Therefore, only a fraction of injected energy is utilized towards the dissociation of gas hydrates.

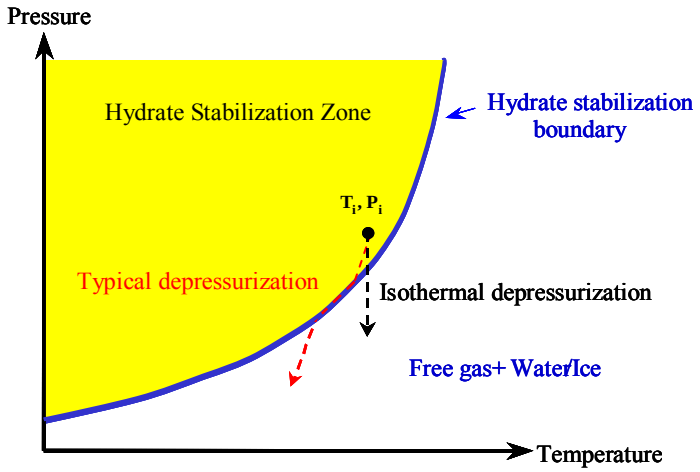

Figure 2-4: Depressurization path

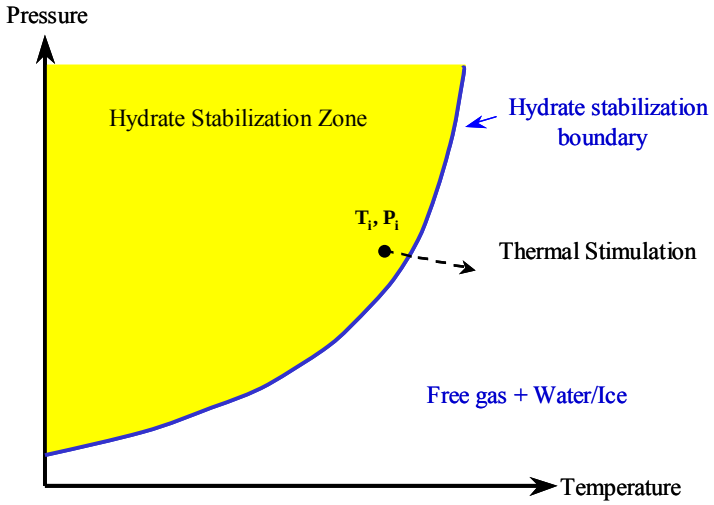

Figure 2-5: Thermal stimulation path

2.3.3 Inhibitor Injection

The objective of this technique is to move the stability boundary of the reservoir so that gas-hydrates in the reservoir become unstable at initial reservoir conditions. Consequently, gas-hydrates can start to dissociate. The change in hydrate stability boundary due to inhibitor injection is shown in Figure 2-6. However, this technique is considered as an uneconomic way of producing natural gas from gas-hydrate reservoirs due to the large amounts of inhibitor utilized. Moreover, penetration of inhibitors may become virtually impossible in tight hydrate formation.

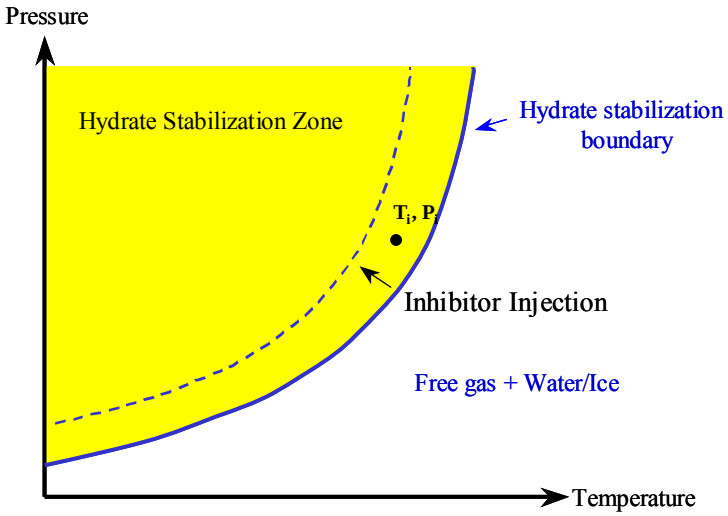

Figure 2-6: Change of stabilization boundary from inhibitor injection

2.4 Review of Hydrate Reservoir Simulation Models

During the past decades, gas-hydrates started to appear as a research topic within the agenda of researchers. Gas hydrate reservoirs are considered as the new potential energy sources for the next century as they represent a potentially enormous supply of natural gas. Since the production mechanisms from gas-hydrate reservoirs are not well understood, several researchers have developed gas-hydrate simulation models that explore the feasibility of various production schemes. In the next section, some of these models are discussed in a chronological order to provide some historical perspective.

2.4.1 Model 1, Holder, G. and Angert (1982) [5]

The goal of this study was to estimate the contribution of gas-hydrates to the total gas production of the reservoir. This study examines the dissociation of methane hydrates in a square reservoir of uniform thickness. The hydrate and gas zones were stratified (50 ft thick for each zone) but were included in the same media. The hydrate zone was assumed to be above the gas zone and the hydrate zone was impermeable (Figure 2-7).

The gas flow occurred only in the portion of reservoir containing gas. Additionally, the hydrate dissociation occurred only at the hydrate-gas interface which was at a uniform depth throughout the area extent of the reservoir. The model developed in this study was a single-phase (gas) flow simulator and water production from hydrate dissociation was not taken into account.

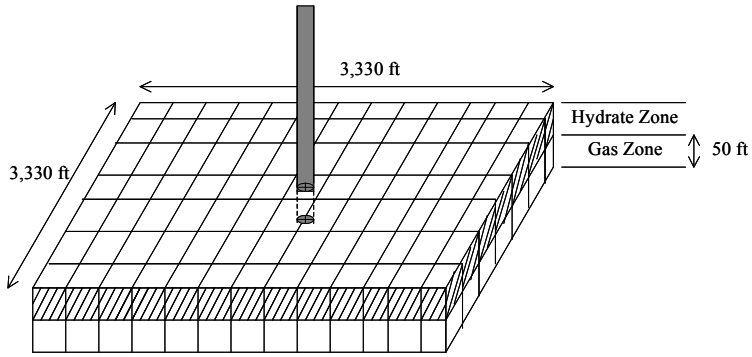

Figure 2-7: Reservoir structure in Holder et al.'s study

In this study, heat for hydrate dissociation was provided from the sensible heat of the hydrate reservoir. Furthermore, heat flow to hydrate-gas interface was allowed by conduction only.

During gas production, the hydrate-gas interface moved toward the surface due to hydrate dissociation. However, it was assumed that the interface still remained at a uniform although changing depth. The temperature at the interface was assumed to be the equilibrium hydrate dissociation temperature corresponding to the reservoir pressure at that point. The equations used in this model are listed in Table 2-1.

The amount of gas obtained from hydrates was compared to the total amount of gas production from this reservoir for a period of 1,000 days. The results showed that the percentage of produced gas coming from hydrate phase increased with time and it contributed about 20 to 30 percent of the total gas production. Moreover, the hydrate-gas interface became colder with time resulting in a greater heat flux to hydrate zone and hence in increased dissociation rate.

Table 2-1: Equations used in Holder et al.'s work

	Equations
Pressure distribution	$\nabla\left(\frac{K(\nabla P)}{\mu B}\right) + Q = \frac{d(\phi/B)}{dt}$
Temperature distribution	$\nabla^2 T = \frac{1}{\alpha}\frac{\partial T}{\partial t}$
Hydrates dissociation	$\frac{q}{2} = k\frac{\partial T}{\partial z} = \frac{\Delta H_D}{2} = \left(\frac{\dot{m}_H}{A}\right)$

2.4.2 Model 2, Burshears, O'Brien, and Malone (1986) [6]

The three-dimensional, two-phase (gas/water) reservoir simulation model of this study was developed to address fundamental questions regarding the feasibility of production schemes for gas reservoirs which were in contact with a gas-hydrate cap. The production of gas results in gas depressurization at the hydrate-gas interface. The primary objective of the model was to determine whether or not the depressurization was capable of initiating and sustaining hydrate dissociation at a practical rate. The second objective of the study was to determine the contribution of gas from dissociated hydrates to total gas production. The effect of water from hydrate dissociation on the production, such as the increase of water-gas ratio and the decrease of relative permeability to gas, was also investigated.

In this study, gas was produced from a single well located in the center of reservoir. The well was completed throughout the gas zone. The gas production rate was constant at a user-specified value. Besides, in free-gas zone, gas flow was radial toward the well. The temperature at any point on the hydrate-gas interface was assumed to be the equilibrium temperature for hydrate dissociation at a local pressure. Moreover, heat flow from the interior of hydrate cap and the gas reservoir to the hydrate-gas interface was possible by conduction only. In this model, the hydrate-gas interface moved upward toward the Earth's surface (due to hydrate dissociation) and the variation in interface depth was smoothened out and an average interface depth was used to determine the volume of the gas reservoir. The hydrate dissociation took place only at the hydrate-gas interface and the interior of hydrate zone was assumed to be impermeable. The equations used in this study are listed in Table 2-2.

For a wide range of realistic variation studies, the simulator indicated that hydrate can be dissociated without an external energy source, i.e., the sensible heat of the reservoir provided the necessary energy for hydrate dissociation. The water involved in hydrate dissociation did not result in an undesirable high producing water-gas ratio and did not impair gas flow to a notable degree. It was concluded that depressurization was a feasible method for dissociating gas-hydrates found at depth greater than 2,300 ft (701 m) in the Alaskan North Slope.

Table 2-2: Equations used in Burshears et al.'s work

	Equations
Pressure distribution	$\nabla\left(\frac{k\,k_{rw}}{\mu_w\,B_w}\left(\nabla P_w - \rho_w g z\right)\right) + Q_w = \frac{d(\phi S_w / B_w)}{dt}$ $\nabla\left(\frac{k\,k_{rg}}{\mu_g\,B_g}\left(\nabla P_g - \rho_g g z\right)\right) + Q_g = \frac{d(\phi S_g / B_g)}{dt}$
Saturation relationship	$S_w + S_g = 1$
Capillary Pressure relationships	$P_w + P_c = P_g$
Temperature Distribution	$\nabla^2 T = \frac{1}{\alpha}\frac{\partial T}{\partial t}$
Dissociation pressure	$P_e = \exp\left[a + \frac{b}{T}\right]$ (*pure gas*) $\ln\left(\frac{P_e}{P_o}\right) = \sum\left(A_i\,x_i + B_i\,x_i^2\right)$ (*mixed gas*)
Dissociation enthalpy	$H_D = c + d\,T$ (*pure gas*) $\ln\left(\frac{H_D}{H_{DO}}\right) = \sum\left(A_i\,x_i + B_i\,x_i^2\right)$ (*mixed gas*)

2.4.3 Model 3, Yousif, Abass, and Selim (1991) [7]

A one-dimensional, three-phase flow model was developed in this study to simulate the process of gas production from Berea sandstone samples containing methane hydrate by means of a depressurization mechanism.

In all models previously proposed, flow equations in a hydrate zone were not considered as a complement to the equation of mass and energy. One purpose of this study was to model the hydrate-depressurization process considering equations of change for both mass and momentum for each phase (gas, water, and hydrate) in the porous medium. The equations used in the model are listed in Table 2-3.

The model was validated using the data collected in laboratory experiments. It was found that the absolute permeability, relative permeability, and reaction rate constant must be varied in order to obtain a satisfactory match of the model to the available experimental data. For example, the relative permeability curve for water was shifted upward about 20% to make the system more permeable to water. The relative permeability curve for gas was shifted upward 3% to make the system slightly more permeable to gas. Furthermore, the dissociation reaction rate constant (k_d) was decreased from 10^{-11} to 10^{-16} kmol/(m^2-Pa-sec) for pure hydrate dissociation.

Table 2-3: Equations used in Yousif et al.'s work

	Equations
Flow equations	$\frac{\partial}{\partial x}\left(\frac{\rho_w k k_{rw}}{\mu_w}\frac{\partial P_w}{\partial x}\right) + \dot{m}_w = \frac{\partial}{\partial t}(\phi \rho_w S_w)$ (*water*) $\frac{\partial}{\partial x}\left(\frac{\rho_g k k_{rg}}{\mu_g}\frac{\partial P_g}{\partial x}\right) + \dot{m}_g = \frac{\partial}{\partial t}(\phi \rho_g S_g)$ (*gas*) $-\dot{m}_H = \frac{\partial}{\partial t}(\phi \rho_H S_H)$ (*hydrate*)
Saturation relationship	$S_w + S_g + S_H = 1$
Capillary pressure relationships	$P_c(S_w) = P_g - P_w$
Hydrate dissociation	$\dot{m}_g = k_d A_s (P_e - P)$ $A_s = (\phi_{wg}^3 / 2k)^{1/2}$ $\dot{m}_g = \dot{m}_H \frac{M_g}{N_H M_w + M_g}$

2.4.4 Model 4, Chuang, Goodarz, and Duane (2001) [8]

A one-dimensional linearized model suggested by Makogon[7] was used in the analysis. The temperature and pressure distributions in porous layer of methane hydrate and in the gas region were evaluated for different well pressures and reservoir temperatures. In this study, it was assumed that the hydrate decomposition in a porous medium does not occur in the entire volume, but takes place in a narrow region that can be treated as a surface, the so-called decomposition front. This moving front separates the volume of the reservoir into two zones with different phases. In the near-well zone, only natural gas and water exist, whereas only the solid hydrate and natural gas exist in the zone further away from the well (Figure 2-8). For a one-dimensional model, the distribution of pressure in the layer was described using an analog of the classical Stefan problem for melting. There were several important assumptions involved in this study. One was that the pressure and temperature at any point on the decomposition front were the equilibrium pressure and temperature for dissociation of methane hydrate. The hydrate reservoir was also assumed to be porous and contain free natural gas. As the dissociation front moves outward, heat must be supplied to the front because of the endothermic nature of the hydrate dissociation process. Furthermore, during hydrate dissociation, the movement of released water in the porous medium was assumed to be negligible. The governing equations used in the model are listed in Table 2-4. The production rate equation listed in the table was developed from the first three equations using linearization technique. It should be noted here that the model used in this study

neglects the heat conduction in the entire reservoir. Thus, the energy balance at the decomposition front cannot be enforced.

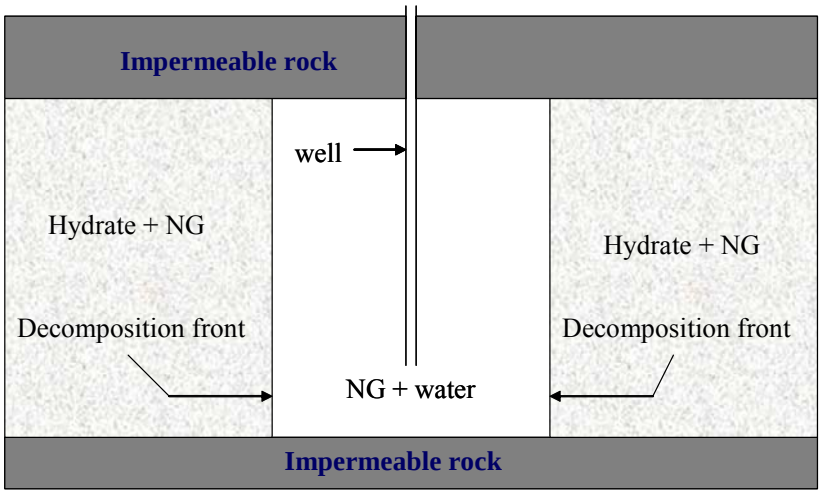

Figure 2-8: Gas hydrate reservoir in Chuang et al.'s study

Table 2-4: Governing equations used in Chuang et al.'s work

	Equations
Pressure distribution	$\frac{2\Phi_n \mu}{k_n}\frac{\partial P_n}{\partial t} = \frac{\partial^2 P_n^2}{\partial x^2}$
Hydrate phase equilibrium	$\log_{10} P_D = a(T_D - T_0) + a(T_D - T_0)^2 + c$
Conductive-convective heat transfer	$a_n \frac{\partial^2 T_n}{\partial x^2} = \frac{\partial T_n}{\partial t} - \frac{c_v k_n}{c_n \mu}\frac{\partial P_n}{\partial x}\left(\frac{\partial T_n}{\partial x} - \delta\frac{\partial P_n}{\partial x}\right) - \eta\frac{\Phi_n c_v}{c_n}\frac{\partial P_n}{\partial t}$
Production rate equation	$Q = \frac{k_1}{\mu}\frac{\partial P_1(0,t)}{\partial x} = \frac{k_1}{\mu}\frac{P_D^2 - P_G^2}{P_G}\frac{1}{erf(\alpha_1)}\frac{1}{2\sqrt{\pi\chi_1 t}}$

In this work, authors were trying to find answers to two questions: (1) Can natural gas be produced by depressurization through drilling a well into a hydrate reservoir? (2) What are the parameters that control the natural gas production rate? In particular, is the gas production thermally controlled?

The results presented in this study guided the authors towards the following conclusions:

- Under favorable conditions, natural gas can be produced from hydrate reservoirs placing a depressurization well.
- The natural gas production rate was controlled by the physical and thermal conditions of the reservoir and the well pressure.
- The required heat for hydrate dissociation could be supplied by the natural gas convection from the exterior (hydrate and natural gas) portions of the field.
- For an infinitely homogenous hydrate reservoir containing natural gas, the dissociation pressure and temperature were fixed (within the bounds of a linearized model), and they depend only on the reservoir conditions and the well pressure.
- For a fixed reservoir pressure and temperature, the well output decreases and the motion of the decomposition front slows as the well pressure increases.
- For fixed reservoir and well pressures, the gas production rate decreases significantly as the reservoir temperature decreases.

- For homogenous hydrate reservoir, the reservoir permeability significantly affects the rate of convective heat transfer and consequently the rate of natural gas production.
- For a fixed porosity, the reservoir with higher permeability has higher production rate and the decomposition front penetrates faster into the reservoir. However, the variation of permeability has a slight effect on the dissociation temperature and pressure at the front.

2.4.5 Model 5, Moridis (2002) [2]

In this work, authors used EOSHYDR2 to explore different mechanisms and strategies for production from typical CH_4-hydrate accumulations. EOSHYDR2 was presented as a new module for the TOUGH2 general-purpose simulator for multi-component, multiphase fluid and heat flow in the subsurface. EOSHYDR2 can model the non-isothermal gas release, phase behavior and flow of fluids and heat under typical conditions of common natural gas hydrate deposits (i.e., in the permafrost and in deep ocean sediments).

EOSHYDR2 includes both equilibrium and kinetic models of hydrate formation and dissociation. This model accounts for up to four phases (gas phase, liquid phase, ice phase, and hydrate phase) and up to nine components. The mass and energy balance equations and all correlations used in this work are listed in Table 2-5.

Table 2-5: Equations used in Moridis' work

	Equations
Flow Equations	$\frac{d}{dt}\int_{V_n} M^k dV = \int_{\Gamma_n} F^k \cdot n\, d\Gamma + \int_{V_n} q^k dV$ $M^w = \sum_{\beta \equiv A,G,I} (\phi \rho_\beta S_\beta X_\beta^w) + M_H^w$ $M^{m,v} = \sum_{\beta \equiv A,G,I} (\phi \rho_\beta S_\beta X_\beta^{w,v}) + M_H^{w,v}$
Hydrate Dissociation	$q^k = \chi_k W_k A_k k_k \exp(\frac{\Delta E^k}{RT})(f_{ek}(T) - f_k), \quad k \equiv m,v$ $q^w = \sum_{k \equiv m,v} \chi_k N_k W_k A_k k_k \exp(\frac{\Delta E^k}{RT})(f_{ek}(T) - f_k)$
Dissociation Pressure	$P_e(kPa) = \exp\left(e_1 - \frac{e_2}{T(K)}\right)$
Dissociation Rate (Optional)	$\dot{m}_g = k_d A_s (P_e - P)$
Heat of Dissociation	$\Delta H^0 = zRT^2 \frac{d(\ln P)}{dT}$
Heat flux	$F^\theta = -\{(1-\phi)K_R + \phi[S_H K_H + S_A K_A + S_G K_G + S_I K_I]\}\nabla T + \sum_{\beta \equiv A,G} h_\beta F_\beta$

In this study, results from four test problems that explore different mechanisms and strategies for production from methane hydrate accumulations were presented. The results indicate that methane production from reservoirs containing methane hydrates can be technically feasible and had significant potential. In particular, thermal stimulation is capable of producing substantial amounts of hydrocarbons, and its effectiveness could be improved when coupled with depressurization and the use of hydrate inhibitors.

2.4.6 Model 6, Sun, Nanchary, and Mohanty (2004) [9]

In this work, a thermal, three-phase, one-dimensional numerical model was developed to simulate two regimes of gas production from sediments containing methane hydrates by depressurization. Authors defined and employed a parameter named dissociation-flow time-scale ratio, R_τ, to identify two regimes, the dissociation-controlled and the flow controlled regimes. In their work, authors implemented the finite difference scheme and equations; they were implicit in water and gas saturation, pressure, and temperature, and explicit in hydrate saturation. The equations used in this work are listed in Table 2-6. The model could be used to fit laboratory-scale experimental data, but the dissociation rate constant, the multiphase flow parameters and the heat transfer parameters must be adjusted.

The salient conclusions of this study were:

- The parameter, R_τ, proposed in this work determines whether the process is dissociation-controlled or flow-controlled. The field scale processes were often flow-controlled, whereas the laboratory scale process could be dissociation

controlled if the permeability is high enough. The production rate does not change much with the kinetic rate if the process is flow controlled.

- Different temperature boundary conditions at the production well do not make a significant difference to the gas production rate at the field scale.
- Gas production rate from a linear reservoir is more sensitive to the heat transfer coefficient with the surrounding than the longitudinal heat conduction coefficient, in 1-D simulations.

Table 2-6: Governing equations used in Sun et al.'s work

	Equations
Flow Equations	$\frac{\partial}{\partial t}(\phi \rho_g S_g) + \frac{\partial}{\partial x}(\rho_g v_g) = \dot{m}_g$
	$\frac{\partial}{\partial t}(\phi \rho_w S_w) + \frac{\partial}{\partial x}(\rho_w v_w) = \dot{m}_w$
	$\frac{d}{dt}(\phi \rho_h S_h) = -\dot{m}_h$
Dissociation Rate	$\dot{m}_g = k_d A_s (P_e - P)$
Dissociation Pressure	$P_e = 1.15 \exp\left(49.3185 - \frac{9459}{T}\right)$
Relative Permeability	$k_{rw} = \left(\frac{s_w/(s_w + s_g) - S_{wirr}}{1 - S_{wirr} - S_{gr}}\right)^{n_w}$
	$k_{rg} = \left(\frac{s_g/(s_w + s_g) - S_{wirr}}{1 - S_{wirr} - S_{gr}}\right)^{n_g}$
Capillary Pressure	$\frac{P_c}{P_c^e} = h_c(s_w) = \left(\frac{s_w/(s_w + s_g) - S_{wirr}}{1 - S_{swirr}}\right)^{-n_c}$
Gas viscosity	$\mu_g = 2.4504x10^{-3} + 2.8764x10^{-5}T + 3.279x10^{-9}T^2 - 3.7838x10^{-12}T^3 + 2.0891x10^{-5}\rho_g + 2.5127x10^{-7}\rho_g{}^2 - 5.822x10^{-10}\rho_g{}^3 + 1.8378x10^{-13}\rho_g{}^4$
Energy Balance	$\frac{\partial}{\partial t}\left[\phi(\rho_g S_g H_g + \rho_w S_w H_w + \rho_h S_h H_h) + (1-\phi)\rho_S H_S\right] + \frac{\partial}{\partial x}(\rho_g v_g H_g + \rho_w v_w H_w) = \frac{\partial}{\partial x}\left(\lambda \frac{\partial T}{\partial x}\right) + q$

2.4.7 Model 7, Sun and Mohanty (2005) [10]

In this work, a methane hydrate reservoir simulator was developed based on the assumption of equilibrium phase transition. Two components (methane and water) and four phases (hydrate, gas, aqueous, and ice) are considered in the proposed model. Mass transport including two-phase flow and the molecular diffusions, and heat transfer through convection and conduction are included in the mathematical model. The governing equations are discretized using finite difference method and are solved with the Newton-Raphson method in a fully implicit manner. The equations used in this work are listed in Table 2-7.

In this work, three examples were presented about the hydrate accumulation in offshore sediments and gas production from hydrate reservoir using depressurization and thermal stimulation. The simulation results of hydrate accumulation in offshore sediments are consistent with the predictions by previous researchers, and the results of gas production simulation can be readily used in future economical feasibility analysis of hydrate reservoirs as a potential energy resource.

Table 2-7: Equations used in Sun and Mohanty's work

	Equations
Mass Transfer Flux	$\overline{F}^{i} = \rho_G \overline{v}_G w_G^i + \rho_A \overline{v}_A w_A^i + \overline{J}_G^i + \overline{J}_A^i$
Heat Flux	$\overline{F}^{E} = \rho_G \overline{v}_G H_G + \rho_A \overline{v}_A H_A - \lambda \nabla T$
Mass Balance	$\frac{\partial}{\partial t}\left[\phi \sum_{j=H,G,A,I} \rho_j S_j w_j^m\right] + \nabla \cdot \overline{F}^{m} = q^m \quad (methane)$ $\frac{\partial}{\partial t}\left[\phi \sum_{j=H,G,A,I} \rho_j S_j w_j^w\right] + \nabla \cdot \overline{F}^{w} = q^w \quad (water)$
Energy Balance	$\frac{\partial}{\partial t}\left[\phi \sum_{j=H,G,A,I} \rho_j S_j U_j + (1-\phi)\rho_R U_R\right] + \nabla \cdot \overline{F}^{E} = q^E$
Capillary Pressure	$P_c = P_{ce}\left(S_A^{e*}\right)^{-n_c} \quad where \; P_{ce} = P_{ce0}\sqrt{\frac{\phi^e k_0}{\phi_0 k}}$
Local Absolute Permeability	$\frac{k}{k_0} = \frac{\phi^e}{\phi_0}\left(\frac{\phi^e(1-\phi_0)}{\phi_0(1-\phi^e)}\right)^{2\beta} \quad where \; \phi^e = \phi\,(S_g + S_a)$
Relative Permeability	$k_{rG} = k_{rG}^0 (S_G^{e*})^{n_G}$ $k_{rA} = k_{rA}^0 (S_A^{e*})^{n_A}$

2.4.8 Model 8, Moridis (2005) [11]

In this work, the developed simulator TOUGH-FX was used. The simulator includes both an equilibrium and kinetic model of hydrate formation and dissociation. The main mathematical equations shown in Table 2-5 (see section 2.4.5) are still used in this model. Unlike the previous developed model, the effect of hydrate saturation on capillary pressure between free gas and aqueous phases is also taken into account in this simulator. The additional equations used in this model are listed in Table 2-8.

The main objectives of this study were to evaluate the production potential of class 1 hydrate accumulations implementing depressurization technique and to determine the factors and conditions affecting it. Two different systems were studied. The first system has hydrate and water in the upper hydrate zone and is hence referred to as a Class 1W deposit. The second system has hydrate and free gas in the upper hydrate zone which is referred to as a Class 1G deposit. The following conclusions could be drawn from this study:

- Large volume of gas is readily produced at high production rate from class 1 hydrate deposits by means of depressurization using conventional technology.
- Wellbore heating of the entire production interval and substantial part of the hydrate interval is a necessity in production in order to avoid blockage caused by hydrate formation around the well.
- In class 1 deposits, up to 65% of the production rate and 45% of the cumulative production are replenished with gas released from hydrate dissociation.

Table 2-8: Additional equations in the modified Moridis' model (2005)

	Equations
Thermal conductivity	$\theta_c = \theta_{dry} + (S_a^{1/2} + S_H^{1/2})(\theta_{wet} - \theta_{dry}) + \phi S_I \theta_I$
Intrinsic permeability	$\frac{k}{k_0} = \frac{1}{2}\left[k_{ra}(S_a = 1 - S_s) + k_{rg}(S_g = 1 - S_s)\right]$ *or* $\frac{k}{k_0} = \left(\frac{\phi - \phi_c}{\phi_0 - \phi_c}\right)^n$
Capillary pressure	$P_{cap}(S_a) = P_{cap,0}\sqrt{\frac{k_0}{k} \cdot \frac{\phi}{\phi_o}}$ *or* $P_{cap}(S_{aA}, S_H) = H(S_H) \cdot F \cdot P_e \cdot (S_{aA})^c$ $S_{aA} = (S_a - S_{ira})/(1 - S_{ira})$

- A unique and universal characteristic of gas production from class 1 hydrate deposits by depressurization is the evolution of a second horizontal hydrate interface that first appears at the top of the hydrate interval and advances downward.
- In Class 1G accumulations, the hydrate contribution to gas production monotonically increases with time. Up to 75% of the rate of gas production and 54% of the cumulative gas production are replenished by gas released from

hydrate dissociation. Class 1G deposits are slower to respond than Class 1W deposits, but their efficiency increases with time.

- Long-term production from class 1 hydrate accumulations causes the temperature to decrease in the reservoir resulting from endothermic hydrate dissociation reaction. However, the temperature drops are mild indicating that th risk of evolution of ice is minimal.
- Water production remains very low during the long-term gas production from class 1 hydrate accumulations.
- Relative permeability and capillary pressures in hydrate-bearing media are complex processes that play a critical role in production from gas hydrate systems. The new models to describe the effect of the presence of hydrates on the wettability properties of porous media were introduced in this study.
- Capillary plays a critical role in gas production. It is responsible for hydrate lensing which is analogous to the process called frost heave. A stronger capillary suction in the regions with larger hydrate content, due to smaller effective pore sizes, causes water to be drawn toward regions with larger hydrate saturation causing additional hydrate formation there at the expense of neighboring regions. This results in the development of banded patterns with alternating layers of large and small hydrate saturation.
- Because of limitations in the ability to describe hydrate dissociation at very high saturations under conditions impermeable to fluids, the predictions should be viewed as the lower limit of the possible solutions.

2.4.9 Model 9, Hong and Pooladi-Darvish's (2005) [12]

In this work, a 2D cylindrical simulator for gas hydrate reservoirs was developed. The model includes the equations for two phase (gas-water) flow, conductive and convective heat transfer, and intrinsic kinetics of hydrate decomposition. The developed simulator was used to study a hydrate reservoir where the hydrate-bearing layer overlies a free-gas zone (class 1 hydrate accumulation). A production well was drilled and completed in the middle of free-gas zone. In this study, the impact of the overlying hydrate in improving production performance of the underlying gas reservoir and the effect of various parameters on gas production behavior were examined. The equations used in this model are listed in Table 2-9. The conclusions from this examination are summarized below:

- The presence of gas hydrate on top of a free gas reservoir provides a significant improvement of the productivity of the underlying gas reservoir.
- A larger thermal conductivity yields more heat transfer from the cap- and base-rock and results in more hydrate decomposition.
- Heat conduction and sensible heat of hydrate zone plays dominant role in gas generation by depressurization.
- Rock permeability is an important factor in the gas production. However, the long-term production of gas depends on continued decomposition of gas hydrates which is predominantly limited by availability of heat.

Table 2-9: Equations used in Hong and Pooladi-Darvish's work

	Equations
Flow Equation	$-\nabla\cdot(\rho_l\vec{u}_{lD}) + \dot{q}_{ml} + \dot{g}_l = \frac{\partial}{\partial t}(\phi\rho_l S_l)$ *where* $\vec{u}_{lD} = -\frac{kk_{rl}}{\mu_l}\frac{\partial\Phi_l}{\partial D}\ (l=g,w\ ;\ D=r,z)$
Energy balance	$\nabla\cdot(k_c\nabla T)-\nabla\cdot(\rho_g\vec{u}_{gD}h_g+\rho_w\vec{u}_{wD}h_w)+\dot{q}_{mw}h_w+\dot{q}_{mg}h_g+\dot{Q}_H$ $+\dot{Q}_{in} = \frac{\partial}{\partial t}\left[(1-\phi)\rho_R U_R+\phi(S_H\rho_H U_H+S_w\rho_w U_w+S_g\rho_g U_g)\right]$ *where subscript* $D=r,z$
Thermal conductivity	$k_c = k_{c,rock}(1-\phi)+\phi(k_{c,H}S_H+k_{c,w}S_w+k_{c,g}S_g)$
Kinetics Equations	$\dot{g}_g = k_d M_g A_{dec}(f_e - f_g)$ $\dot{g}_w = \dot{g}_g N_H \frac{M_w}{M_g}$ $\dot{g}_H = -\dot{g}_g \frac{M_H}{M_g}$ *where*: $k_d = k_d^0 \exp\left(\frac{-E}{RT}\right)$ $A_{dec} = \phi S_H A_{HS}$

- The dissociation front remains at equilibrium through out the simulation which implies that the equation of intrinsic rate of decomposition is not needed. However, when the decomposition rate constant was lowered by orders of magnitude, non-equilibrium effects played some roles.
- Lower wellbore pressure can increase hydrate dissociation and gas production rates. However, reducing too much bottom-hole pressure may cause the reservoir

temperature to fall below the freezing point leading to the formation of ice which block pathway for fluid flows toward a production well.

2.4.10 Model 10, Gerami and Pooladi-Darvish's (2006) [13]

In this work, the first tank-type material balance model for a hydrate-capped gas reservoir, Class 1 hydrate accumulations, has been developed. The material balance equation is developed by analytically and simultaneously solving the mass and energy balance equations. The solutions of the equations provided the average reservoir pressure and the released gas from hydrate dissociation as a function of cumulative produced gas, for a reservoir that is produced at a constant rate.

The developed material balance model is developed based on the following assumptions:

- The reservoir is consisted of, at most, three components including hydrate, water, and methane gas.
- One mole of hydrate decomposes to one mole of methane gas and N_H moles of water, where N_H is hydration number.
- The expansions of water and rock are modeled using average compressibility of water and rock, respectively.
- Water influx may occur.
- The porosity and initial saturations are uniform throughout the reservoir.

Gas production from hydrate reservoirs involves a combination of different mechanisms of fluid flow, heat transfer, and thermodynamics of hydrate dissociation.

These equations are nonlinear and require numerical technique to obtain solutions. Therefore, to obtain a model using analytical techniques, the following assumptions are made:

- A tank type model is used to predict average reservoir pressure. It implies that the pressure and temperature in the system are instantaneously uniform.
- Geothermal gradient and the hydrostatic pressure can be ignored.
- Convective heat transfer is ignored.
- Hydrate dissociation follows the three-phase hydrate equilibrium relation.
- The temperature of free-gas zone remains at the initial reservoir temperature.
- No water influx and the change in formation fluid-filled pore volume is negligible.
- The thermo-physical properties of hydrate, reservoir, and surrounding formations (cap and base rocks) remain constant during the production period.

For energy balance calculation, the sensible heat of rocks and fluids surrounding hydrate in porous media and heat conducted from the cap and base rocks are the two sources of heat available for hydrate dissociation. The governing equation for heat transfer from the cap rock is determined by conservation of energy using Fourier's law of heat conduction[14]. The equations used in this model are listed in Table 2-10.

Table 2-10: Equations used in Gerami and Pooladi-Darvish's work

	Equations
Material balance (Simplified)	$\frac{\bar{P}(t)}{Z(t)} = \frac{p_i}{z_i}\left(1-\frac{G_p(t)-G_g(t)}{G_f}\right)$
Energy balance	$\left.\frac{dT}{dz}\right\|_{z=0} = \left(\frac{\Delta H \cdot \rho_H}{k_{cr} \cdot A \cdot E_H}\right)\frac{dG_g}{dt} + \left(\frac{\rho \cdot c_p \cdot V_b}{k_{cr} \cdot A}\right)\frac{dT_{se}}{dt}$
Dissociation Pressure	$P_e = \exp\left(\lambda - \frac{\beta}{T_{se}}\right)$
Temperature gradient at hydrate interface	$\left.\frac{\partial T}{\partial z}\right\|_{z=0} = 2 \cdot b(t)\sqrt{\frac{t}{\pi \alpha_r}}$
Gas dissociation rate	$q_g(t) = \frac{E_H A H \rho c_p}{\rho_H \Delta H} b(t)\left(\frac{4\rho_r c_{pr}\sqrt{\alpha_r}}{\rho c_p H\sqrt{\pi}}\sqrt{t}+1\right)$
Hydrate recovery	$R_h(t) = \frac{\rho c_p}{\phi S_H \rho_H \Delta H} b(t)\left(\frac{8\rho_r c_{pr}\sqrt{\alpha_r}}{3\rho c_p H\sqrt{\pi}}\sqrt{t}+1\right)\cdot t$
Temperature parameter	$b(t) = q_w\left(\begin{array}{l}\frac{1-(p_{oe}Z_i)/(p_i Z_{oe})}{T_i - T_{oe}} G_f \\ + \frac{E_H A H \rho c_p}{\rho_H \Delta H}\left(\frac{8}{3\rho c_p H\sqrt{\pi}}\sqrt{k_{cr}c_{pr}\rho_r t}+1\right)\end{array}\right)^{-1}$
Initial free gas-in-place	$G_f = \frac{(T_i - T_{oe})\left[\frac{q_w}{b_{match}} - \frac{E_H A}{\rho_H \Delta H}\left(\frac{8\sqrt{t_{avg}}}{3\sqrt{\pi}}\sqrt{k_{cr}\rho_r c_{pr}} + H\rho c_p\right)\right]}{1-(p_{oe}Z_i)/(p_i Z_{oe})}$
Hydrate cap thickness	$H = \frac{1}{\rho c_p}\left[\left(\frac{q_w}{b_{match}} - \frac{1-(p_{oei}Z_i)/(p_i Z_{oe})}{T_i - T_{oe}} G_f\right)\frac{\rho_H \Delta H}{E_H A} - \frac{8\sqrt{t_{avg}}}{3\sqrt{\pi}}\sqrt{k_{cr}\rho_r c_{pr}}\right]$

In this study, the developed model was used to study (using its forward solution mode) the effects of important parameters (including reservoir porosity, rock thermal conductivity, production rate, hydrate zone thickness, free-gas zone thickness, reservoir radius, reservoir permeability, and initial reservoir temperature) on production characteristics of hydrate reservoirs. The initial free gas-in-place, G_f, and the initial thickness of the hydrate cap, H, can be determined using the inverse solution mode of the model.

The following conclusions could be drawn from this study:

- The temperature in hydrate zone drops in a close-to-linear manner and the rate of temperature decline is a function of production rate, reservoir volume, thermo-physical properties of hydrate cap, and a weak function of production time.
- For the depressurization technique, the dissociation of hydrates can contribute significantly to the total production of a gas reservoir.
- The dissociation rate of hydrate phase in the reservoir strongly depends on the degree of pressure reduction.
- The deliverability equation developed for conventional gas reservoirs may be used for hydrate-capped gas reservoirs if it is modified for the average reservoir pressure and partial penetration skin.

2.4.11 Model 11, Phale and Zhu's (2006) [15]

Depressurization, thermal stimulation, and inhibitor injection are the methods being examined for commercial gas production from gas hydrate reservoirs. In this study,

an alternative of gas production from gas hydrate reservoirs using CO_2 injection is investigated. This method has several attractive features: 1) CO_2 is thermodynamically favored over CH_4 in hydrate, 2) the heat released by formation of CO_2-hydrate is 20% greater than the hat needed for dissociating CH_4-hydrate, 3) refilling pore space with CO2-hydrate is expected to maintain mechanical stability of the hydrate-bearing formations during production, and 4) the process is environmental friendly, removing CO_2 from atmosphere while simultaneously producing clean-burning natural gas. This study focused on the evaluation of a set of optimum parameters for methane recovery with simultaneous CO_2 sequestration using the STOMP-HYD simulator which is developed by the Pacific Northwest National Laboratory.

Four mass conservation equations and one energy conservation equation are used in STOMP simulator to describe the subsurface hydrate system where the conserved mass components are water, CH_4, CO_2, and salt (NaCl). Aqueous, liquid CO_2, and free gas are assumed to be mobile phases whereas hydrate, ice, precipitated salt, and host porous media are assumed to be immobile phases in the model. The equations used in this model are shown in Table 2-11.

Table 2-11: Equations used in STOMP-HYD simulator

	Equations
Energy conservation	$\frac{\partial}{\partial t}\left(\sum_{\gamma=l,g,n,h,i,p}(\phi\rho_\gamma s_\gamma u_\gamma)+(1-\phi)\rho_s u_s\right)=-\sum_{\gamma=l,g,n}\left(\nabla(h_\gamma F_\gamma)\right)$ $-\sum_{\zeta=w,a,o}\left(\nabla(h_g^\zeta J_g^\zeta)-\nabla(k_e\nabla T)\right)+\sum_{\gamma=l,g,n}\left(h_\gamma \dot{m}_\gamma\right)+\dot{q}$
Mass conservation	$\frac{\partial}{\partial t}\left(\sum_{\gamma=l,g,n,h,i,p}(\phi\rho_\gamma s_\gamma \omega_\gamma^\zeta)\right)=-\sum_{\gamma=l,g,n}\left(\nabla(\omega_\gamma^\zeta F_\gamma)\right)-\sum_{\gamma=l,g}\left(\nabla(J_\gamma^\zeta)\right)$ $+\sum_{\gamma=l,g,n}\left(\omega_\gamma^\zeta \dot{m}_\gamma\right)\ \ where\ \zeta=w,a,o,s$
diffusion-dispersive flux and advective	$F_\gamma=-\frac{\rho_\gamma k_{r\gamma} k_i}{\mu_\gamma}\left(\nabla P_\gamma+\rho_\gamma g z_g\right)\quad where\ \gamma=l,g,n$
Diffusive mass flux	$J_\gamma^\zeta=-\phi\tau_\gamma\rho_\gamma s_\gamma\frac{M^\zeta}{M^\gamma}D_\gamma^\zeta\left(\nabla\chi_\gamma^\zeta\right)\ \ for\ \gamma=l\ and\ \zeta=w,a,o,s$ $for\ \gamma=g\ and\ \zeta=w,a,o$

More information about STOMP simulator and its constitutive equations can be found from the users' guide[16].

The study was initially carried out on the simple 1-D reservoir models to support the hypothesis of CO_2-microemulsion injection for methane recovery from the gas hydrate reservoirs. In this step, the effects of various parameters such as CO_2-microemulsion temperature, concentration of CO_2-slurry and absolute permeability of the formation rock were examined. In this case, CO_2-microemulsion injection was considered

from the West boundary of the system whereas the methane was produced from the East boundary of the system. The conclusions from this examination are summarized below:

- The simple 1-D analysis supports the hypothesis of enhanced gas-hydrate recovery method using a CO_2-microemulsion injection technique.
- Nearly pure methane was produced which is consistent with the observations from laboratory experiments.
- The results indicate that higher hydraulic conductivity results in much faster methane production. Accordingly, fracturing the formation to improve injectivity may be an effective way for improving methane production rate.

From the results from 1-D simulation study, it indicates the feasibility of using CO_2-microemulsion injection for methane recovery. The more complex 2-D reservoir models were then examined. In this case, the range of CO_2-microemulsion temperature and concentration for optimizing methane production were determined. Similarly, CO_2-microemulsion injection was considered from the West boundary of the system whereas the methane was produced from the East boundary of the system as shown in Figure 2-9.

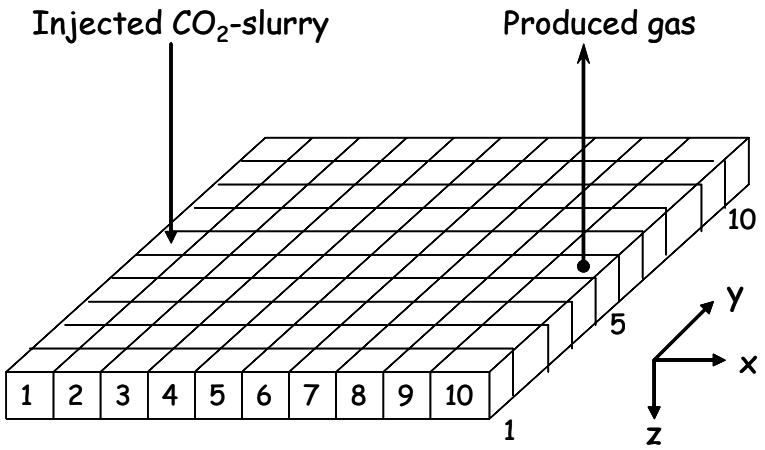

Figure 2-9: Schematic representation of 2-D reservoir model for STOMP-HYD simulator

The following conclusions could be drawn from this case study:

- Lower CO_2-slurry concentrations (up to 40-45%), higher methane recovery can be achieved for moderate CO_2-microemulsion temperatures.
- For moderate CO_2-slurry concentrations (about 50%), the amount of methane recovered increased with increase in CO_2-microemulsion temperature, and the maximum methane recovery was observed when temperature of CO_2-slurry was 28 ^{o}C.
- CO_2-slurry injection at moderate concentrations and higher temperatures might help in optimizing methane recovery.

2.4.12 Model 12, Uddin, Coombe, and Gunter's Model [17]

This work describes a new unified kinetic model, couple with a compositional thermal reservoir simulator (CMG STARS), that can simulate the dynamics of CH_4 and CO_2 hydrates formation and decomposition in a geological formation. The kinetic model contains two mass transfer equations: 1) formation equation transfers gas and water into hydrate, and 2) decomposition equation transfers hydrate into free gas and water.

In this work, the proposed model was evaluated in two case studies. In case 1, a single well natural hydrate reservoir was examined for studying the kinetics of CH_4 and CO_2 hydrates formation and decomposition In this case, the a detailed parameter sensitivity analysis was performed. In case 2, a multi-well reservoir was examined for studying the unified kinetic model to demonstrate the flexibility of CO_2 sequestration in a natural hydrate reservoir with potential enhancement of methane recovery. In this case, limitations of the numerical model to simulate the CO_2 sequestration processes in gas hydrate reservoirs were identified and suggestions for future model development were recommended.

The unified kinetic model which can handle CH_4 and CO_2 hydrates formation and/or decomposition has been developed in this work. In this model, a system of first order rate equations (kinetic equations for water, methane, CO_2, CH_4 hydrate, and CO_2 hydrate) was formulated for the kinetics of hydrate formation and decomposition. The equations of hydrate formation (forward kinetic) and hydrate decomposition (backward kinetic) rates are listed in Table 2-12.

Table 2-12: Hydrate formation and decomposition rate models used in Uddin et al.'s work

	Equations
Rate of hydrate formation	$\left.\frac{dc_H}{dt}\right\|_{Form} = A \cdot \exp(-\frac{E}{RT})(\phi S_a \rho_a)(\phi S_H \rho_H)(y_i p_g)\left(1-\frac{1}{K(p,T)}\right)$
Rate of hydrate decomposition	$\left.\frac{dc_H}{dt}\right\|_{Decomp} = B \cdot (1+\phi S_H) \cdot \exp(-\frac{E}{RT})(\phi S_a \rho_a)(y_i p_g)\left(1-\frac{1}{K(p,T)}\right)$

The following conclusions can be drawn from this study:

From case study 1:

- The effect of kinetic rate constants to the CH_4 and CO_2 hydrates decomposition were not significant.
- The effect of reservoir permeability on hydrate formation and decomposition is significant. The rapid pressure drawdown in high permeable system results a large areas of hydrate formation and decomposition.
- The hydrate formation with gas injection reduces the effective porosity and permeability around the injection well. The continuation of gas injection could lead into an unstable pressure-temperature condition around the injection well.

From case study 2:

- The unified gas hydrate model effectively describes the dynamics of gas hydrate formation and decomposition under varied kinetics, thermodynamics and

hydrodynamics conditions. The CH_4 and CO_2 hydrates can form and are stable under specific ranges of elevated gas pressure and temperature conditions. This depends upon several variables such as permeability, porosity, water salinity, as well as other petrophysical parameters.

The overall genealogy of the gas hydrate reservoir simulation models reviewed in this thesis are shown in Figure 2-10, Figure 2-11, and Table 2-13.

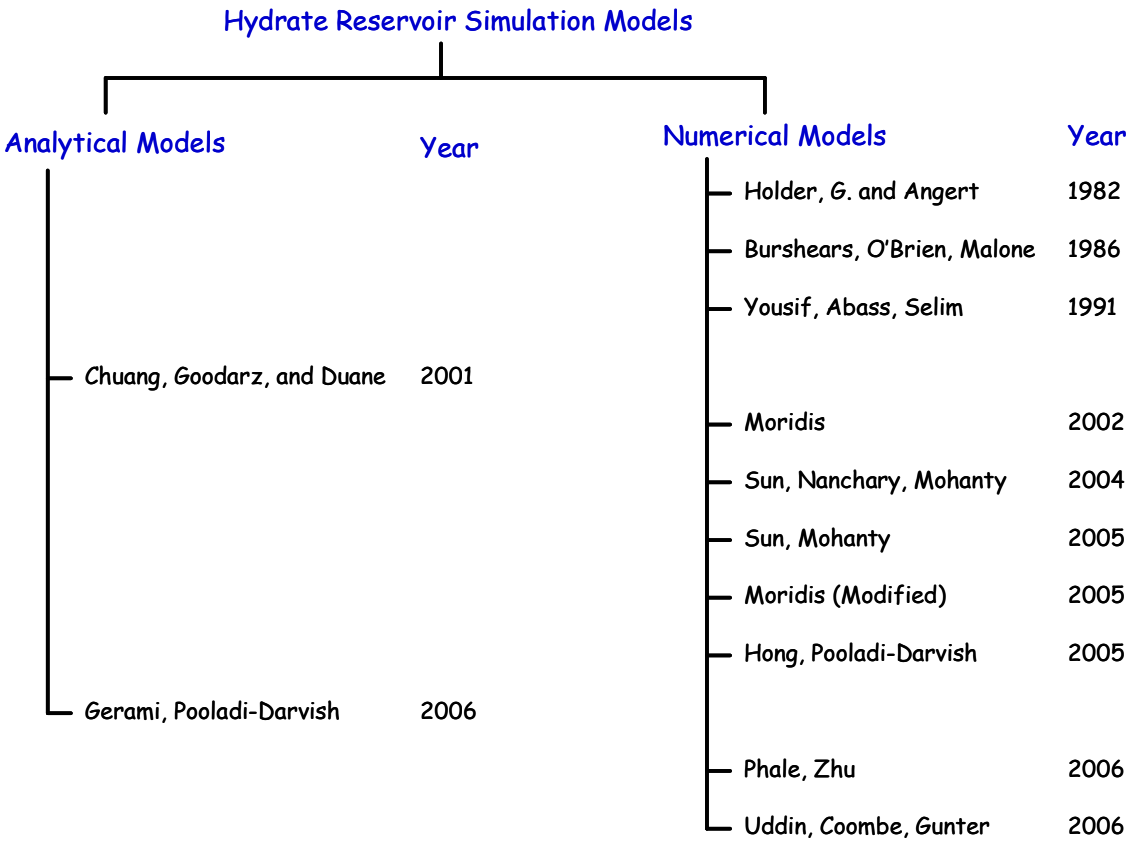

Figure 2-10: Overall relationships of the reviewed models

Note that one of the objectives of this study is to develop a numerical simulation model of gas hydrate reservoir. Therefore, the literature review of this study focused more on the numerical models.

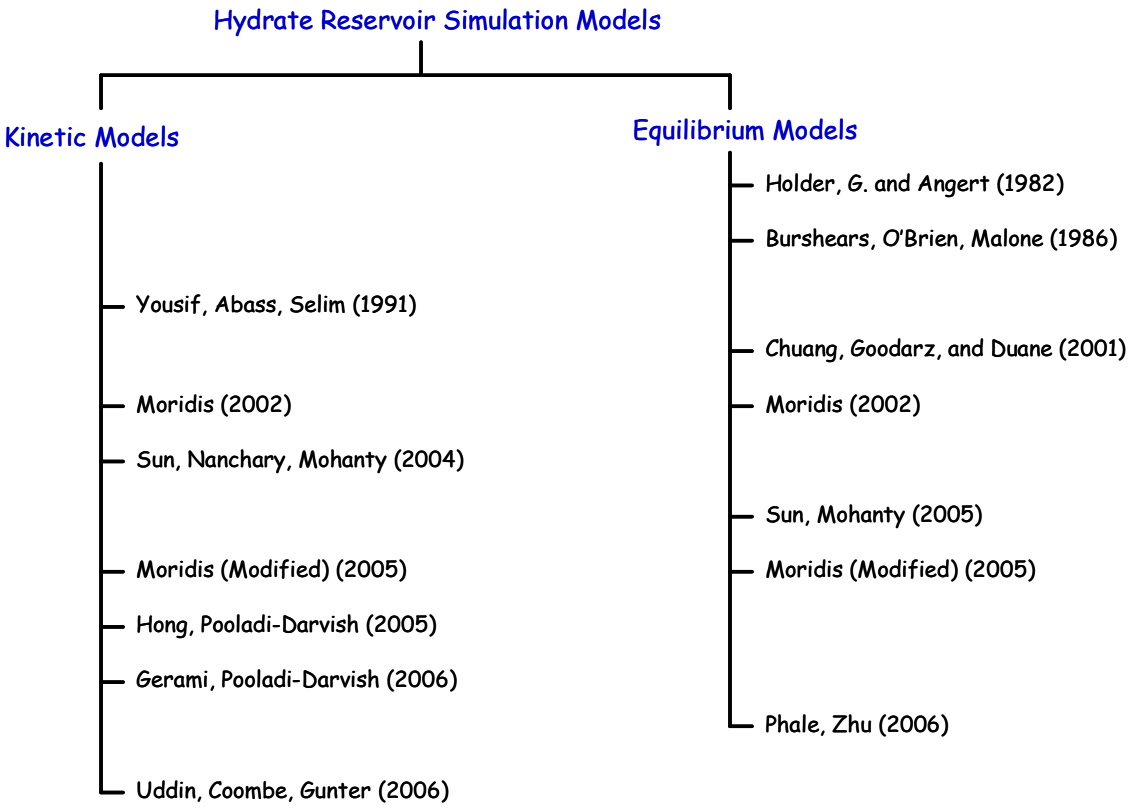

Figure 2-11: Types of the reviewed hydrate reservoir simulation models

Table 2-13: Model comparison

Models	Coordinate system	Model type	Field scale	Heat of conduction	Heat of convection	Kinetics model	Equilibrium model	Production scheme
Holder, G. and Angert	3-D Cartesian	Numerical	Y	Y	N	N	Y	Depressurization
Burshears, O'Brien, Malone	3-D Cartesian	Numerical	Y	Y	N	N	Y	Depressurization
Yousif, Abass, Selim	1-D Cartesian	Numerical	N	N	N	Y	N	Depressurization
Chuang, Goodarz, and Duane	1-D Cartesian	Analytical	Y	N	N	N	Y	Depressurization
Moridis	3-D Cylindrical/Cartesian	Numerical	Y	Y	Y	Y	Y	Depressurization/Thermal stimulation
Sun, Nanchary, Mohanty	1-D Cartesian	Numerical	Y	Y	Y	Y	N	Depressurization
Sun, Mohanty	3-D Cartesian	Numerical	Y	Y	Y	N	Y	Depressurization
Moridis (Modified)	3-D Cylindrical/Cartesian	Numerical	Y	Y	Y	Y	Y	Depressurization/Thermal stimulation
Hong, Pooladi-Darvish	2-D Cylindrical	Numerical	Y	Y	Y	Y	N	Depressurization
Gerami, Pooladi-Darvish	Non-dimensional	Analytical	Y	Y	N	N	Y	Depressurization
Phale, Zhu	3-D Cartesian	Numerical	Y	Y	Y	N	Y	CO_2 sequestration
Uddin, Coombe, Gunter	3-D Cartesian	Numerical	Y	Y	Y	Y	N	CO_2 sequestration
This study	3-D Cartesian	Numerical	Y	Y	Y	N	Y	Depressurization

CHAPTER 3

PROBLEM STATEMENT

Methane-hydrate reservoir behavior can not be effectively modeled using conventional two-phase fluid flow formulations. Proper modeling requires a methane-hydrate equilibrium model to be coupled with the formulation of fluid flow in porous media. The methane-hydrate equilibrium model predicts whether methane hydrate phase is stable at any particular pressure and temperature values. In addition, the dissociation of methane hydrate is an endothermic reaction. For this reason, the system cannot be treated as an isothermal system.

There are three main production methods for methane-hydrate reservoir which are depressurization, thermal stimulation, and inhibitor injection. A major feasibility constraint for all recovery methods is their economic implication. The thermal stimulation method has the terrible flaw of the tremendous amount the associated energy losses taken by the surroundings and the injection systems. Because of this, only a fraction of the injected energy finally meets the hydrate; and from this fraction, part of it is taken by the matrix of the rock. Moreover, penetration of hot fluids or inhibitors may become virtually impossible for very tight hydrate formations. Altogether, depressurization has stood as the most viable recovery method from an economic prospective.

During the gas production by depressurization, the decrease of reservoir temperature is likely to be observed because some energy is used for the dissociation of

methane hydrate. The decrease of reservoir pressure will start the dissociation of methane hydrate in the reservoir when reservoir pressure becomes equal to or lower than the dissociation pressure of methane hydrate, the pressure which methane hydrates become unstable, at reservoir temperature. However, the dissociation pressure of methane hydrate exponentially decreases with temperature drop. If the decrease of the dissociation pressure of methane hydrate (due to the reduction of reservoir temperature) in the reservoir is faster than the decrease of reservoir pressure, the dissociation of methane hydrate will not occur. Therefore, the changes of temperature and pressure of the system clearly control the recovery mechanism of methane hydrates in reservoirs.

All the reservoir simulation studies of gas-hydrate reservoirs which have been done so far focused on the feasibility study of gas production (by depressurization and heat stimulation) from gas-hydrate reservoirs. In this study, the effects of production parameters such as well-penetrating location and well spacing on the gas production efficiency are examined. This work mainly focuses on a constant bottom-hole pressure production scheme.

A gas-hydrate reservoir simulator developed by Lawrence Berkeley National Laboratory[10] , *TOUGH FX* simulator, was launched to public in 2005. Unfortunately, a well bore model has not been incorporated into the simulator resulting in the limitations of the simulator to be used for studying gas production characteristics from different production strategies. For a multilayer well with constant gas flow rate specification case, the gas flow rate of each layer must be specified in the *TOUGH FX* simulator and these specified flow rates do not change for the entire simulation which is not accurate. The incorporation of wellbore model improves the accuracy of the simulation results. In the

case that a wellbore model is incorporated in the model, the gas and aqueous flow rates of each layer change corresponding to the mobilities of aqueous and free gas phases in each layer, and the total gas flow rate is equal to the specification value. Moreover, the study of production characteristics for a constant bottom-hole pressure production scheme can not be performed without a wellbore model. Therefore, a new methane-hydrate reservoir simulator which is capable of simulating production characteristics from different production schemes is developed in this work and it is used for exploring production characteristics of class 1 methane-hydrate reservoirs.

CHAPTER 4

HYDRATE CRYSTAL CELL STRUCTURES AND PHASE EQUILIBRIUM MODELS OF GAS HYDRATES

4.1 Crystal Cell Structures of Gas Hydrates[3,18]

Gas hydrates are crystalline molecule complexes formed from mixtures of water and suitably sized gas molecules. Water (host) molecules form unstable lattice structures, upon hydrogen bonding, with several cavities. Gases (guest) molecules can occupy the lattice cavities and when the minimum numbers of cavities are occupied, the crystalline structure becomes stable even at temperatures well above the water freezing point. Gas hydrates are formed.

The two common forms of gas hydrates known as structure *I (sI)* and *II (sII)* have been investigated using X-ray diffraction methods by Von Stackelberg and Müller (1954). They found that the unit cell of hydrate structure *I* is a 12 ^{o}A cube consisting of 46 water molecules which has two cavity types: small and large cavities. There are two small cavities and six large cavities in a unit cell of hydrates structure *I*. The small cavity is pentagonal dodecahedra, whereas the large cavity is tetradecanhedra. Jeffrey (1984) suggested the nomenclature description ($n_i^{m_i}$), where n_i is the number of edges in the *I* type of face and m_i is the number of faces of *i* type. Thus the small cavity for hydrate structure *I* is denoted 5^{12} because it has twelve pentagonal and two hexagonal faces, whereas the large cavities for this structure is denoted $5^{12}6^2$ because it has twelve

pentagonal and two hexagonal faces. The smaller cavities are almost spherical, whereas the larger cavities are slightly oblate.

The unit cell of structure *II (sII)*, which is a 17.3 ^{o}A cube with 136 water molecules, also contains two types of cavities. The 16 small cavities are distorted pentagonal dodecahedra (5^{12}), and the 8 large cavities are hexadecahedra ($5^{12}6^{4}$) having 4 hexagonal faces and twelve pentagonal faces. The latter cavities are almost spherical in shape.

Ripmeester et al. (1987) reported a new hexagonal hydrate structure which requires both large and small molecules to stabilize the structure. They proposed that the new structure is known as structure *H (sH)*. According to Ripmeester, the unit cell consists of 34 water molecules forming a hexagonal lattice. This structure has three different types of cavities. It consists of three 5^{12} cavities which is common to all known hydrate structures, two new 12 faces $4^{3}5^{6}6^{3}$ cavities and one new large $5^{12}6^{8}$ cavity. The $4^{3}5^{6}6^{3}$ cavity has three square faces, six pentagonal faces, and three hexagonal faces. The $5^{12}6^{8}$ cavity has twelve pentagonal faces and eight hexagonal faces. The first two cavities accommodate the small molecules. The large cavities can accommodate even larger molecules, so that the molecules in the size range of 7.5 to 8.6 ^{o}A can potentially form this type of gas hydrate structure. The cavities in each hydrate structure are shown in Figure 4-1.

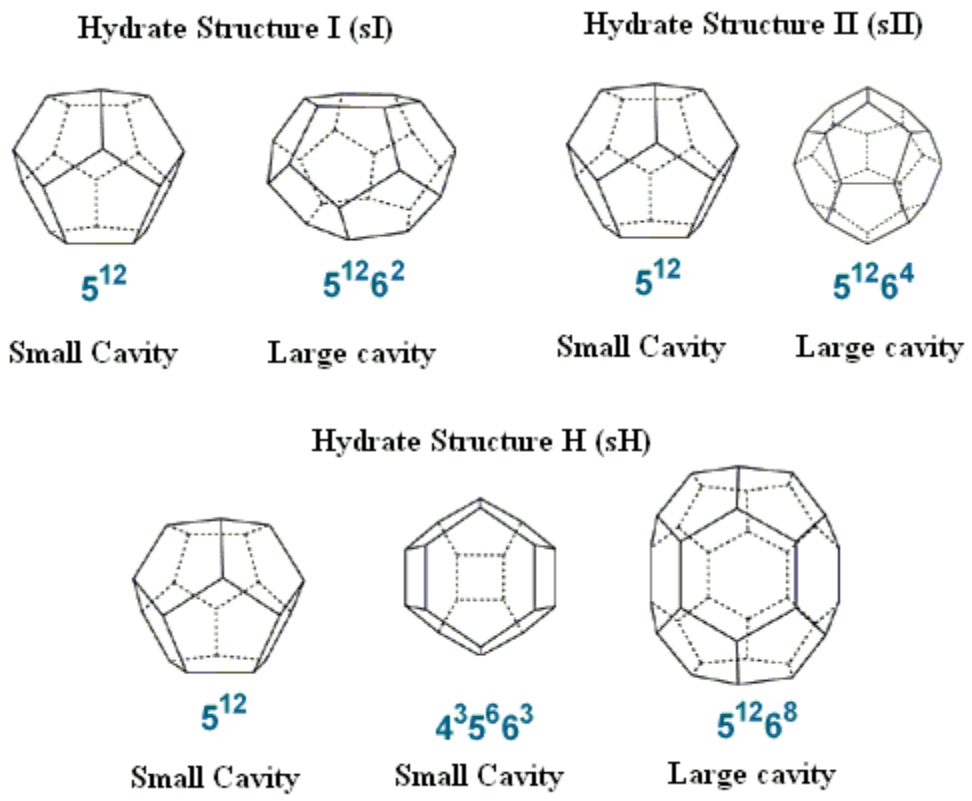

Figure 4-1: Structures of cavity types in hydrate structures[18]

In all hydrate structures, each cavity can contain at most one guest molecule. There have been no documented experiments where cavities were observed to be occupied by more than one guest molecule. The comparison between the sizes of cavities and guest molecule, a revision of a figure originally by von Stalkelberg, is shown in Figure 4-2 [3]. As indicated in the Figure 4-2, molecules of transitional size (shaded regions) such as cyclopropane and trimethylene oxide, which have diameters of 5.8 ^{o}A and 6.1 ^{o}A, respectively, may form either structure *I* or structure *II*.

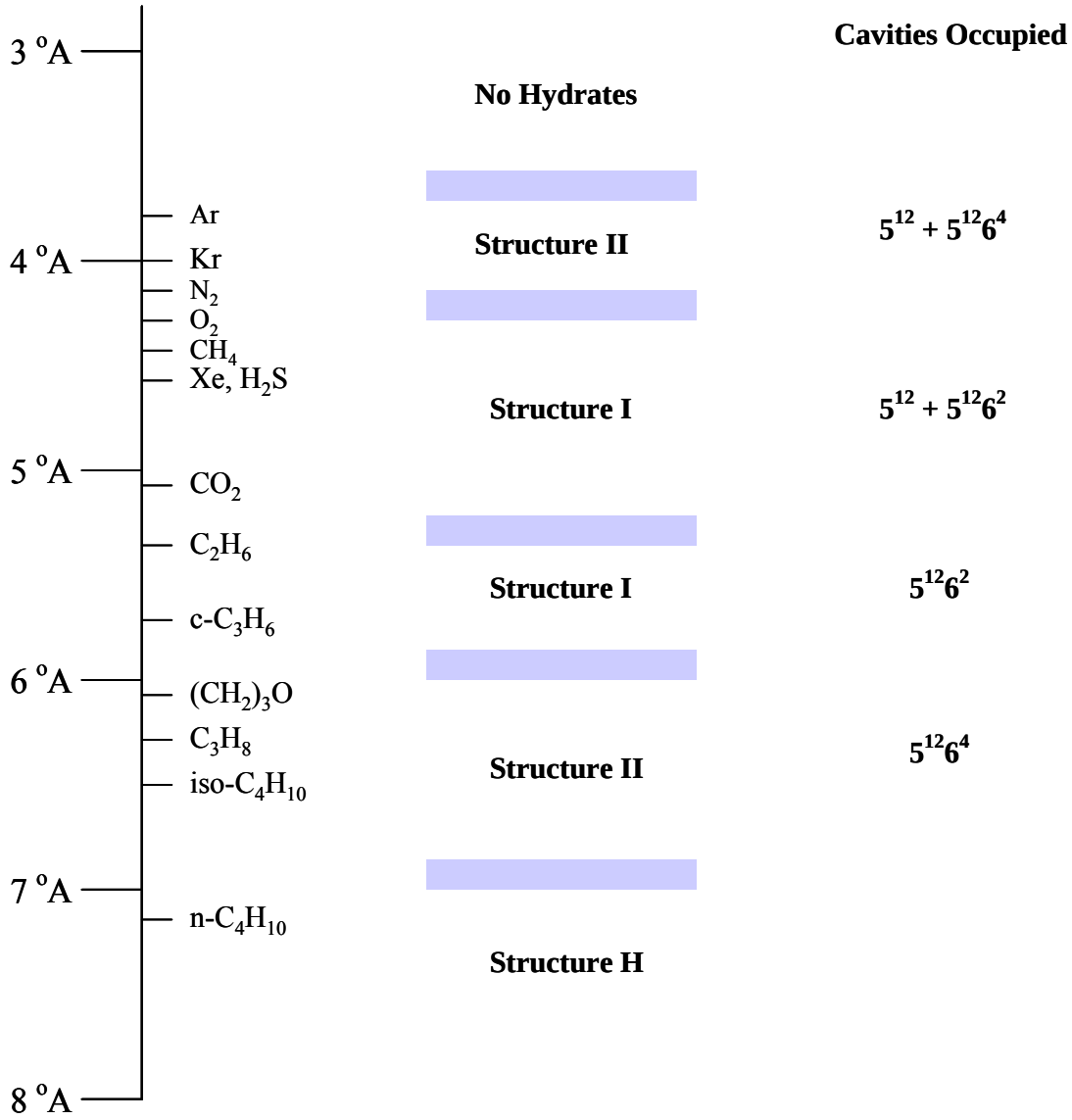

Figure 4-2: Comparison between guest molecule and cavity sizes[3]

4.2 Hydrate Phase Equilibrium Models

A hydrate phase equilibrium model was developed in order to determine the dissociation pressure of hydrates at a particular temperature. The dissociation pressure is used for calculating the rate of gas and water released from the dissociation reaction.

Hydrate phase equilibrium models could be developed from two different methods. The first method uses the statistical thermodynamic concept to set up the model. Another method uses the regression analysis to set up the models from available experimental data. In this chapter, some empirical correlations and the statistical thermodynamic model are discussed.

4.2.1 Statistical Thermodynamic Model

The model used in this study was based on classical statistical thermodynamics proposed by Van der Waals and Plateeuw[19] in 1959. The method for predicting equilibrium was based on the criterion of equality of chemical potential of water in hydrate and water rich (or ice) phases. Using μ_β, the chemical potential of an unoccupied hydrate lattice, as the reference state, the equilibrium condition can be written as:

$$\mu_\beta(T,P) - \mu_w(T,P) = \mu_\beta(T,P) - \mu_H(T,P) \quad 4.1$$

$$\Delta\mu_w = \Delta\mu_H \quad 4.2$$

where μ_w is the chemical potential of water in water rich (or ice) phase

μ_H is the chemical potential of water in hydrate phase

4.2.1.1 Calculation of $\Delta\mu_w$

The water-rich phase chemical potential difference as a function of pressure and temperature can be written as:

$$d\left(\frac{\Delta\mu_w}{RT}\right) = -\left(\frac{\Delta h_w}{RT^2}\right)dT + \left(\frac{\Delta V_w}{RT}\right)dP \qquad 4.3$$

where Δh_w is the enthalpy difference between water (or ice) and empty-hydrate lattice

ΔV_w is the volume difference between water (or ice) and empty-hydrate lattice

Holder *et al.*[20] provided a simple method to determine the effects of temperature, pressure, and gas composition on $\Delta\mu_w$ using the following expression:

$$\frac{\Delta\mu_w}{RT} = \frac{\Delta\mu_w^o}{RT_o} - \int_{T_o}^{T}\left(\frac{\Delta h_w}{RT^2}\right)dT + \int_0^P\left(\frac{\Delta V_w}{RT}\right)dP - \ln\left(x_w\gamma_w\right) \qquad 4.4$$

where $\Delta\mu_w^o$ is the chemical potential difference between the empty-hydrate lattice and water phase at the reference state (0 kPa, 273.15 K)

T_o is the reference temperature (273.15 K)

x_w is the mole fraction of water in water rich phase

γ_w is the activity coefficient of water rich phase

The first term on the right hand side of the above equation represents the chemical potential difference between the theoretical empty hydrate and liquid water (or ice) at its reference state. The second term accounts for the change in chemical potential difference due to temperature at zero pressure. The third term accounts for the change in chemical

potential difference due to pressure. The last term accounts for the solubility of gas in water rich phase. The activity coefficient of water rich phase accounts for the non-idealities of the water rich phase. The activity coefficient of water rich phase was assumed to be 1.0 when only gas and water systems were studied because the gas solubility in water is generally small.

The enthalpy difference, Δh_w, is calculated from the following equation:

$$\Delta h_w = \Delta h_w^o + \int_{T_0}^{T} \Delta c_{pw} dT \qquad 4.5$$

where Δh_w^o is the reference enthalpy difference between water (or ice) and empty-hydrate lattice

Δc_{pw} is the heat capacity difference between water (or ice) and empty-hydrate lattice

The heat capacity difference is calculated from the following relationship:

$$\Delta c_{pw} = \Delta c_{pw}^o + b(T - T_0) \qquad 4.6$$

where Δc_{pw}^o is the reference heat capacity difference

b is a constant

The values of $\Delta \mu_w^o$, Δh_{pw}^o, and Δc_{pw} used in this study are listed in Table 4-1. The value of ΔV_w in equation (4.4) is a constant and it depends on the type of phase present in the system (water or ice phase).

Table 4-1: Values of $\Delta\mu_w^o$, Δh_{pw}^o, and Δc_{pw} used in this study[3]

Parameters	T_0 = 273.15 K	
$\Delta\mu_w^o$ (J/mol)	1220	
Δh_w^o (J/mol-K)	$T > T_0$	-4,300
	$T \le T_0$	1270
Δc_{pw} (J/mol-K)	$T > T_0$	-38.12 + 0.141 (T- T_0)
	$T \le T_0$	3.20 + 0.121 (T- T_0)

The value of mole fraction of water in water rich phase in the last term in equation (4.4) can be calculated from the following equation:

$$x_w = 1 - \sum_{k=1}^{nc} x_k \qquad 4.7$$

The variable x_k is the mole fraction of dissolved gas component k in water rich phase. The solubility of gas in water is determined by using Krichevsky-Kasarnovsky expression[3]:

$$x_k = \frac{f_k}{H_k \cdot \exp(PV_k^\infty / RT)} \qquad 4.8$$

Here V_k^∞ is the volume of gas component k in water at infinite dilution. The value of H_k can be calculated using the following equation:

$$-\ln(H_k) = \frac{H_k^0}{R} + \frac{H_k^1}{RT} + \frac{H_k^2}{R}\ln(T) + \frac{H_k^3}{R}T \qquad 4.9$$

The units of H_k and T in this equation are "atm" and "Kelvin", respectively. The values of Henry's coefficients (H_k^0, H_k^1, H_k^2, and H_k^3) and V_k^∞ for methane are summarized in Table 4-2.

Table 4-2: Henry's constants and V_k^{∞} values[3]

Component	H^o	H^1	H^2	H^3	V^{∞} (cm^3/mol)
Methane	-365.183	18,016.7	49.7554	-0.000285	32
Ethane	-533.392	26,565.0	74.6240	-0.004573	32
Propane	-628.866	31,638.4	88.0808	0.000000	32
i-Butane	190.082	-4,913.0	-34.5102	0.000000	32
n-Butane	-639.209	32,785.7	89.1483	0.000000	32
H_2S	-297.158	16,347.7	40.2024	0.002571	32
N_2	-327.850	16,757.6	42.8400	0.016765	32
CO_2	-317.658	17,371.2	43.0607	-0.002191	32

4.2.1.2 Calculation of $\Delta\mu_H$

The value of $\Delta\mu_H$ can be calculated from the following equation purposed by Van der Waals and Platteeuw[19]:

$$\Delta\mu_H = -RT\sum_j^n \nu_j \ln(1-\sum_i^{nc} y_{ij}) \qquad 4.10$$

Here y_{ij} is the fractional occupancy of the cages defined as the fraction of the cavity type "*j*" by the guest molecule "*i*". The parameter ν_j is the number of cavity type "*j*" per water molecule in the hydrate structure. For structure *I* of hydrate lattice, there are two cavity types (small and large cavities). The value of ν_1 (small cavity) and ν_2 (large cavity) for structure *I* of hydrate lattice are 1/23 and 3/23, respectively. The parameters "*nc*" and "*n*" in this equation are the number of guest components and the number of cavity types in the hydrate structure. The value of y_{ij} is calculated from the following Langmuir's isotherm equation:

$$y_{ij} = \frac{C_{ij}\, f_i}{1 + \sum_{k}^{nc} C_{kj}\, f_k} \qquad 4.11$$

where C_{ij} is the Langmuir constant of hydrate former "i" in cavity type "j"

f_i is the gas phase fugacity of hydrate guest component "i"

In this study, the Peng-Robinson Equation of State is used for evaluating the gas phase fugacity of guest component. Van der Waals and Platteeuw[19] suggested the use of Lennard-Jones potential to represent the interaction between enclathrated gas and hydrate lattice water molecules in their original work. However, Lennard-Jones potential is satisfactory only for guest components which are small spherical molecules. The use of Kihara Potential function is recommended[3] since it gives better results for larger poly-atomic and rod-like molecules. Van der Waals and Platteeuw assumed that only nearest neighbor water molecules had an effect on the energy of the enclathrated gas molecule[19]. The Kihara parameter values given by Sloan[3] are used in this study. The values of Kihara parameters for methane are listed in Table 4-3. The values of radius (R) and coordination number (Z) are listed in Table 4-4. The Langmuir constant for component "n" in cavity type "j" is calculated from the following equation:

$$C_{ij} = \frac{4\pi}{kT} \int_{0}^{R-a_i} \exp\left(-\frac{W_{ij}(r)}{kT} \right) r^2\, dr \qquad 4.12$$

where W_{ij} is the cell potential for guest component "i" in cavity "j"

The cell potential can be calculated from the following expression:

$$W_{ij}(r) = 2Z_j\varepsilon_i\left[\frac{\sigma_i^{12}}{R_j^{11}r}(\delta_{ij}^{10}+\frac{a_i}{R_j}\delta_{ij}^{11}) - \frac{\sigma_i^{6}}{R_j^{5}r}(\delta_{ij}^{4}+\frac{a_i}{R_j}\delta_{ij}^{5})\right] \quad 4.13$$

where,

$$\delta_{ij}^{m} = \frac{1}{m}\left[(1-\frac{r}{R_j}-\frac{a_i}{R_j})^{-m} - (1+\frac{r}{R_j}-\frac{a_i}{R_j})^{-m}\right] \quad 4.14$$

Superscript *m* in equation (4.14) is equal to 4, 5, 10, and 11. R_j and Z_j are the cavity radius and coordination number for cavity type "*j*", respectively. Parameters σ_i, a_i, and ε_i are the Kihara parameters for guest component "*i*", and *r* is the distance of the guest molecule from the center of the cavity.

4.2.1.3 Numerical Scheme

Equation (4.2) can be rewritten in the following form:

$$F(P,T) = \Delta\mu_w - \Delta\mu_H = 0 \quad 4.15$$

Substitution of equation (4.4) and (4.10) into equation (4.15) yields:

$$F(P,T) = \left[\frac{\Delta\mu_w^o}{T_o} - \int_{T_o}^{T}\left(\frac{\Delta h_w}{T^2}\right)dT\right]T + \Delta V_w P - RT\ln(x_w\gamma_w) + RT\sum_j^n \nu_j \ln(1-\sum_i^{nc} y_{ij}) = 0 \quad 4.16$$

In this study, equation (4.16) is used to calculate the hydrate association pressure at a given temperature. Since, equation (4.16) is a non-linear function. It can be solved using Newton-Raphson Method through the following procedure:

$$P^{k+1} = P^k - \frac{F(P,T)}{F'(P,T)} \qquad 4.17$$

where $F'(P,T)$ is the derivative of *F(P,T)* with respect to pressure. The solution is obtained when $| P^{k+1} - P^k | < \varepsilon$ and ε is a convergent tolerance.

The comparison between the dissociation pressures obtained from the statistical thermodynamic model and the experimental data provided by Sloan[3] at various temperatures for methane hydrate is shown in Figure 4-3.

Table 4-3: Kihara parameters for guest molecules[3]

Component	σ (A^o)	ε/k (K)	a (A^o)
Methane	3.1650	154.54	0.3834
Ethane	3.2641	176.40	0.5651
Propane	3.3093	203.31	0.6502
i-Butane	3.0822	225.16	0.8706
n-Butane	2.9125	209.00	0.9379
N_2	3.0124	125.15	0.3526
CO_2	2.9818	168.77	0.6805

Table 4-4: Cavity radius and coordination number[3]

	Structure I			Structure II		
	Radius (^{o}A)	Z	υ	Radius (^{o}A)	Z	υ
Small cavity	3.91	20	39105	3.902	20	39130
Large cavity	4.33	24	39164	4.683	28	39099

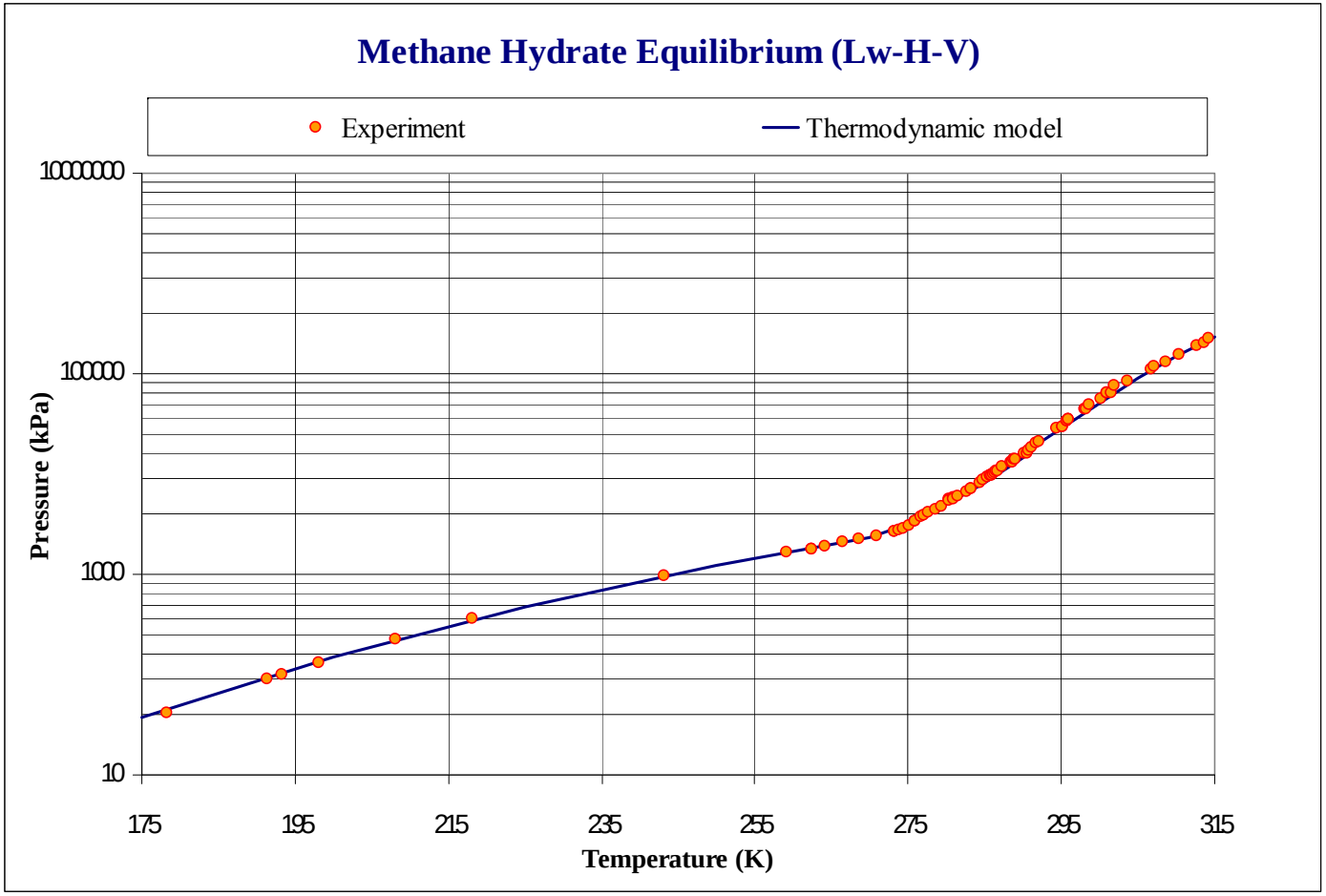

Figure 4-3: Methane hydrate dissociation pressure from statistical thermodynamic model and experimental data[3]

4.2.2 Empirical Correlations

There are several hydrate equilibrium models using regression technique developed during the past decades. Some of these models are summarized below:

4.2.2.1 Kamath's correlation[22]

Kamath proposed the following correlation between temperature, T, and dissociation pressure, P_e, for gas hydrates:

$$P_e = \exp\left(e_1 + \frac{e_2}{T}\right) \qquad 4.18$$

Here P_e is the dissociation pressure (kPa), T is temperature (K), and e_1 and e_2 are empirical constants. The values of empirical constants in the equation for methane hydrate are summarized in Table 4-5.

Table 4-5: Empirical constants in Kamath's correlation for methane hydrate[22]

Component	*Temperature*	e_1	E_2
Methane	273.15 < T ≤ 298.15 K	38.98	-8533.80
	248.15 ≤ T ≤ 273.15 K	14.717	-1886.79

4.2.2.2 Makogon's correlation[23]

The regression equation proposed by Makogon is expressed as:

$$\log_{10} P_e = a(T - T_0) + b\,(T - T_0)^2 + c \qquad 4.19$$

where T_0 is 273.15 K and a, b, c are empirical constants that depend on hydrate composition. The units of P_e and T are Pascal and Kelvin, respectively. The values of constants for methane hydrate are listed in Table 4-6.

Table 4-6: Empirical constants in Makogon's correlation for methane hydrate[23]

Component	a (1/K)	b (1/K^2)	c
Methane	0.0342	0.0005	6.4804

4.2.2.3 Moridis's correlation[24]

This correlation is developed by regression technique from the methane-hydrate equilibrium data provided by Sloan[3]. The correlation is shown in the following equation:

$$\ln P_e = aT^5 + bT^4 + cT^3 + dT^2 + eT + f \qquad 4.20$$

The units of P_e and T in this equation are MPa and K, respectively. The values of empirical constants in the equation are listed in Table 4-7.

The comparison of predicted methane hydrate dissociation pressures at various temperatures from these three empirical correlations is shown in Figure 4-4.

Table 4-7: Empirical constants in Moridis' correlation for methane hydrate[24]

Empirical constants	***Temperature (K)***	
	150 K ≤ T ≤ 273.15 K	***273.15 < T ≤ 315 K***
a	$1.09882180475307 \times 10^{-10}$	$8.86065316687571 \times 10^{-8}$
b	$-1.03669656828834 \times 10^{-7}$	$-1.30465829788791 \times 10^{-4}$
c	$3.85413985900724 \times 10^{-5}$	$7.67559117787059 \times 10^{-2}$
d	$-7.27291427030502 \times 10^{-3}$	$-2.25540264493806 \times 10^{1}$
e	$7.76302133739303 \times 10^{-1}$	$3.31018213397926 \times 10^{3}$
f	$-4.38921173434628 \times 10^{1}$	$-1.94138504464560 \times 10^{5}$

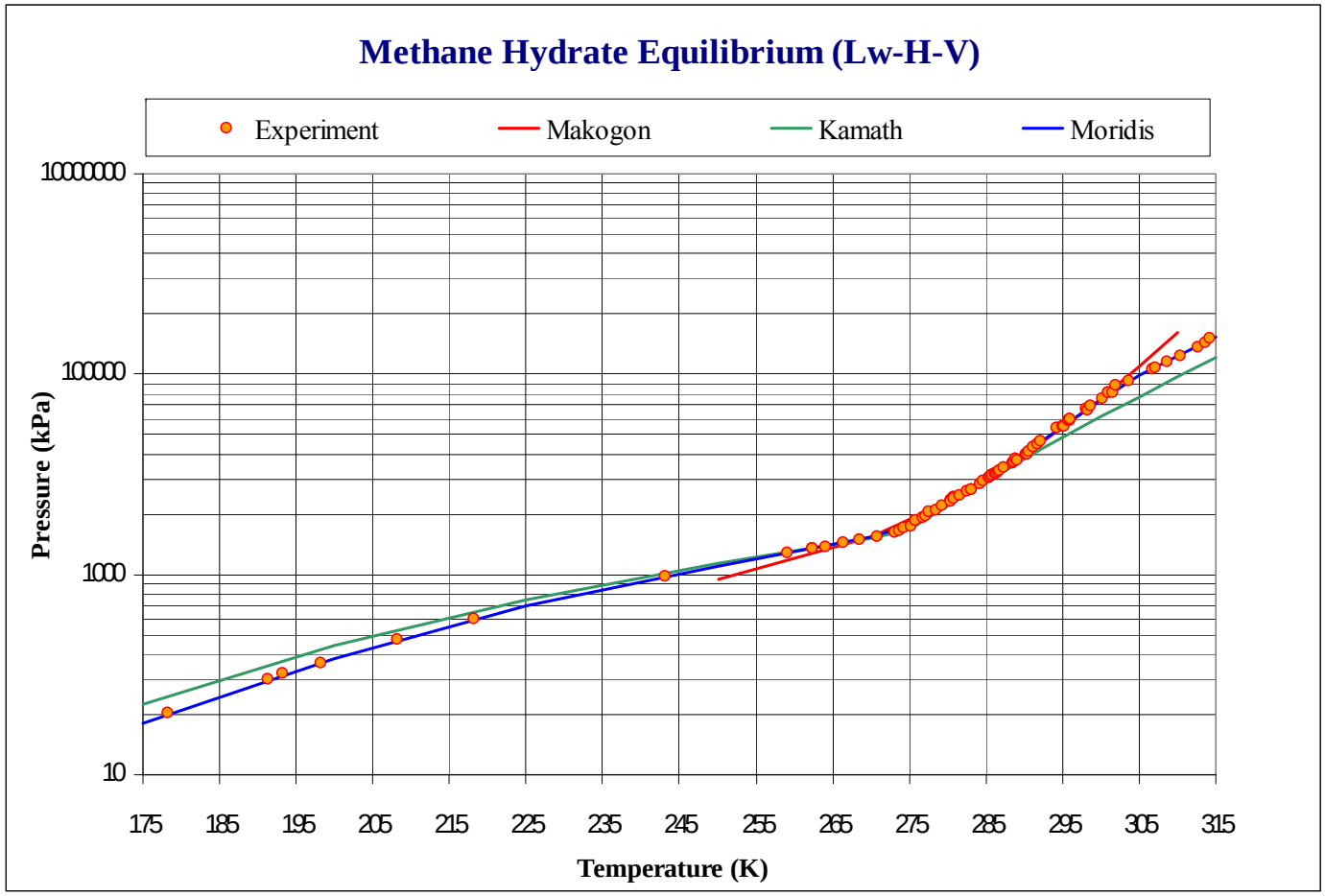

Figure 4-4: Methane hydrate dissociation pressures from various empirical correlations and experimental data[3]

CHAPTER 5

MODEL DEVELOPMENT

5.1 Model Conceptualization and Governing Equations

The mathematical model for multiphase flow in gas-hydrate reservoir can be developed using mass and energy conservation equations for the three-dimensional system shown in Figure 5-1.

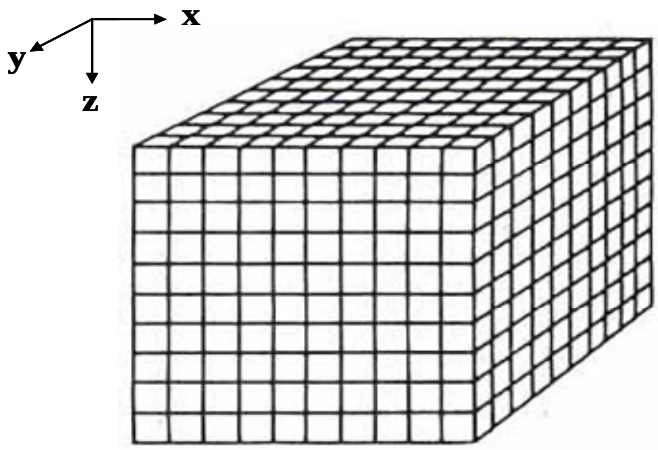

Figure 5-1: Discretized rectangular grid system

In this study, the system was modeled as a four-phase (gas, water, ice, and hydrate phases) system where only two components (methane and water) were to be found at any point in the system. The amount of methane dissolved in aqueous phase and the amount of water vapor in free gas phase were taken into account. However, ice phase was assumed to be methane-free. Only aqueous and free gas phases were mobile. The phase

change between aqueous and ice phase were assumed to be instantaneous once freezing conditions were attained. Rocks were assumed to be rigid. In this model, the dissociation of methane hydrate was assumed to be instantaneous. The model can handle phase appearance/disappearance situation. The governing flow equation of each component (methane and water) can be written as:

Methane

$$\frac{\partial}{\partial x}\left[y_m \overline{\rho}_g \frac{A_x k_x k_{rg}}{\mu_g}\left(\frac{\partial \Phi_g}{\partial x}\right) + x_m \overline{\rho}_a \frac{A_x k_x k_{ra}}{\mu_a}\left(\frac{\partial \Phi_a}{\partial x}\right)\right]\Delta x$$
$$+\frac{\partial}{\partial y}\left[y_m \overline{\rho}_g \frac{A_y k_y k_{rg}}{\mu_g}\left(\frac{\partial \Phi_g}{\partial y}\right) + x_m \overline{\rho}_a \frac{A_y k_y k_{ra}}{\mu_a}\left(\frac{\partial \Phi_a}{\partial y}\right)\right]\Delta y$$
$$+\frac{\partial}{\partial z}\left[y_m \overline{\rho}_g \frac{A_z k_z k_{rg}}{\mu_g}\left(\frac{\partial \Phi_g}{\partial z}\right) + x_m \overline{\rho}_a \frac{A_z k_z k_{ra}}{\mu_a}\left(\frac{\partial \Phi_a}{\partial z}\right)\right]\Delta z + \frac{Q_m}{5.615}$$
$$= \left(\frac{V_b}{5.615}\right)\frac{\partial}{\partial t}\left(y_m \phi S_g \overline{\rho}_g + x_m \phi S_a \overline{\rho}_a + N_m \phi S_H \overline{\rho}_H \right) \qquad 5.1$$

Water

$$\frac{\partial}{\partial x}\left[(1-y_m) \overline{\rho}_g \frac{A_x k_x k_{rg}}{\mu_g}\left(\frac{\partial \Phi_g}{\partial x}\right) + (1-x_m) \overline{\rho}_a \frac{A_x k_x k_{ra}}{\mu_a}\left(\frac{\partial \Phi_a}{\partial x}\right)\right]\Delta x$$
$$+\frac{\partial}{\partial y}\left[(1-y_m) \overline{\rho}_g \frac{A_y k_y k_{rg}}{\mu_g}\left(\frac{\partial \Phi_g}{\partial y}\right) + (1-x_m) \overline{\rho}_a \frac{A_y k_y k_{ra}}{\mu_a}\left(\frac{\partial \Phi_a}{\partial y}\right)\right]\Delta y$$
$$+\frac{\partial}{\partial z}\left[(1-y_m) \overline{\rho}_g \frac{A_z k_z k_{rg}}{\mu_g}\left(\frac{\partial \Phi_g}{\partial z}\right) + (1-x_m) \overline{\rho}_a \frac{A_z k_z k_{ra}}{\mu_a}\left(\frac{\partial \Phi_a}{\partial z}\right)\right]\Delta z + \frac{Q_w}{5.615}$$
$$= \left(\frac{V_b}{5.615}\right)\frac{\partial}{\partial t}\left((1-y_m)\, \phi S_g \overline{\rho}_g + (1-x_m)\, \phi S_a \overline{\rho}_a + \phi S_I \overline{\rho}_I + N_w \phi S_H \overline{\rho}_H \right) \qquad 5.2$$

The derivation of these two molar balance equations is shown in Appendix A.

The parameters $\overline{\rho}_g$ and $\overline{\rho}_a$ are molar density of free gas and aqueous phases. The parameters N_m and N_w in the equations are number of methane and water molecules in

methane hydrates, respectively. Parameters N_m and N_w are the constants that are known for a given hydrate structure. The value of N_w is 46 whereas the value of N_m is normally between 6 to 8 for the case of methane hydrate. Parameters x_m and y_m are mole fractions of methane in aqueous and free gas phases, respectively. The saturated value of dissolved methane gas in aqueous phase can be calculated from Henry's law because of the low concentration of methane gas in aqueous phase [10]:

$$x_m^{sat} = \begin{cases} \dfrac{P_g}{H_m} & if \ P_g < P_e \\ \dfrac{P_e}{H_m} & if \ P_g \geq P_e \end{cases} \qquad 5.3$$

The value of Henry constant for methane gas can be evaluated from[10]:

$$\ln(H_m) = 5.1345 + \frac{7837}{T} - \frac{1.509\times10^6}{T^2} + \frac{2.06\times10^7}{T^3} \qquad 5.4$$

where H_m is in Pascal and T is in Kelvin

The saturated molar fraction of water in gas phase is determined using partial pressure rule as the following expression:

$$y_g^{sat} = \frac{P^{\upsilon}}{P_g} \qquad 5.5$$

P_g is the gas phase pressure and P^{υ} is the water vapor pressure which can be calculated from the following equation[10]:

$$P^{\upsilon} = \begin{cases} \exp\left(73.649 - \dfrac{7258}{T} - 7.3037\ln T + 4.1653\times10^{-6}T^{2}\right), & T \geq 273.15\ K \\ \exp\left(15.6217 - \dfrac{6415.37}{T+5.5171}\right)\times10^{6}, & T < 273.15\,K \end{cases} \quad 5.6$$

where T is in Kelvin and P^{υ} is in Pascal

In this study, it is assumed that there is no fluid flow across the reservoir boundaries (no flow boundaries). The heat transfers in the x and y directions are negligible comparing to heat transfer in the z-direction because the temperature gradients in the z direction are much higher than the temperature gradients in the x- and y-directions. The heat transfer between reservoir and its surrounding can be modeled using heat conduction equation. Moreover, hydrate dissociation is an endothermic reaction. Accordingly, the system has to be treated as a non-isothermal system. Equation (5.7) is the energy balance equation used in this study, which takes into account heat transfer due to conduction and convection:

$$\frac{\partial}{\partial t}\left\{\phi(\rho_g S_g h_g) + \phi(\rho_a S_a h_a) + \phi(\rho_H S_H h_H) + (1-\phi)(\rho_r h_r)\right\}$$
$$= \nabla\cdot\left(K_h \nabla T\right) - \nabla\cdot\left[\rho_g v_g h_g + \rho_a v_a h_a\right] + \frac{(Q_E - Q_{dis} + Q_{fus})}{V_b} \quad 5.7$$

In equation (5,7), the variable K_h is the heat conductivity of formation. Q_E, Q_{dis}, and Q_{fus} are external heat source, heat of hydrate dissociation, and heat of fusion of ice, respectively. The value of heat of fusion of ice is 80 cal/g or 144 BTU/lb [28]. The variable v_l, and h_l are velocity and molar enthalpy of phase l, respectively.

The amount of methane-hydrate dissociation energy (based on 1 mole of released methane gas) can be calculated using the Clausius-Clapeyron equation [2]:

$$Q_{dis} = ZRT^2 \frac{d(\ln P)}{dT} \qquad 5.8$$

Here, Z is gas compressibility factor and $d(lnP)/dT$ can be determined from hydrate phase equilibrium relationship. The unit of Q_{dis} is J/kg-released methane gas and T is temperature in K.

Another empirical equation for calculating the dissociation energy of methane hydrate is[22]:

$$Q_{dis} = 13.521 - 0.00402\,T \qquad 5.9$$

where Q_{dis} = dissociation energy of methane hydrate in kcal/gmol CH_4

T = temperature in K

The molar enthalpy of water and gas phase in equation (5.7) at standard pressure (14.7 psia) can be calculated from:

$$h_i(T) = \int c_{pi} dT = c_{pi} T \qquad 5.10$$

where c_{pi} is the heat capacity of phase "i" at standard pressure.

In this work, the molar enthalpy of gas phase at pressure P and temperature T is calculated using the following expression:

$$\frac{h_g^{res}}{RT} = \frac{(h_g - h_g^{ig})}{RT} = -\int_0^P T\left(\frac{\partial Z}{\partial T}\right)\frac{dP}{P} + Z - 1 \qquad 5.11$$

where h_g = gas enthalpy at pressure P_g

h_g^{ig} = gas enthalpy at standard pressure

Z = gas compressibility factor at gas pressure P_g and temperature T

In this study, the ideal liquid behavior was assumed for aqueous phase. Accordingly, the molar enthalpy of water phase at high pressure is assumed to be equal to the water enthalpy at standard pressure.

In this work, the Peng-Robinson Equation of State is used for estimating the gas properties. Then, the molar gas enthalpy in equation (5.11) can be expressed as:

$$\frac{h_g^{res}}{RT} = \frac{(h_g - h_g^{ig})}{RT} = Z - 1 + \left(\frac{F(T_r)}{\sqrt{8}}\right)\ln\left(\frac{Z + (1+\sqrt{2})B}{Z + (1-\sqrt{2})B}\right) \qquad 5.12$$

where $A = aP/R^2T^2$

$B = bP/RT$

$a = a_c[1 + \kappa(1 - \sqrt{T_r})]^2$

$a_c = 0.45724\, R^2 T_c^2 / P$

$b = 0.07780\, RT_c / P$

$\kappa = 0.37464 + 1.54226\,\omega - 0.26993\,\omega^2$

ω = acentric factor

$$F(T_r) = \frac{-a}{bRT} - \frac{a_c}{bRT}[1 + \kappa(1 - \sqrt{T_r})]\,\kappa\sqrt{T_r}$$

Substitution of molar enthalpy of each phase into equation (5.7) yields:

$$\frac{\partial}{\partial t}\left\{\phi[\rho_g S_g(c_{pg}T + h_g^{res}RT)] + \phi[\rho_w S_w c_{pw}T] + \phi[\rho_H S_H h_H] + (1-\phi)[\rho_r c_{pr}T]\right\}$$
$$= \nabla\cdot\left(K_h\nabla T\right) - \nabla\cdot\left[\rho_g v_g(c_{pg}T + h_g^{res}RT) + \rho_w v_w c_{pw}T\right] + \frac{(Q_E - Q_{dis} + Q_{fus})}{V_b} \qquad 5.13$$

Recalling the following properties:

$$\nabla\cdot(\rho\upsilon c_p T) = \rho\upsilon\cdot\nabla(c_p T) + c_p T\cdot\nabla(\rho\upsilon) \qquad 5.14$$

$$\nabla\cdot(c_p T) = c_p\nabla T + T\nabla c_p = c_p\nabla T + T\left(\frac{\partial c_p}{\partial T}\right)\nabla T = \left(c_p + T\frac{\partial c_p}{\partial T}\right)\nabla T \qquad 5.15$$

and the mass balance of mobile phase "*l*" can be expressed as:

$$\nabla\cdot(\rho_l\upsilon_l) = \frac{Q_l}{V_b} - \frac{\partial}{\partial t}(\phi\rho_l S_l) \qquad 5.16$$

Substitution of equation (5.14), (5.15), and (5.16) into equation (5.13) yields:

$$-\rho_g v_g\left(c_{pg} + T\frac{\partial c_{pg}}{\partial T}\right)\nabla T - \rho_g v_g\nabla\cdot\left(h_g^{res}RT\right) - \rho_w v_w\left(c_{pw} + T\frac{\partial c_{pw}}{\partial T}\right)\nabla T$$
$$+ \frac{(Q_E - Q_{dis} + Q_{ice}^{fus})}{V_b} - \left(\frac{Q_g c_{pg}T}{V_b} + \frac{Q_w c_{pw}T}{V_b} + \frac{Q_g h_g^{res}RT}{V_b}\right) + \nabla\cdot\left(K_h\nabla T\right)$$
$$= \phi\rho_g S_g\left(c_{pg} + T\frac{\partial c_{pg}}{\partial T}\right)\frac{\partial T}{\partial t} + \phi\rho_w S_w\left(c_{pw} + T\frac{\partial c_{pw}}{\partial T}\right)\frac{\partial T}{\partial t} + (1-\phi)\rho_r c_{pr}\frac{\partial T}{\partial t}$$
$$+ (1-\phi)\rho_r T\left(\frac{\partial c_{pr}}{\partial T}\right)\frac{\partial T}{\partial t} + \frac{\partial(\phi\rho_H S_H h_H)}{\partial t} - h_g^{res}RT\frac{\partial(\phi\rho_g S_g)}{\partial t}$$
$$+ \rho_r c_{pr}T\frac{\partial(1-\phi)}{\partial P_g}\left(\frac{\partial P_g}{\partial t}\right) \qquad 5.17$$

Equation (5.1), (5.2), and (5.17) constitute a system of partial differential equations with ten unknowns which are P_g, P_a, S_g, S_a, S_H, x_m, x_w, y_m, y_w, and T. The primary variables are defined as the unknowns that are directly solved from the

discretized mass and energy balance equations (finite difference approximation) and the remaining unknowns are determined from auxiliary equations such as equations (5.3) and (5.5). Typically, primary variables will be selected from the natural variables such as pressure, temperature, phase saturation, and concentrations (mole fractions). They will be selected according to the phases appeared in each grid block. The sets of primary variables for each phase appearance case are summarized in Table 5-1.

Table 5-1: Sets of primary variables for each phase appearance case

Case	Phases	Primary Variables
1	H+A	T, P_a, S_H
2	G+A	T, P_g, S_a
3	H+A+G	T, S_a, S_g

For two-phase case, one phase pressure and temperature are used as the independent variables. They are solved simultaneously from the discretized governing equations. Only one phase saturation needs to be solved. Mole fractions of each component are not considered unknowns because they can be determined from equations (5.3) and (5.5).

For the three-phase case, free gas phase pressure and temperature are not both independent variables but they can be calculated as a function of the other using the equilibrium *P-T* correlation. In this work, the temperature was selected as the primary variable and P_G is calculated from the equilibrium correlation. The aqueous phase pressure is then calculated using capillary pressure relationship. For this case, aqueous

and free gas phase saturations are selected as primary unknowns and hydrate phase saturation is calculated from $S_H+S_g+S_a = 1$.

During the simulation, the disappearance of a phase can be simply identified by tracking its saturation value. If a saturation of any phase become less than or equal to zero, that phase disappears. The identification of phase appearance is more complicated and is determined using the location of gridblock condition which reflect to the *P*-*T* diagram of hydrate phase equilibrium. In the phase appearance identification, during two consecutive iterations, the hydrate phase stabilization boundary in the *P*-*T* diagram cannot be directly passed. An example of the protocol followed for phase appearance determination is discussed below.

Let us assume that hydrate and aqueous phases (*H*+*A*) are present in a previous iteration such as point "*A*" in Figure 5-2. The gas phase pressure at current iteration level is compared with the equilibrium pressure at the block temperature. Three possibilities may result from the comparison:

a) If $P_G > P_e$, such as point "*B*" in the figure, there should not be appearance of any new phase. Thus, the primary variables for this case are not changed.

b) If $P_G = P_e$, such as point "*C*" in the figure, the three phases (hydrate, aqueous, and free gas) should coexist at this condition. Therefore, a free gas phase should appear. Then the primary variables are switched to T, S_a, and S_g.

c) If $P_G < P_e$, such as point "*D*" in the figure, there should be only gas and aqueous phases. However, hydrate phase cannot immediately disappear in one iteration. Thus, the phases presented in this block at current iteration level should be

hydrate, free gas, and aqueous phases (H+G+A). Then, the primary variables are switched to T, S_a, and S_g.

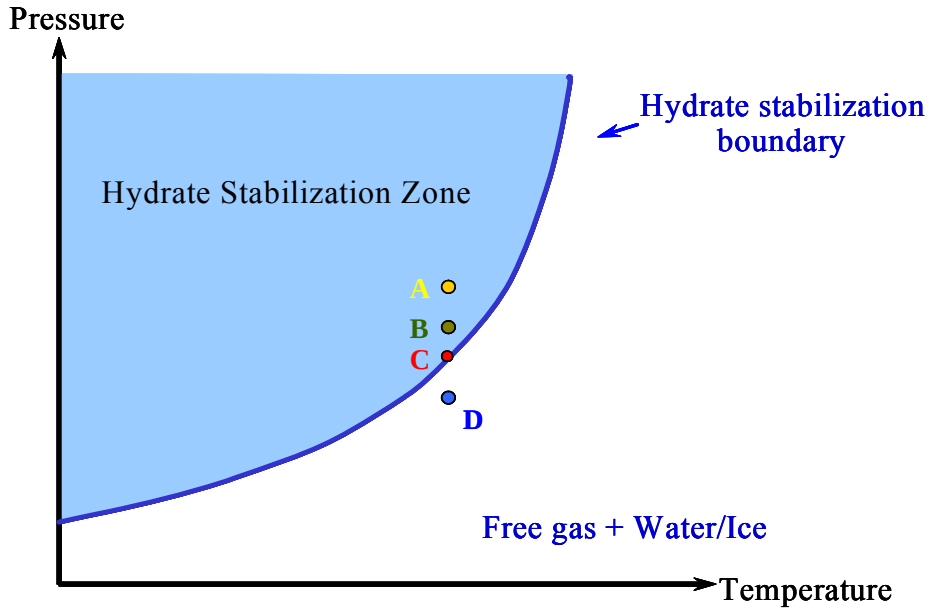

Figure 5-2: The possible calculated conditions at a new iteration level

In gas-hydrate systems, formation permeability decreases as hydrate saturation increases due to the decrease of the pore spaces. The capillary pressure between free-gas and aqueous phase in the formation also change when the saturations of aqueous and hydrate phases change. Additionally, the change of aqueous and hydrate saturations also change the heat conductivity of the system because they have different conductivity values. All of these factors are required to be taken into account for solving the problem and they will be discussed in the next section.

.

5.2 Absolute and Relative Permeability, Capillary Pressure, and Heat conductivity

5.2.1 Absolute Permeability

In this study, solid phase (hydrate and ice) in porous medium was considered as immobile phase and only aqueous and free gas phases can flow in porous medium. Thus, the presence of solid phase changes porosity and absolute permeability of porous rock. In the case that the data of rock permeability at various hydrate and ice saturations are not available, based on "tube-in-series" model of pore space, the change of rock permeability can be calculated from the following correlation[24, 25]:

$$\frac{k}{k_0} = \left(\frac{\phi - \phi_c}{\phi_0 - \phi_c} \right)^n \qquad 5.18$$

where ϕ_c = critical permeability

ϕ_0 = rock porosity (ice- and hydrate-free porosity)

k_0 = permeability at ϕ_0

n = correlation parameter

ϕ = rock porosity (with ice or hydrate phase in the pore space)

k = the permeability at ϕ

According to the experimental data, the value of parameter "n" can be as high as 10[11]. The values of $\frac{k}{k_0}$ at various hydrate saturations (for the case k_0 = 44 md, ϕ_0 = 0.3, ϕ_c = 0.07, and n = 3) calculated from equation (5.18) are shown in Figure 5-3.

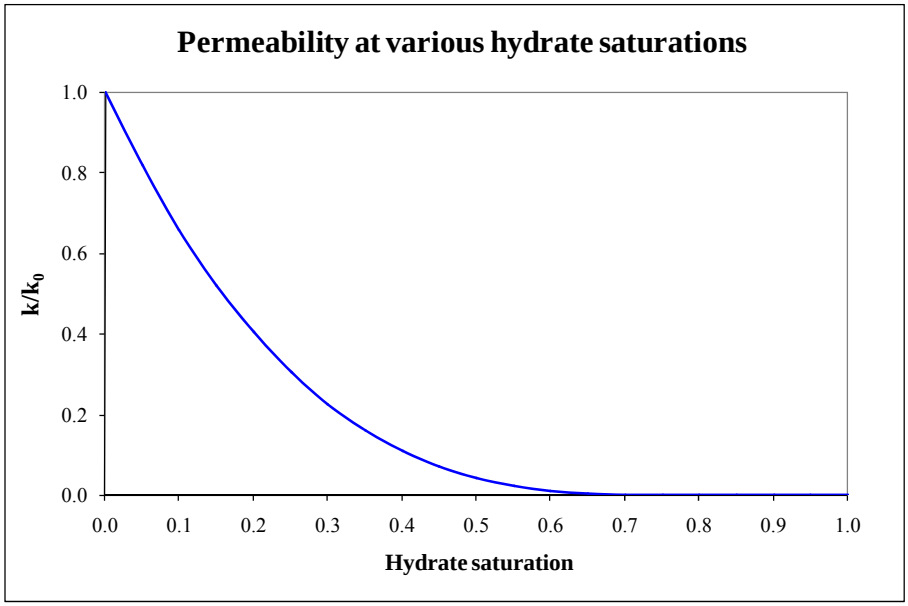

Figure 5-3: Permeability at various hydrate saturations

5.2.2 Relative Permeability

For relative permeability calculation purposes, the immobile solid phases (hydrate and ice phases) were treated as parts of porous rock, and the normalized aqueous and free gas saturations were used in relative permeability calculation. The normalized aqueous and free gas saturations can be calculated from the following equations:

$$S_a^* = \frac{S_a}{S_a + S_g} \qquad 5.19$$

$$S_g^* = \frac{S_g}{S_a + S_g} \qquad 5.20$$

where S_a^* = normalized aqueous phase saturation

S_g^* = normalized free gas phase saturation

S_a = aqueous phase saturation

S_g = free gas phase saturation

The calculated normalized water and free gas saturations are then used to determine relative permeability data to each phase from relative permeability data using linear interpolation technique. Note that the relative permeability data can be either provided to the simulator by users or generated from the default correlations of the simulator. Equation (5.21) shows the default relative permeability correlations of the simulator developed in this work.

$$k_{ra} = \left[\frac{S_a^* - S_{ira}}{1 - S_{ira}}\right]^{n_a}$$
$$k_{rg} = \left[\frac{S_g^* - S_{irg}}{1 - S_{ira}}\right]^{n_g} \qquad 5.21$$

Here n_a and n_g are the exponential parameters for aqueous and free-gas phases, respectively.

5.2.3 Capillary Pressure

The change of the capillary pressure between aqueous and free-gas phases due to hydrate saturation needs to be incoporated in the model. Moridis et al.[10] proposed a variant of Brooks-Corey function to estimate the capillary pressure for hydrate-water systems in Class 1 of hydrate deposit as the following equation:

$$P_{cap}(S_H, S_{aA}) = H(S_H) \cdot F \cdot P_e \cdot (S_{aA})^c \qquad 5.22$$

where P_e = gas entry pressure

c = a negative exponent ($|c| < 1$)

$S_{aA} = (S_A - S_{irA})/(1 - S_{irA})$

S_{irA} = irreducible water saturation

S_A = water saturation

F = erf [60 (1 - S_{aA})]

$H(S_H) = 1 + wB_x(a,b,S_S)$

S_H = hydrate saturation

w = a constant which can be estimated from laboratory data

$B_x(a,b,S_S)$ = the incomplete beta function

a and b = shape parameters

S_s = solid (hydrate and/or ice) saturation

The function F is introduced into the equation in order to prevent the discontinuity in the derivative which may cause the unstable of the numerical solution[10].

The capillary pressure at various hydrate saturations (S_{irA} = 0.25, S_{irG} = 0.02, w = 9.28, a = 2.1, b = 2.2, c = -0.65, and P_{GE} = 1.55x10^4 Pa) calculated from equation (5.22) is shown in Figure 5-4:

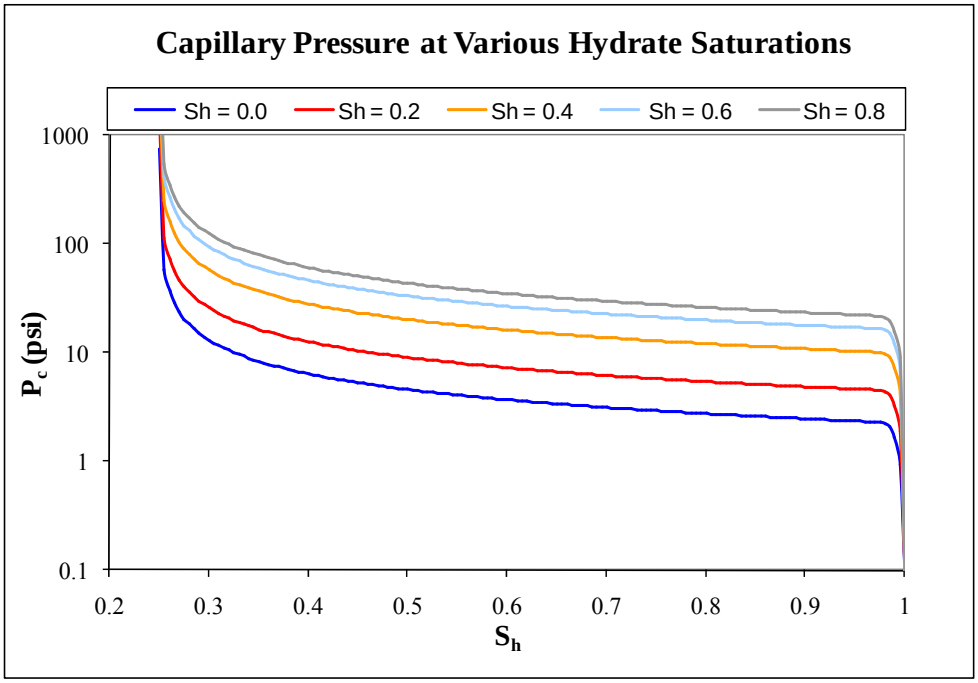

Figure 5-4: Capillary pressure at various hydrate saturations

5.2.4 Heat Conductivity

The appearance of hydrate phase can change the heat conductivity property of porous medium because rock, hydrate, aqueous and free gas have different conductivity properties. It has been recently studied [25] and found that the commonly used linear model based on the saturation-weighted contributions of phases and of the solid matrix is not adequate[11]. According to the study [25], a more appropriate estimate of the composite thermal conductivity of the porous media can be calculated from the extension of the Somerton et al. model[27] which is extensively used in geothermal studies:

$$\theta = \theta_{dry} + (S_a^{0.5} + S_H^{0.5})(\theta_{wet} - \theta_{dry}) + \phi S_I \theta_I \qquad 5.23$$

where θ_{dry} = dry thermal conductivity

θ_{wet} = wet thermal conductivity

θ_I = thermal conductivity of ice

S_a, S_H, S_I = saturations of aqueous, hydrate, and ice phases, respectively

5.3 Fluid Property Calculation

The following correlations are used to calculate density and viscosity of aqueous and free-gas phases in this study.

5.3.1 Fluid Density

In this study, a linear inerpolation technique is used to calculate the aqueous phase density at temperature T and 1 atm from the density data of water. Then the compressibility of water is used to calculate the aqueous phase density at temperature T and pressure p. Note that the effect of the amount of methane dissolved in aqueous phase on aqueous phase density is assumed to be negligible.

$$\rho_a(T, p) = \rho_a(T, 1atm) \cdot \left[1 + c_w(p - p_{sc})\right] \qquad 5.24$$

Parameter c_w is the compressibility of aqueous phase and p_{sc} is the standard pressure (14.7 psia).

The density of free-gas phase can be calculated from the following real gas law:

$$\rho_g(T,p) = (p \cdot MW)/(z \cdot R \cdot T) \qquad 5.25$$

Parameter *z* is the compressibility factor of free-gas phase and the Peng-Robinson Equation of State is used for calculating the compressibility factor of free-gas phase in this study.

5.3.2 Fluid Viscosity

In this study, the linear interpolation technique is used to calculate the aqueous phase viscosity at temperature *T* from the viscosity data of water. It is assumed that the effect of pressure on aqueous phase viscosity is negligible.

The Lee-Gonzalez-Eakin correlation[28] is used to determine the free-gas phase viscosity in this work:

$$\mu_g = 1x10^{-4} k_v \, EXP\left(x_v \left(\frac{\rho_g}{62.4} \right)^{y_v} \right) \qquad 5.26$$

where $k_v = \dfrac{\left[9.4 + 0.02\,MW_g\right] T^{1.5}}{209 + 19MW_g + T}$

$y_v = 2.4 - 0.2x_v$

$x_v = 3.5 + \dfrac{986}{T} + 0.01MW_g$

The units of *T*, ρ_g, and μ_g in this correlation are *R*, *lb/ft*^{3}, and *cP*, respectively.

5.4 Well Models for Reservoir Simulation

In this work, the Peaceman's wellbore model is used. The well-bore model is used to determine well flow rates and/or flowing bottomhole pressures. The detail of the wellbore model used in this work is discussed below. Note that the positive value of flow rate represents injection rate whereas the negative value of flow rate represents production rate.

5.4.1 Vertical Well

a) Water Flow Rate Specification

In this study, the explicit method was used for calculating water flow rate from multi-layer wells. A constant pressure gradient (i.e., the difference between well-block pressure and bottomhole pressure) is assumed for all completion layers in this method. Thus, water flow rate from layer *k* of a vertical well can be calculated from total water flow rate specification as shown in the following equation:

$$q_w^k = q_{w_{SP}} \cdot \frac{J_{wk}}{\sum_{k=1}^{nk} J_{wk}} \qquad 5.27$$

The variable J_{wk} is productivity index of aqueous phase for well block layer *k* (in the total *nk* well-block layers) which can be calculated from:

$$J_{wk} = \left[\frac{2\pi \bar{k} k_{rw} h}{\mu_w B_w \ln\left(\frac{r_w}{r_e} + S\right)} \right]_k \qquad 5.28$$

where r_w = wellbore radius

h = thickness of well block layer k

S = skin factor of well block layer k

k_{rw} = relative permeability to aqueous phase

B_w = formation volume factor of aqueous phase

μ_w = aqueous viscosity

Parameters $\bar{k}$ and r_e in equation (5.25) are calculated from the following equations:

$$\bar{k} = \sqrt{k_x \cdot k_y} \tag{5.29}$$

$$r_e = 0.28 \frac{\sqrt{(k_y/k_x)^{1/2}(\Delta x)^2 + (k_x/k_y)^{1/2}(\Delta y)^2}}{(k_y/k_x)^{1/4} + (k_x/k_y)^{1/4}} \tag{5.30}$$

The values of k_x and k_y are the rock permeability in x- and y-directions. After calculating water flow rate from each layer in vertical wells, gas flow rate from each layer is then calculated from the mobility ratio of gas to water phases as shown in the following expression:

$$q_g^k = q_w^k \left\{ \frac{k_{rg}/\mu_g B_g}{k_{rw}/\mu_w B_w} \right\}_k \tag{5.31}$$

where q_g^k = gas flow rate from layer k

q_w^k = water flow rate from layer k

k_{rg}, k_{rw} = relative permeability to free-gas and aqueous phases

B_g, B_w = formation volume factor of free-gas and aqueous phases

μ_g, μ_w = gas and aqueous viscosities

b) Gas Flow Rate Specification

Similar to the water flow rate specification case, gas flow rate from layer *k* of a vertical well can be calculated from total gas flow rate specification shown below:

$$q_g^k = q_{g_{SP}} \cdot \frac{J_{gk}}{\sum_{k=1}^{nk} J_{gk}} \qquad 5.32$$

Again, J_{gk} is the productivity index of gas phase of well block layer *k* which can be calculated from:

$$J_{gk} = \left[\frac{2\pi \bar{k} k_{rg} h}{\mu_g B_g \ln\left(\frac{r_w}{r_e} + S\right)} \right]_k \qquad 5.33$$

where r_w = well bore radius

h = thickness of well block layer *k*

S = skin factor of well block layer *k*

k_{rg} = the relative permeability to free gas phase

B_g = formation volume factor of gas phase

μ_g = gas viscosity

Again, $\bar{k}$ and r_e can be calculated from equations (5.26) and (5.27), respectively.

Similarly, water flow rate from each layer can be calculated from the mobility ratio of water to gas phases as shown in the following expression:

$$q_w^k = q_g^k \left\{ \frac{k_{rw} / \mu_w B_w}{k_{rg} / \mu_g B_g} \right\}_k \qquad 5.34$$

where q_w^k = water flow rate from layer k

q_g^k = gas flow rate from layer k

k_{rg}, k_{rw} = relative permeability to free-gas and aqueous phases

B_g, B_w = formation volume factor of free-gas and aqueous phases

μ_g , μ_w = gas and aqueous viscosities

c) Flowing Bottomhole Pressure Specification

In this work, it is assumed that the bottomhole pressures for all phases are the same. The Peaceman's wellbore model for this case can be written as:

$$q_f^k = \left(\frac{2\pi \bar{k}\, k_{rf}\, h\, (P_f - P_{wf,k})}{\mu_f B_f \ln\left(\frac{r_w}{r_e} + S \right)} \right)_k \qquad 5.35$$

where q_f^k = fluid flow rate from well block layer k

k_{rf} = relative permeability to fluid f

r_w = well bore radius

h = thickness of well block layer k

S = skin factor of well block layer k

B_f = formation volume factor of fluid

μ_f = fluid viscosity

$P_{wf,k}$ = sandface pressure of the well block layer k

Again $\bar{k}$ and r_e can be calculated from equations (5.26) and (5.27), respectively.

Since a constant pressure gradient for every layer for the flow rate specification cases is assumed, the value of sandface pressure of well block layer k can be calculated using pressure gradient of the well block under consideration:

$$P_{wf,k} = P_{wb,k} - \Delta P_{ref} \qquad 5.36$$

where $P_{wf,k}$ = sandface pressure of well block layer k

$P_{wb,k}$ = well block pressure (layer k)

ΔP_{ref} = pressure gradient of the reference layer

5.4.2 Horizontal Well

a) Water Flow rate is specified

Again, it is assumed the constant pressure gradient along the horizontal well (the difference between well-block pressure and bottomhole pressure). Thus, water flow rate from section l of a horizontal well can be calculated from total water flow rate specification as shown in the following equation:

$$q_w^l = q_{w_{SP}} \cdot \frac{J_{wl}}{\sum_{l=1}^{nl} J_{wl}} \qquad 5.37$$

The variable J_{wl} is productivity index of aqueous phase for well block l (in the total nl well-block sections) which can be calculated from:

$$J_{wl} = \left[\frac{2\pi \bar{k} k_{rw} L_l}{\mu_w B_w \ln\left(\frac{r_w}{r_e} + S \right)} \right]_l \qquad 5.38$$

where r_w = well bore radius

L_l = Length of well block section l

S = skin factor of well block section l

k_{rw} = relative permeability to aqueous phase

B_w = formation volume factor of aqueous phase

μ_w = aqueous viscosity

The values of $\bar{k}$ can be calculated from the following equation:

$$\bar{k} = \sqrt{k_m \cdot k_n} \qquad 5.39$$

Here k_m and k_n are the permeability values in m- and n-directions, respectively. Subscripts m and n represent the m-n plane which is perpendicular to the well direction. For example, m and n refer to y and z directions for horizontal wells placed along the x-direction. Similarly, the value of r_e is calculated from:

$$r_e = 0.28 \frac{\sqrt{(k_m/k_n)^{1/2}(\Delta n)^2 + (k_n/k_m)^{1/2}(\Delta m)^2}}{(k_m/k_n)^{1/4} + (k_n/k_m)^{1/4}} \qquad 5.40$$

Again, subscript *m* and *n* represent the *m*-*n* plane which is perpendicular to the well direction.

Similar to the vertical well case, and after calculating water flow rate of each section of a horizontal well, gas flow rate of well block section *l* can be then calculated from the mobility ratio of gas to water phases as indicated in the following equation:

$$q_g^l = q_w^l \left\{ \frac{k_{rg} / \mu_g B_g}{k_{rw} / \mu_w B_w} \right\}_l \qquad 5.41$$

where q_g^l = gas flow rate from section *l* of a horizontal well

q_w^l = water flow rate from section *l* of a horizontal well

k_{rg}, k_{rw} = relative permeability to free-gas and aqueous phases

B_g, B_w = formation volume factor of free-gas and aqueous phases

μ_g , μ_w = gas and aqueous viscosities

b) Gas Flow Rate Specification

Similar to the water flow rate specification case, gas flow rate from section *l* of a horizontal well can be calculated from total gas flow rate specification using the following equation:

$$q_g^l = q_{g_{SP}} \cdot \frac{J_{gl}}{\sum_{l=1}^{nl} J_{gl}} \qquad 5.42$$

Again, J_{gl} is the productivity index of gas phase of well block section *l* which can be calculated from:

$$J_{gl} = \left[\frac{2\pi \bar{k} k_{rg} L_l}{\mu_g B_g \ln\left(\frac{r_w}{r_e} + S\right)} \right]_l \qquad 5.43$$

where r_w = well bore radius

L_l = Length of well block section l

S = skin factor of well block section l

k_{rw} = relative permeability to aqueous phase

B_w = formation volume factor of aqueous phase

μ_w = aqueous viscosity

The values of $\bar{k}$ and r_e can be calculated using equations (5.36) and (5.37).

Similarly, and after calculating gas flow rate of each section of a horizontal well, water flow rate of well block section l can be then calculated from the mobility ratio of water to gas phases as indicated in the following equation:

$$q_w^l = q_g^l \left\{ \frac{k_{rw} / \mu_w B_w}{k_{rg} / \mu_g B_g} \right\}_l \qquad 5.44$$

where q_w^l = water flow rate from section l of a horizontal well

q_g^l = gas flow rate from section l of a horizontal well

k_{rg}, k_{rw} = relative permeability to free-gas and aqueous phases

B_g, B_w = formation volume factor of free-gas and aqueous phases

μ_g , μ_w = gas and aqueous viscosities

c) Flowing Bottomhole Pressure Specification

For horizontal well case, bottomhole pressures of every section of a horizontal well are equal to specified bottomhole pressure because there are no hydrostatic gradients for this case. Accordingly, the flow rate of fluid *f* from section *l* of a horizontal well can be calculated from:

$$q_f^l = \left(\frac{2\pi \bar{k}\, k_{rf}\, L_l\, (P_f - P_{wf,l})}{\mu_f B_f \ln\left(\frac{r_w}{r_e} + S\right)} \right)_l \qquad 5.45$$

where q_f^l = fluid flow rate from section *l* of a horizontal well

k_{rf} = relative permeability to fluid *f*

r_w = well bore radius

L_l = Length of well block section *l*

S = skin factor of well block section *l*

B_f = formation volume factor of fluid

μ_f = fluid viscosity

$P_{wf,k}$ = sandface pressure of the well block section *l*

Again $\bar{k}$ and r_e can be calculated from equations (5.36) and (5.37), respectively.

5.5 Material and Energy Balance Checks

5.5.1 Material Balance Check

In order to check the accuracy of the simulation results, a material balance check on each component must be performed. There are two types of checks.

a) Incremental Material Balance (IMB) for i^{th}-component

$$IMB_i = \left| \frac{\sum_{i=1}^{nx}\sum_{j=1}^{ny}\sum_{k=1}^{nz}\left(\frac{V_b}{5.615}\left(\phi y_i S_g \overline{\rho}_g + \phi x_i S_a \overline{\rho}_a + \phi c_i S_H \overline{\rho}_H\right)\right)_{i,j,k}^{n+1} + \sum_{i=1}^{nw} y_i q_g^{well(n+1)} \Delta t^{n+1} + \sum_{i=1}^{nw} x_i q_a^{well(n+1)} \Delta t^{n+1}}{\sum_{i=1}^{nx}\sum_{j=1}^{ny}\sum_{k=1}^{nz}\left(\frac{V_b}{5.615}\left(\phi y_i S_g \overline{\rho}_g + \phi x_i S_a \overline{\rho}_a + \phi c_i S_H \overline{\rho}_H\right)\right)_{i,j,k}^{n}} \right| \cong 1.0 \qquad 5.46$$

b) Cumulative Material Balance (CMB) for i^{th}-component

$$CMB_i = \left| \frac{\sum_{i=1}^{nx}\sum_{j=1}^{ny}\sum_{k=1}^{nz}\left(\frac{V_b}{5.615}\left(\phi y_i S_g \overline{\rho}_g + \phi x_i S_a \overline{\rho}_a + \phi c_i S_H \overline{\rho}_H\right)\right)_{i,j,k}^{n+1} + \sum_{l=0}^{n+1}\left(\sum_{i=1}^{nw} y_i q_g^{well(l)} \Delta t^{l} + \sum_{i=1}^{nw} x_i q_a^{well(l)} \Delta t^{l}\right)}{\sum_{i=1}^{nx}\sum_{j=1}^{ny}\sum_{k=1}^{nz}\left(\frac{V_b}{5.615}\left(\phi y_i S_g \overline{\rho}_g + \phi x_i S_a \overline{\rho}_a + \phi c_i S_H \overline{\rho}_H\right)\right)_{i,j,k}^{n=0}} \right| \cong 1.0 \qquad 5.47$$

5.5.2 Energy Balance Check

The correct temperature distribution should produce a good energy balance check. The finite difference approximation should be consistent with the energy conservation if the finite difference representation approximates the solution of the problem with an acceptable degree of accuracy. On an incremental basis, the energy balance can be expressed as the following equation:

$$Final\ Heat\ Content = Original\ Heat\ Content + Heat\ Added - Heat\ Loss \qquad 5.48$$

Each term in the above equation can be calculated from the following expressions:

$$Final\ Heat\ Content = \sum_{i=1}^{nx}\sum_{j=1}^{ny}\sum_{k=1}^{nz} V_b \left\{ \left[(1-\phi)\rho_r c_{pr} + \phi(\rho_g S_g c_{pg} + \rho_w S_w c_{pw}) \right]_{i,j,k}^{n+1} T_{i,j,k}^{n+1} + \left[\phi \rho_H S_H h_H(T) \right]_{i,j,k}^{n+1} \right\}$$

$$Original\ Heat\ Content = \sum_{i=1}^{nx}\sum_{j=1}^{ny}\sum_{k=1}^{nz} V_b \left\{ \left[(1-\phi)\rho_r c_{pr} + \phi(\rho_g S_g c_{pg} + \rho_w S_w c_{pw}) \right]_{i,j,k}^{n} T_{i,j,k}^{n} + \left[\phi \rho_H S_H h_H(T) \right]_{i,j,k}^{n} \right\}$$

$$Heat\ Loss = \sum_{i=1}^{nx}\sum_{j=1}^{ny}\sum_{k=1}^{nz} \left\{ \left[q_g^{well} \Delta t\, \rho_{gsc} c_{pg} + 5.615 q_w^{well} \Delta t\, \rho_{wsc} c_{pw}) \right]_{i,j,k}^{n+1} T_{i,j,k}^{n+1} + \left(q_g^{dis} \Delta t\, Q_{dis} \right)_{i,j,k}^{n+1} \right\}$$

$$Heat\ Added = \sum_{i=1}^{nx}\sum_{j=1}^{ny}\sum_{k=1}^{nz} \left[5.615 q_w^{inject} \Delta t\, \rho_{wsc} c_{pw}) T \right]_{i,j,k}^{injected\ conditions}$$

One may define the incremental balance as the following ratio:

$$IEB = \frac{Original\ Heat\ Content + Heat\ Added - Heat\ Loss}{Final\ Heat\ Content} \cong 1.0 \qquad 5.49$$

CHAPTER 6

RESERVOIR SIMULATION STUDY

The methane-hydrate reservoir simulator developed in this work must be validated before using it for further simulation application. Unfortunately, production data from actual methane-hydrate reservoirs in the literature are not yet available. However, results of some simulation studies from mathematical models developed in previous studies can be found in the literature[6,11]. Therefore, at this point in time, the validation of the developed simulator in this work can only be achieved by comparing the simulation results of this work with the results from previous studies. In this work, the simulation results from Burshears' and Moridis' works[6,11] are used for the validation purposes. In Moridis' work, the cylindrical-coordinate system was used whereas the rectangular-coordinate system is used in this work. The two reservoirs have the same volume. Gas is produced through a production well located at the center of the reservoir at a constant gas flow rate at 2.5 MMSCF/day. The production well is completed along the free-gas zone.

The class 1 methane hydrate reservoir structure discussed in Holder's work [5] was used in Moridis' study and it is also used in this work for the examination of production characteristics from class 1 gas hydrate deposit. From the literature review, most of the methane-hydrate reservoir simulation studies, the production characteristics for constant gas production rate scheme were examined. In this work, the study of gas production characteristics will focus on a constant bottomhole-pressure production scheme more

than a constant gas flow rate production scheme to gain a better insight for the activation of the production mechanisms inherent to this class of reservoirs.

The reservoir structure in Holder's work consists of two zones: hydrate zone in the upper part of the system and free gas zone in the lower part of the reservoir. The thicknesses of both zones are 50 feet.

Initially, methane hydrate and water saturations in the hydrate zone are 70 and 30 percents, respectively, whereas the average free gas and water saturations in the free gas zone are 70 and 30 percents, respectively. There is a well located at the center of the system and it is completed only in the free gas zone. The overall structure of the reservoir is shown in Figure 6-1.

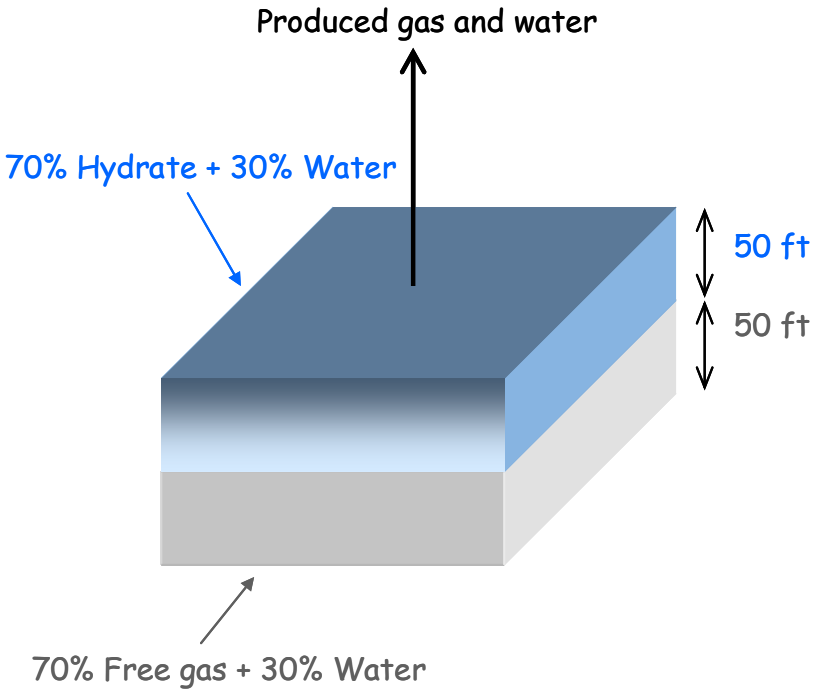

Figure 6-1: Gas-hydrate reservoir structure in this study

6.1 Reservoir Rock and Fluid Properties

a) Reservoir Rock Properties

In this work, the reservoir rock is assumed to be sandstone with uniform porosity and homogeneous and isotropic permeability distribution. The reservoir rock properties used in this model validation are summarized in Table 6-1. Note that the input data for the developed simulator must be in the oil-field unit, but since the SI unit was used in Moridis' work, the rock and fluid properties used in this validation are therefore shown in the SI unit as well.

Table 6-1: Reservoir rock properties used in this study[11]

Rock Properties	Value	
Rock porosity (homogeneous)	30 %	
Heat conductivity (wet)	1.7911 BTU/hr-ft-^{o}F	(3.1 W/m-K)
Heat conductivity (dry)	0.2889 BTU/hr-ft-^{o}F	(0.5 W/m-K)
Rock density (homogeneous)	162.31 lb/ft^{3}	(2,600 kg/m^{3})
Pore compressibility*	0.0 psi^{-1}	(0.0 Pa^{-1})
Rock permeability	1,000 mD	(1.0x10^{-12} m^{2})
Specific heat of rock*	0.22 BTU/lb-^{o}F	(0.92 kJ/kg-K)

* This value was not provided in Moridis' study

b) Methane-Hydrate Properties

In this work, it is assumed that the change of the density of methane-hydrate due to the change of temperature and pressure is negligible. The properties of methane-hydrate phase used in this work are summarized in Table 6-2.

Table 6-2: Hydrate Properties[11]

Hydrate Properties	Value	
Density*	57.43 lb/ft^3	(920 kg/m^3) [3]
Specific heat	0.5016 BTU/lb-^{o}F	(2.10 kJ/kg-K)
Heat conductivity	0.2600 BTU/hr-ft-^{o}F	(0.45 W/m-K)

* This value was not provided in Moridis' study

c) Aqueous phase properties

The change of the density of aqueous phase can occur when either pressure or temperature (or both) change. The densities of aqueous phase at various temperatures and 14.70 psia used in this work are shown in Table 6-3. The change of aqueous phase density due to the change of pressure can be calculated using the compressibility of aqueous phase. In this work, the compositional effect on aqueous phase density is neglected. Note that the compressibility of aqueous phase is assumed to be a constant within the pressure range of the study.

Table 6-3: Aqueous phase density at various temperatures[29]

Temperature (^{o}F)	Density (lb/ft^3)	Temperature (^{o}F)	Density (lb/ft^3)
32.0	62.42	57.2	62.39
33.8	62.42	59.0	62.38
35.6	62.42	60.8	62.37
37.4	62.43	62.6	62.36
39.2	62.43	64.4	62.35
41.0	62.43	66.2	62.33
42.8	62.43	68.0	62.32
44.6	62.43	69.8	62.31
46.4	62.42	71.6	62.29
48.2	62.42	73.4	62.28
50.0	62.41	75.2	62.26
51.8	62.41	77.0	62.25
53.6	62.40	78.8	62.23
55.4	62.39	80.6	62.22

In this work, it is assumed that the change of aqueous phase viscosity due to the change of pressure is negligible. However, the change of aqueous phase viscosity due to the temperature change is taken into account. Table 6-4 shows the values of aqueous phase viscosity used in this study at various temperatures. Again, the compositional effect of aqueous phase on its viscosity is neglected.

Table 6-4: Aqueous phase viscosity at various temperatures[29]

Temperature (^{o}F)	Viscosity (cP)
32.0	1.794
40.0	1.546
50.0	1.310
60.0	1.129
70.0	0.982
80.0	0.862
90.0	0.764
100.0	0.682

d) Rock and Fluid Interactions Properties

In this study, the change of rock permeability due to solid saturation is calculated using equation (5.17). Equation (5.20) is used for calculating capillary pressure between aqueous and free gas phases. Table 6-5 summarizes all the parameter values of these two equations used in this study. Note that the information about the equation used for calculating the change of formation permeability due to the change of hydrate saturation was not provided in the Moridis' study. In this study, equation (5.18) was used and the values of the parameters in the equation were selected in such a way that the permeability of the hydrate zone (S_H = 0.70) is closed to zero in order to prevent the drainage of aqueous phase in hydrate zone to the lower free-gas zone. The plot of this equation was displayed earlier in Figure 5-3.

Table 6-5: Parameters used in permeability and capillary pressure calculations[11]

Properties	Parameters	Value
Permeability*	n	3.00
	ϕ_o	0.30
	ϕ_c	0.07
	k_0	1000 mD
Capillary Pressure	S_{wirr}	0.25
	p_e	2.248 psia (15500 Pa)
	c	-0.65
	a	2.10
	b	2.20

* This information was not provided in Moridis' study

Table 6-6 shows the data of the relative permeabilities to aqueous and free-gas phases used in this validation.

Table 6-6: Relative permeability data used in this validation[11]

S_A	k_{rA}	k_{rg}	S_A	k_{rA}	k_{rg}
0.00	0.0000	1.0000	0.60	0.2160	0.0640
0.10	0.0000	0.7290	0.62	0.2383	0.0549
0.15	0.0000	0.6141	0.64	0.2621	0.0467
0.20	0.0000	0.5120	0.66	0.2875	0.0393
0.25	0.0000	0.4219	0.68	0.3144	0.0328
0.26	0.0176	0.4052	0.70	0.3430	0.0270
0.28	0.0220	0.3732	0.72	0.3732	0.0220
0.30	0.0270	0.3430	0.74	0.4052	0.0176
0.32	0.0328	0.3144	0.76	0.4390	0.0138
0.34	0.0393	0.2875	0.78	0.4746	0.0106
0.36	0.0467	0.2621	0.80	0.5120	0.0080
0.38	0.0549	0.2383	0.82	0.5514	0.0058
0.40	0.0640	0.2160	0.84	0.5927	0.0041
0.42	0.0741	0.1951	0.86	0.6361	0.0027
0.44	0.0852	0.1756	0.88	0.6815	0.0017
0.46	0.0973	0.1575	0.90	0.7290	0.0010
0.48	0.1106	0.1406	0.92	0.7787	0.0005
0.50	0.1250	0.1250	0.94	0.8306	0.0002
0.52	0.1406	0.1106	0.96	0.8847	0.0001
0.54	0.1575	0.0973	0.98	0.9412	0.0000
0.56	0.1756	0.0852	1.00	1.0000	0.0000
0.58	0.1951	0.0741			

6.2 Grid Structure of the Reservoir

A three-dimensional, rectangular, body-centered grid system is used in the discretization of this study. The additional 45-feet thick intervals of impermeable rock are added to the top and the bottom of the reservoir. No fluid flow takes place in these two impermeable zones but heat transfer across the upper and lower boundaries is allowed. It is further assumed that this thickness is sufficient to allow accurate heat exchange calculation with hydrate deposit over a 30-year long production period [11]. Figure 6-2 shows the grid structure of the reservoir in this study.

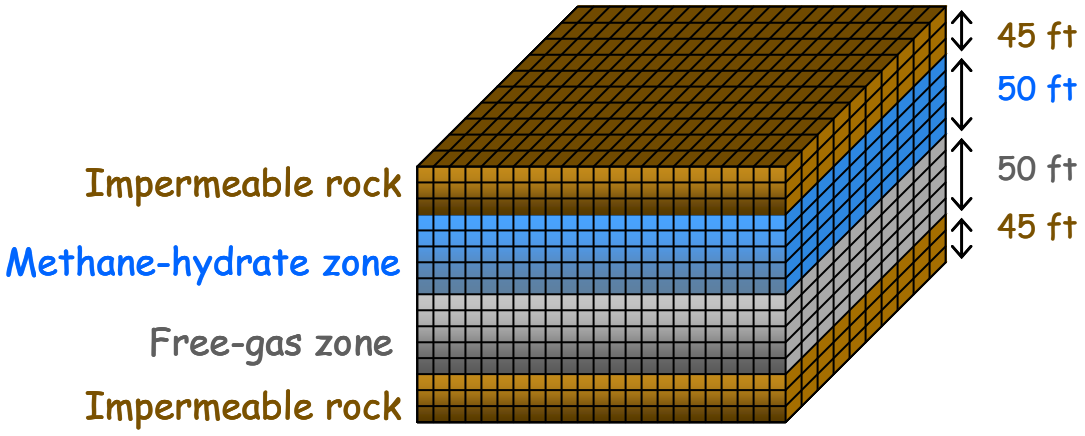

Figure 6-2: Grid structure of the reservoir in this work

In this study, the total number of layers of free-gas and hydrate zones is 10 layers (5 layers for each zone). Each layer is 10 feet thick. There are three layers for each impermeable zone. Therefore, the grid structure is totally consisted of 16 layers in the z-direction. The layer thickness and the rock properties for each zone are summarized in Table 6-7. The cartesian coordinate system is used in this work whereas the cylindrical

coordinate was used in Moridis' work. Thus, the grid-block dimensions used in this work are not the same as the block dimensions used in the Moridis' work. Note that the block dimensions are selected as small as possible with due cognizance is given to the computational work invloved.

Table 6-7: Layer thickness and rock properties

Layers No.	Layer Thickness (ft)	Porosity	Permeability (mD)	Remark
1	20	0.0	0.00	**Const P and T**
2	20	0.0	0.00	**Impermeable rock zone**
3	15	0.0	0.00	
4	10	0.0	0.00	
5	10	0.3	1000	**Methane-hydrate zone** ≈ 70% Hydrate saturation ≈ 30% Water saturation
6	10	0.3	1000	
7	10	0.3	1000	
8	10	0.3	1000	
9	10	0.3	1000	
10	10	0.3	1000	**Free-gas zone** ≈ 70% Free-gas saturation ≈ 30% Water saturation
11	10	0.3	1000	
12	10	0.3	1000	
13	10	0.3	1000	
14	10	0.3	1000	
15	10	0.0	0.00	**Impermeable rock zone**
16	15	0.0	0.00	
17	20	0.0	0.00	
18	20	0.0	0.00	**Const P and T**

6.3 Reservoir Initialization

Initially, the system is in hydraulic, thermal, and thermodynamic equilibrium. The initialization for the reservoir simulation of Class 1 hydrate deposits is a challenging task. It is found that initializing the entire system at once is not an easy task to obtain the

initial conditions close to the desired initial conditions. This is because the changes of pressure and temperature in the free-gas zone will affect the conditions in hydrate zone. For example, if the heat flux to the dissociation front from the lower and upper layers are not equal, it causes the change of temperature at the dissociation front. Consequently, the hydrate association or dissociation occurs resulting in the change of pressure and temperature of the entire system. Accordingly, it will be easier to initialize the entire system when the change of the conditions of both zones is minimal. In order to achieve this objective, the procedure discussed below is implemented.

In the initialization process, the reservoir is divided into two sections, one corresponding to the hydrate zone (upper section) and the other one corresponding to the two-phase zone (lower section). The bottom layer of the upper (hydrate) zone and the top layer of the lower (free-gas) zone are treated as the boundaries representing the hydrate dissociation front where free gas phase, aqueous phase, and methane hydrate coexist in equilibrium.

Starting with the lower section, initial pressure, temperature, and saturation of each phase are determined by running the simulator (without production or injection) to achieve an equilibrium condition. Note that pressure, temperature, and phase saturations of the first layer (hydrate dissociation front) of this zone do not change during this step. The initial values used for this initialization are shown in Table 6-8. The temperature gradient used for this zone is 0.0170 ^{o}F/ft and the temperature of the dissociation front is 56.30 ^{o}F [11]. The temperature gradient of the system was not provided in this Moridis' work. This value comes from a different work of Alp and Moridis [30] when a similar system was studied.

Table 6-8: Initial values for the initialization of the lower section

Layer no.	P_g (psia)	S_a	S_H	T (^oF)	Remarks
9	1550.00	0.2950	0.7000	56.300	Dissociation front (G+H+A)
10	1550.00	0.3000	0.0000	56.465	Free gas zone (G+A)
11	1550.00	0.3000	0.0000	56.629	
12	1550.00	0.3000	0.0000	56.794	
13	1550.00	0.3000	0.0000	56.959	
14	1550.00	0.3000	0.0000	57.123	
15	0.00	0.0000	0.0000	57.288	Impermeable layer
16	0.00	0.0000	0.0000	57.452	
17	0.00	0.0000	0.0000	57.699	
18	0.00	0.0000	0.0000	58.029	Inactive layer with constant T

Note that the program automatically sets the gas pressure of any block where three phases (gas, aqueous, and methane hydrate) are present to be equal to the dissociation pressure corresponding to the block temperature. Therefore, the gas pressure of the dissociation front layer is automatically set to be 1548.06 psia corresponding to the temperature (56.30 ^oF) of this layer even though the pressure of this layer from the input file was 1,550 psia. In this initialization, the small gas saturation (0.005) was introduced in the dissociation front layer so that three phases appear in the dissociation front layer. The results from the initialization of this section are shown in Table 6-9.

Table 6-9: Results from the initialization of the lower section

Layer no.	P_g (psia)	S_a	S_H	T (^oF)	Remarks
9	1548.06	0.2950	0.7000	56.300	Dissociation front (G+H+A)
10	1537.05	0.2591	0.0000	56.344	Free gas zone (G+A)
11	1537.44	0.2650	0.0000	56.415	
12	1537.83	0.2747	0.0000	56.486	
13	1538.22	0.2926	0.0000	56.555	
14	1538.60	0.3334	0.0000	56.621	
15	0.00	0.0000	0.0000	56.726	Impermeable layer
16	0.00	0.0000	0.0000	57.051	
17	0.00	0.0000	0.0000	57.507	
18	0.00	0.0000	0.0000	58.029	Inactive layer with constant T

Results in Table 6-9 show that aqueous phase saturation in the lower part of the section is higher due to the gravitational effects.

The next step is to initialize the upper section. The initial values for the initialization of this section are shown in Table 6-10. The results from the initialization of this section are shown in Table 6-11. Note that the program reads gas phase pressure and aqueous phase saturation from the input data and then uses the capillary pressure correlation to calculate aqueous phase pressure. In the case that there is no gas phase in a grid block, the gas phase pressures of all layers in the upper section are set to be a little bit higher (1,550 psia) than the gas pressure at the dissociation front layer (1,548.06 psia) to ensure that the conditions of all the layers above the dissociation front are inside the hydrate stabilization boundary in the gas-hydrate equilibrium diagram.

Table 6-10: Initial values for the initialization of the upper section

Layer no.	P_g (psia)	S_a	S_H	T (^oF)	Remarks
1	0.00	0.0000	0.0000	54.571	Inactive layer with constant T
2	0.00	0.0000	0.0000	54.901	Impermeable layer
3	0.00	0.0000	0.0000	55.230	
4	0.00	0.0000	0.0000	55.477	
5	1550.00	0.3000	0.7000	55.641	Hydrate zone (H+A)
6	1550.00	0.3000	0.7000	55.806	
7	1550.00	0.3000	0.7000	55.971	
8	1550.00	0.3000	0.7000	56.135	
9	1548.06	0.2950	0.7000	56.300	Dissociation front (G+H+A)

Table 6-11: Results from the initialization of the upper section

Layer no.	P_g (psia)	S_a	S_H	T (^oF)	Remarks
1	0.00	0.0000	0.0000	54.571	Inactive layer with constant T
2	0.00	0.0000	0.0000	54.909	Impermeable layer
3	0.00	0.0000	0.0000	55.275	
4	0.00	0.0000	0.0000	55.438	
5	1530.66	0.3000	0.7000	55.584	Hydrate zone (H+A)
6	1535.01	0.3000	0.7000	55.812	
7	1539.36	0.3000	0.7000	55.970	
8	1543.71	0.3000	0.7000	56.136	
9	1548.06	0.2950	0.7000	56.300	Dissociation front (G+H+A)

In the third step, the two sections are combined together and still keep the pressure, temperature, and saturations of the dissociation front constant. Then the model is run until achieving a new equilibrium condition. Table 6-12 shows the initial values for this step. The next step is to set layer no.9 as a regular layer (*T*, *P* and *S* can change) and run the simulation to achieve a new equilibrium condition. The results of this step are shown in Table 6-13.

Table 6-12: Initial values for the initialization of the entire reservoir

Layer no.	P_g (psia)	S_a	S_H	T (^oF)	Remarks
1	0.00	0.0000	0.0000	54.571	Inactive layer with constant T
2	0.00	0.0000	0.0000	54.909	Impermeable layer
3	0.00	0.0000	0.0000	55.275	
4	0.00	0.0000	0.0000	55.438	
5	1530.66	0.3000	0.7000	55.584	Hydrate zone (H+A)
6	1535.01	0.3000	0.7000	55.812	
7	1539.36	0.3000	0.7000	55.970	
8	1543.71	0.3000	0.7000	56.136	
9	1548.06	0.2950	0.7000	56.300	Dissociation front (G+H+A)
10	1537.05	0.2591	0.0000	56.344	Free gas zone (G+A)
11	1537.44	0.2650	0.0000	56.415	
12	1537.83	0.2747	0.0000	56.486	
13	1538.22	0.2926	0.0000	56.555	
14	1538.60	0.3334	0.0000	56.621	
15	0.00	0.0000	0.0000	56.726	Impermeable layer
16	0.00	0.0000	0.0000	57.051	
17	0.00	0.0000	0.0000	57.507	
18	0.00	0.0000	0.0000	58.029	Inactive layer with constant T

Table 6-13: Results from the initialization of the entire reservoir

Layer no.	P_g (psia)	S_a	S_H	T (^oF)	Remarks
1	0.00	0.0000	0.0000	54.571	Inactive layer with constant T
2	0.00	0.0000	0.0000	55.040	Impermeable layer
3	0.00	0.0000	0.0000	55.532	
4	0.00	0.0000	0.0000	55.971	
5	1534.75	0.3000	0.7000	56.060	Hydrate zone (H+A)
6	1539.10	0.3000	0.7000	56.117	
7	1543.45	0.3000	0.7000	56.183	
8	1547.81	0.3000	0.7000	56.257	
9	1552.16	0.2949	0.6965	56.341	Dissociation front (G+H+A)
10	1538.87	0.2619	0.0000	56.594	Free gas zone (G+A)
11	1539.26	0.2651	0.0000	56.653	
12	1539.65	0.2747	0.0000	56.609	
13	1540.03	0.2926	0.0000	56.638	
14	1540.42	0.3334	0.0000	56.614	
15	0.00	0.0000	0.0000	56.734	Impermeable layer
16	0.00	0.0000	0.0000	57.054	
17	0.00	0.0000	0.0000	57.508	
18	0.00	0.0000	0.0000	58.029	Inactive layer with constant T

The result shows a slight decrease of hydrate saturation at the dissociation front due to the dissociation at the front.

It was found that the hydrate saturations at the dissociation front of the reservoir can be slightly changed to the desired values (0.70) without disturbing the obtained initial condition because this change does not significantly affect the heat transfer properties of this layer. Accordingly, the computed initial pressure and temperature of the entire system can still be used. Therefore, the saturations of aqueous and hydrate phases in the upper section are changed to the desired values. Table 6-14 shows the initial conditions of the reservoir used in this study.

Table 6-14: Initial conditions of the reservoir used in this study

Layer no.	P_g (psia)	S_a	S_H	T (^oF)	Remarks
1	0.00	0.0000	0.0000	54.571	Inactive layer with constant T
2	0.00	0.0000	0.0000	55.040	Impermeable layer
3	0.00	0.0000	0.0000	55.532	
4	0.00	0.0000	0.0000	55.971	
5	1534.75	0.3000	0.7000	56.060	Hydrate zone (H+A)
6	1539.10	0.3000	0.7000	56.117	
7	1543.45	0.3000	0.7000	56.183	
8	1547.81	0.3000	0.7000	56.257	
9	1552.16	0.2950	0.7000	56.341	Dissociation front (G+H+A)
10	1538.87	0.2619	0.0000	56.594	Free gas zone (G+A)
11	1539.26	0.2651	0.0000	56.653	
12	1539.65	0.2747	0.0000	56.609	
13	1540.03	0.2926	0.0000	56.638	
14	1540.42	0.3334	0.0000	56.614	
15	0.00	0.0000	0.0000	56.734	Impermeable layer
16	0.00	0.0000	0.0000	57.054	
17	0.00	0.0000	0.0000	57.508	
18	0.00	0.0000	0.0000	58.029	Inactive layer with constant T

An uniform block dimension is used in this work. The effects of block dimensions (Δx and Δy) on simulation results are shown in Figure 6-3. Table 6-15 shows the average percent deviation of the results against the results from the smallest grid block dimensions (Δx and Δy =50 ft) and the computational time it can reduced.

Table 6-15: The effects of grid block dimensions on the results and computational time

Dimensions (feet)	Differences (%)	Reduction Time (%)
50*	0.00	0.00
75	2.92	12.00
100	6.99	26.00
150	13.07	34.00

* reference case

The grid block dimensions in x and y directions (Δx and Δy) used in this study is selected as 100 feet as the model could execute about 26 percent faster while maintaining an average derviation of 7 percent with respect to the reference case of block dimensions of 50 feet.

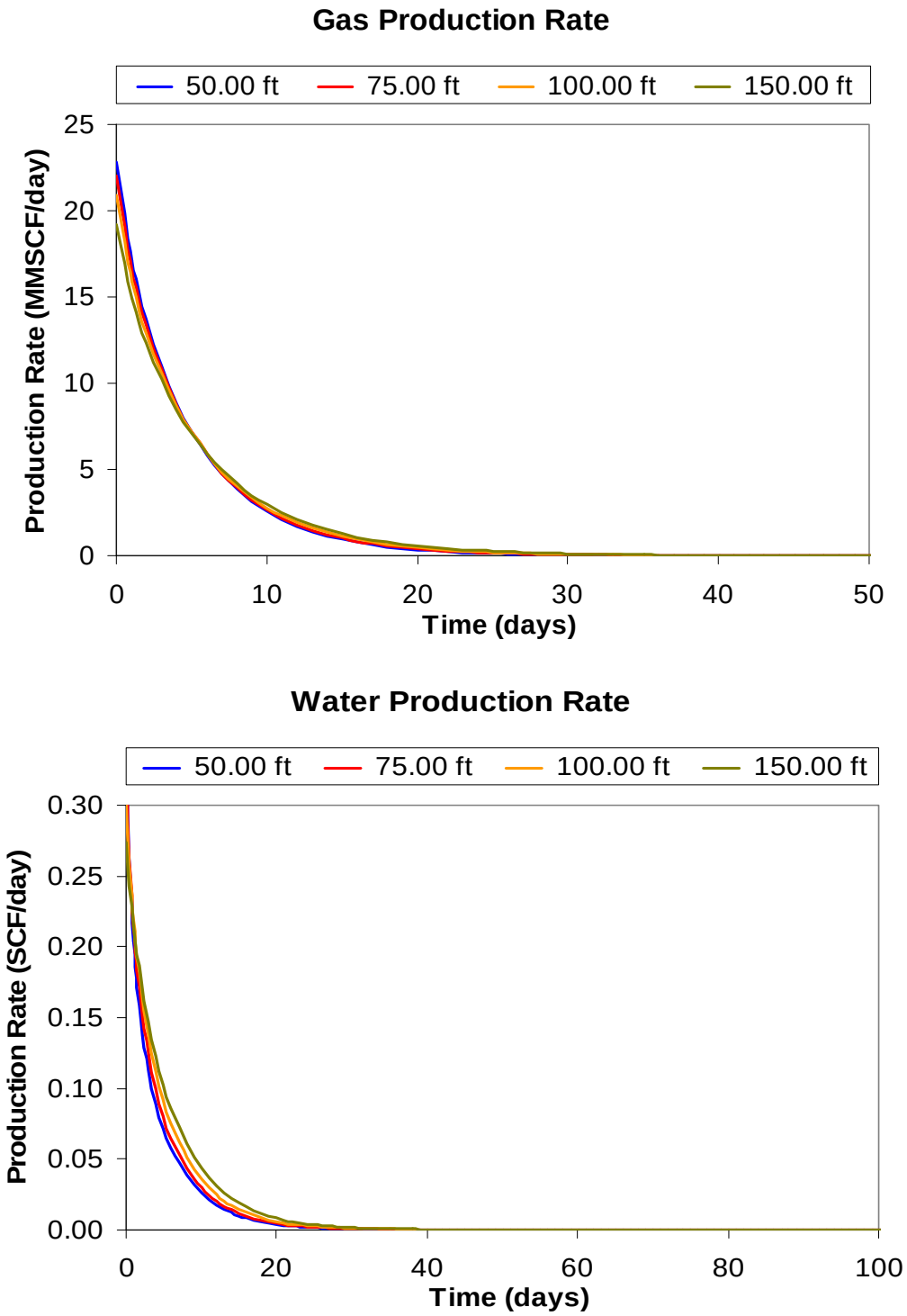

Figure 6-3: The effects of grid block dimensions (Δx and Δy) on the simulation results

6.4 Comparison of Results

In this comparison, methane gas is produced through a production well located at the center of the reservoir at a constant gas flow rate at 2.5 MMSCF/day[11]. The input data of reservoir structure, rock and fluid properties, and initial conditions of this validation case are shown in the Table 6-1 to Table 6-7, and Table 6-14, respectively. In this case, a production well is completed only in the free-gas zone. Figure 6-4 shows the comparison between the cumulative produced gas and cumulative dissociated gas from this work and that from Moridis' work [11]. Note that this comparison is shown in SI unit because the simulation results in Moridis' work were presented in SI unit system. The saturation and temperature distributions along the x-z plane (at about 56 meters from the well) are shown in Figure 6-5, Figure 6-6 shows the distribution plots from the Moridis' work[11].

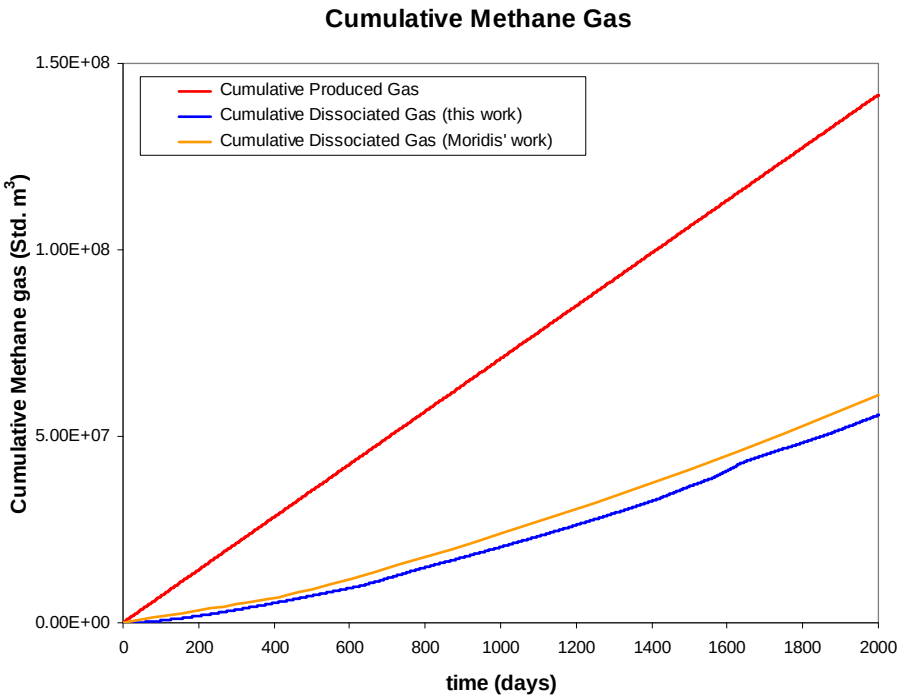

Figure 6-4: Cumulative produced and dissociated gas from Moridis's[11] and this work

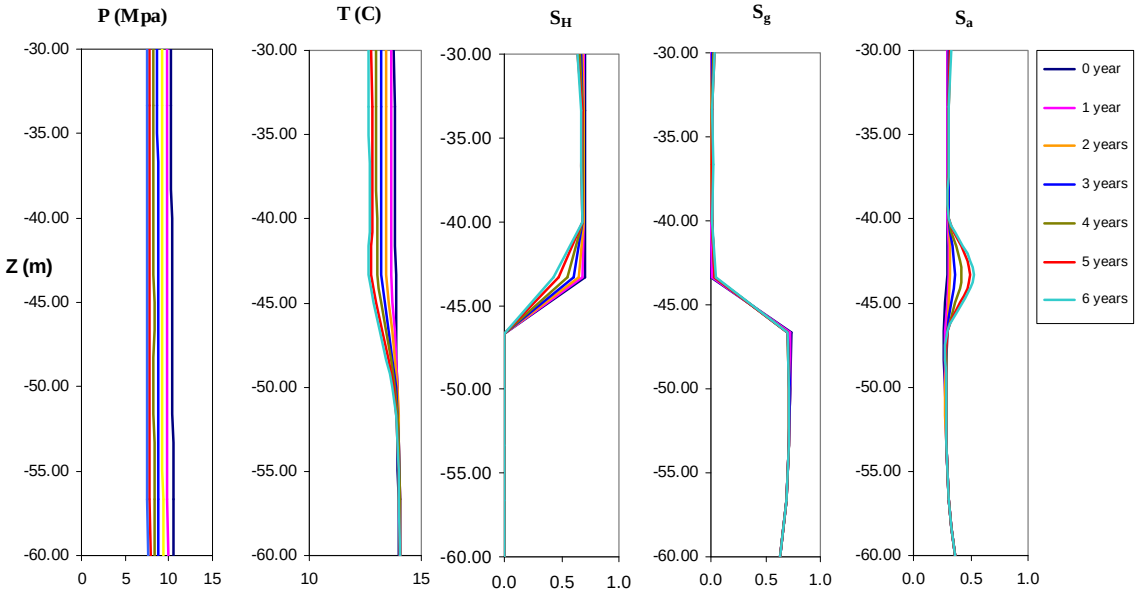

Figure 6-5: Temperature and saturation distributions along the vertical direction (at r = 56 m) of this work

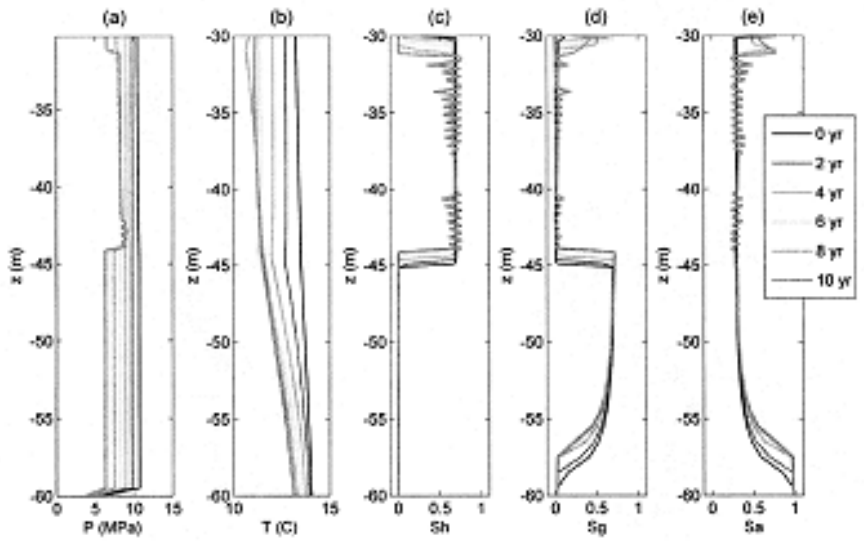

Figure 6-6: Temperature and saturation distribution along the vertical direction (at r = 50 m) of Moridis's work[11]

The simulation results from the two models are somewhat different. The cumulative dissociated gas predicted from Moridis' work is higher than the predictions achieved from this work. The differences can be attributed to the use of different correlations for calculating some parameters and fluid physical properties (such as the amount of methane gas that can dissolve in the aqueous phase, aqueous phase density, aqueous phase viscosity) and the change of rock permeability due to hydrate saturation of the two simulators. Another difference between the two simulators is that the wellbore model was not incorporated in the TOUGH FX simulator which was used in the Moridis' study. For TOUGH FX simulator, the gas production rate from each individual artificial grid layer was calculated by dividing the total gas production rate (2.5 MMSCF/day) by the number of artificial grid layers of the production zone in order to obtain the gas production rate for each layer, and then these calculated values were specified for each layer and they did not change for the entire simulation period. On the other hand, a

wellbore model as suggested by Peaceman is incorporated in this model. Therefore, production rate from each artificial grid layer can change according to the mobility of each mobile phase whereas the total gas production rate is still equal to 2.5 MMSCF/day. This could cause the difference between the results from the two models. The lack of wellbore model in the TOUGH FX simulator limits the capability of the model to simulate the systems that use a specified bottom-hole pressure production scheme. The difference of the coordinate systems that used in the two models might also contribute to the existing disparities in the results from these two models.

The hydrate saturation profiles shown in Figure 6-5 and Figure 6-6 indicate that hydrate dissociation propagates from the initial dissociation front upward to the top of the hydrate zone. This is because the pressure reduction moves upward from the production region (free-gas zone) to the non-production region (hydrate zone). The nearer to the production region, one sees the higher pressure drops (which cause the higher dissociation rate).

Similar to the results from Moridis' study, the emergence of a second dissociation front that forms at the top of the hydrate zone and advances downward is observed. This is because production and dissociation occurred in the system causes the decrease of reservoir temperature. Consequently, the rate of heat transfer from the surrounding above the hydrate zone to the top of hydrate zone increases, and this triggers the hydrate dissociation in the top portion in the hydrate zone.

Figure 6-7 shows the incremental material balance checks of methane and water components of the obtained simulation results which indicate very good material balances on the simulation results.

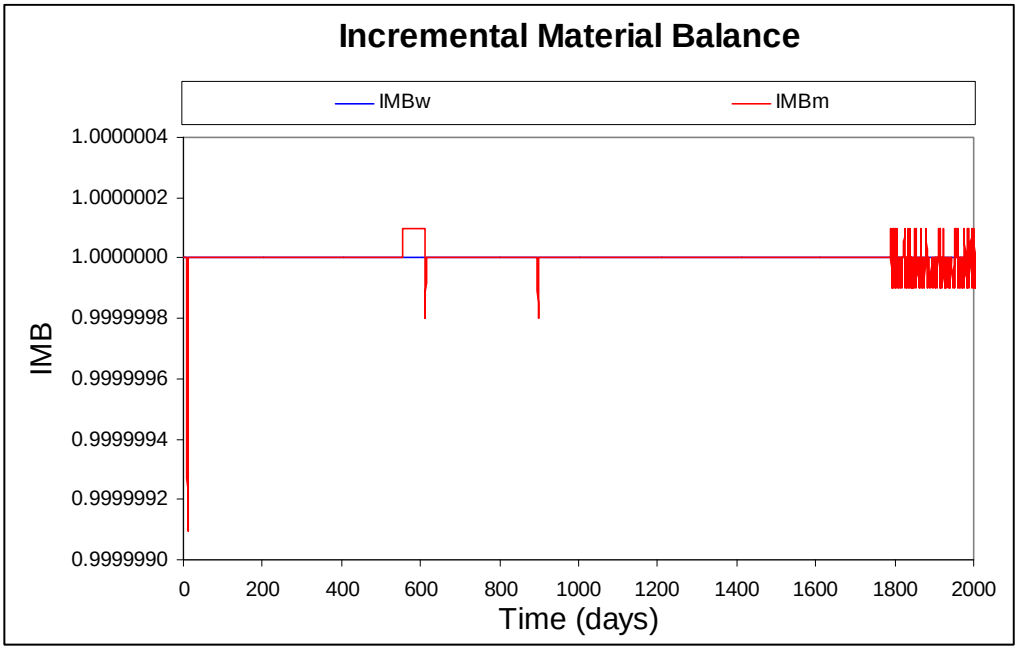

Figure 6-7: Incremental material balance checks for methane and water components

Water saturation, hydrate saturation, gas saturation, and temperature distributions on the x-z plane (cross section of the system) at various times are shown in Figure 6-8 to Figure 6-11, respectively.

According to the hydrate saturation distribution plots, the hydrate saturation just above the production zone is increasing with time. This is because the temperature in this region drops faster than the other region resulting in the hydrate formation in this region. The temperature distribution plots show the drop of temperatures in the dissociation regions because hydrate dissociation is endothermic and it might be able to slow down the dissociation process if the rate of temperature reduction is high enough to make the dissociation pressure below the reservoir pressure (hydrate phase become stable).

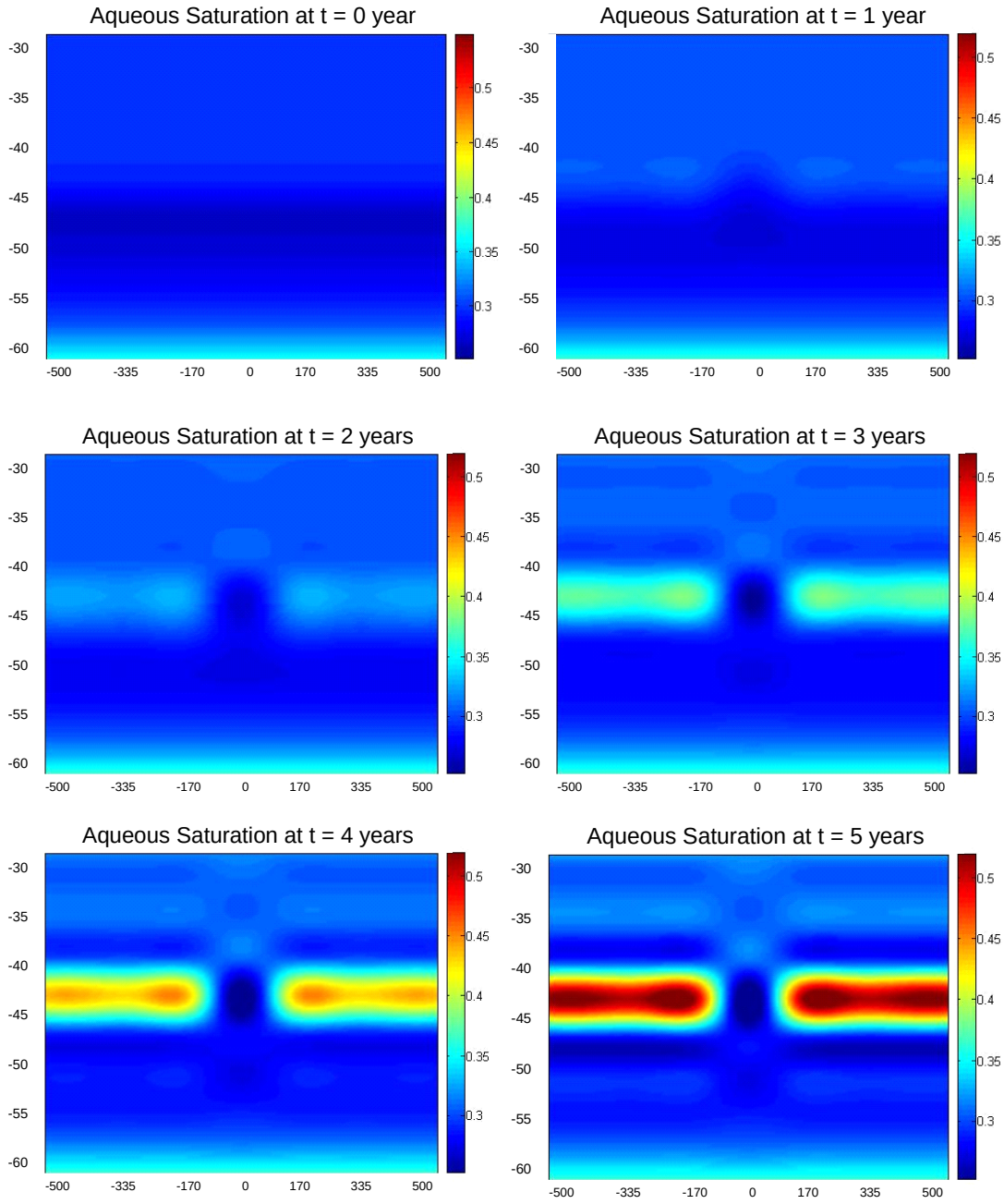

Figure 6-8: The distributions of aqueous phase saturation at different times during the dissociation process

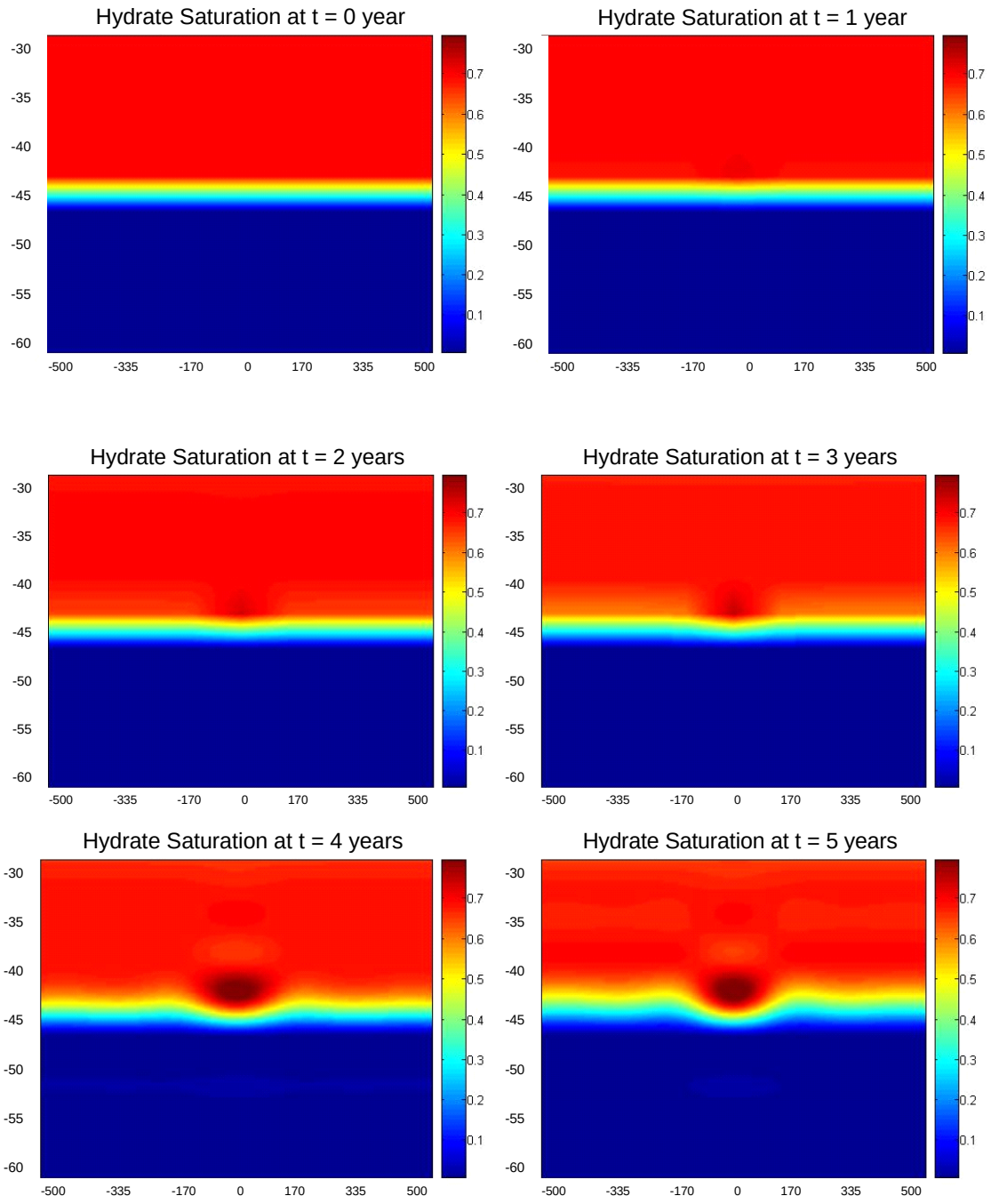

Figure 6-9: The distributions of hydrate phase saturation at different times during the dissociation process

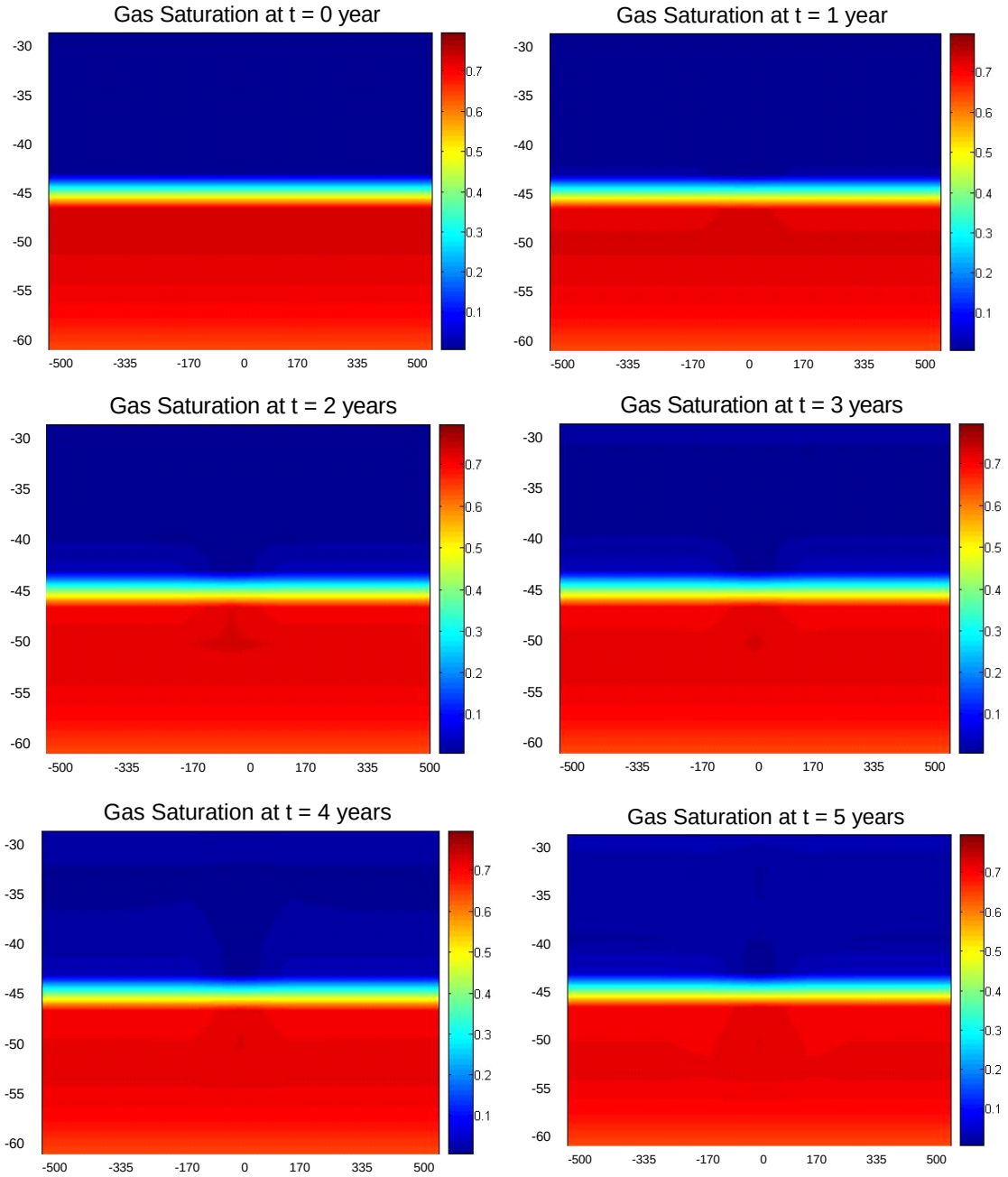

Figure 6-10: The distributions of gas phase saturation at different times during the dissociation process

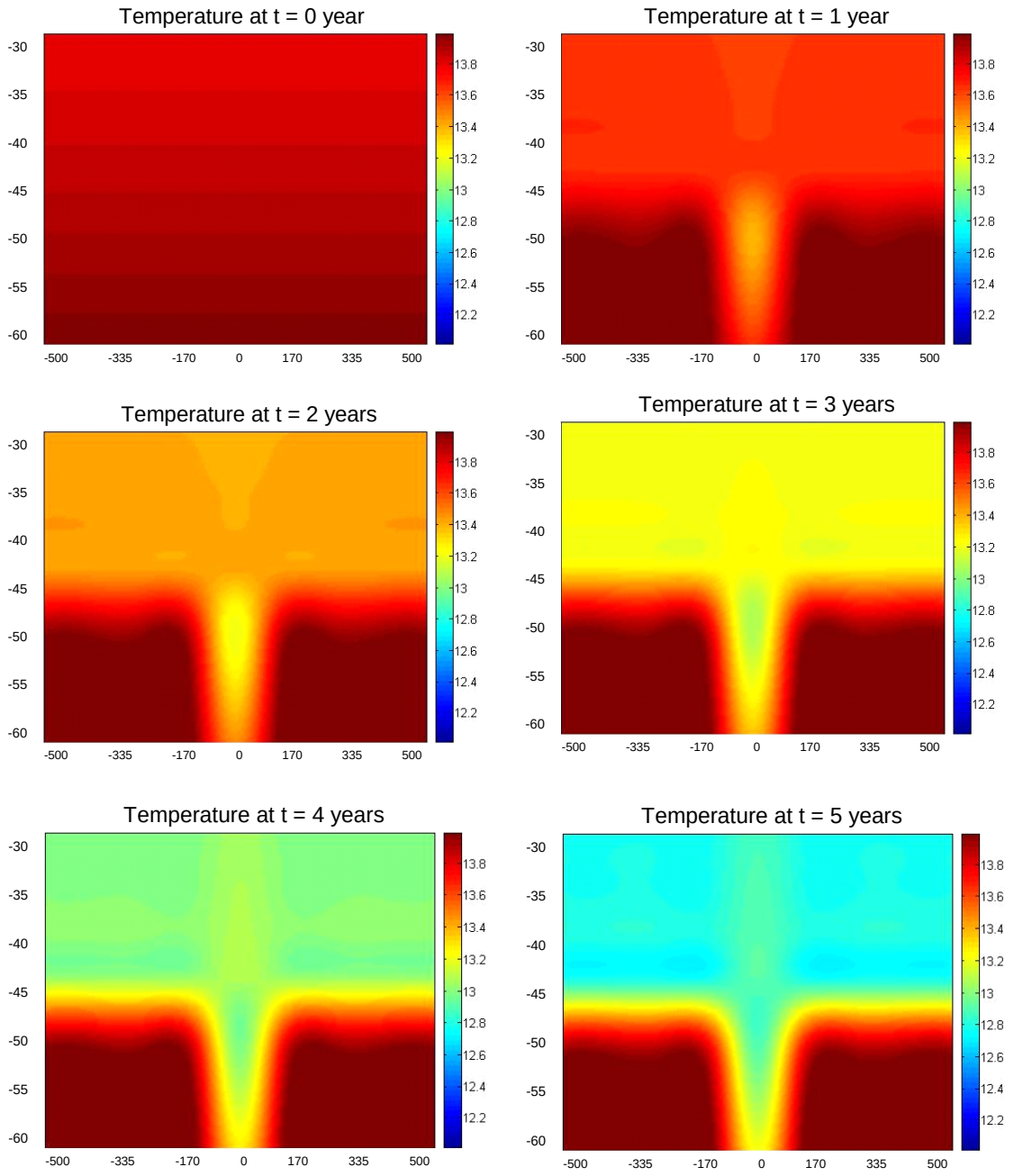

Figure 6-11: Temperature distributions at different times during the dissociation process

Another validation with a simplified gas-hydrate reservoir simulation is also performed in this work. The simulation results from Burshears' study[6] are used in this validation. The reservoir structure used in his study is similar to the reservoir structure shown in Figure 6-1. The characteristics and properties of this reservoir are summarized in Table 6-16. Note that the values of parameters and properties used in the previous validation case are used if they are not provided in the Burshears' work. In this simulation, the production well is operated with a constant gas flow rate at 10 MMSCF/day.

Table 6-16: Characteristics and properties of the reservoir in Burshears' work [6]

Reservoir thickness	100 ft
Gas zone thickness	50 ft
Hydrate zone thickness	50 ft
Reservoir porosity	30%
Reservoir permeability	44 mD
Initial pressure	3,000 psia
Initial temperature	65.8 ^{o}F
Gas composition	100% CH_4
Thermal conductivity	1.56 BTU/ft-Hr-^{o}F
Production rate (gas)	10 MMSCF/day

The reservoir grid structure (number of layers and their thickness) shown in Table 6-7 is also used in this case. Following the same initialization procedure previously discussed, the initial conditions of this reservoir shown in Table 6-17 are realized.

Table 6-17: Reservoir initial conditions used in the validation

Layer no.	P_g (psia)	S_a	S_H	T (^oF)	Remarks
1	0.00	0.0000	0.0000	64.239	Inactive layer with constant T
2	0.00	0.0000	0.0000	64.845	Impermeable layer
3	0.00	0.0000	0.0000	65.376	
4	0.00	0.0000	0.0000	65.754	
5	2980.29	0.3000	0.7000	65.820	Hydrate zone (H+A)
6	2984.66	0.3000	0.7000	65.857	
7	2989.02	0.3000	0.7000	65.893	
8	2993.39	0.3000	0.7000	65.930	
9	2997.75	0.2950	0.7000	65.966	Dissociation front (G+H+A)
10	2984.01	0.2637	0.0000	66.015	Free gas zone (G+A)
11	2984.75	0.2709	0.0000	66.048	
12	2985.50	0.2832	0.0000	66.081	
13	2986.24	0.3071	0.0000	66.115	
14	2986.98	0.3650	0.0000	66.150	
15	0.00	0.0000	0.0000	66.262	Impermeable layer
16	0.00	0.0000	0.0000	66.620	
17	0.00	0.0000	0.0000	67.123	
18	0.00	0.0000	0.0000	67.697	Inactive layer with constant T

Figure 6-12 (a) shows a very good agreement between the cumulative dissociated gas predictions from Burshears' work and this study. Figure 6-12 (b) shows the change of the simulation results when different heat transfer mechanisms are taken into account in the calculation.

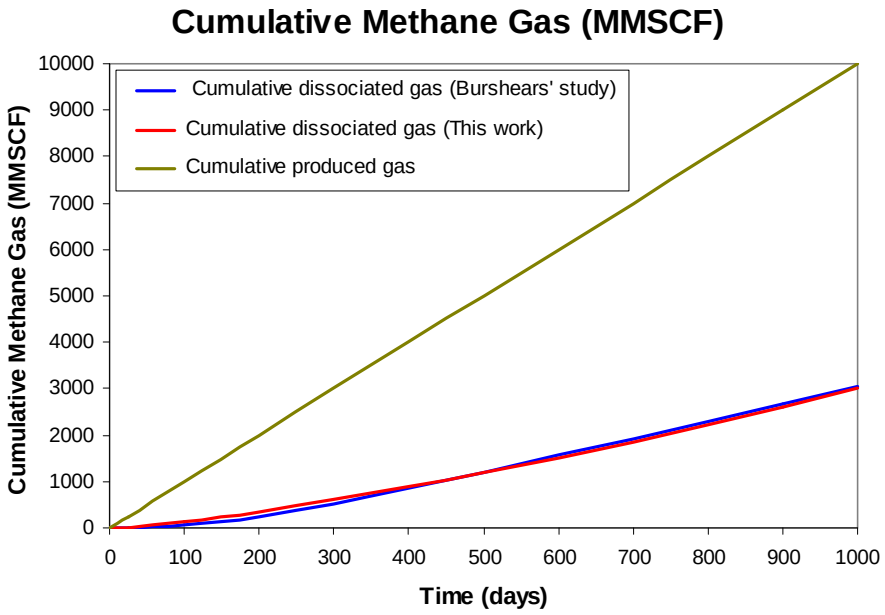

(a) Comparison between the results from Burshears' work and this study

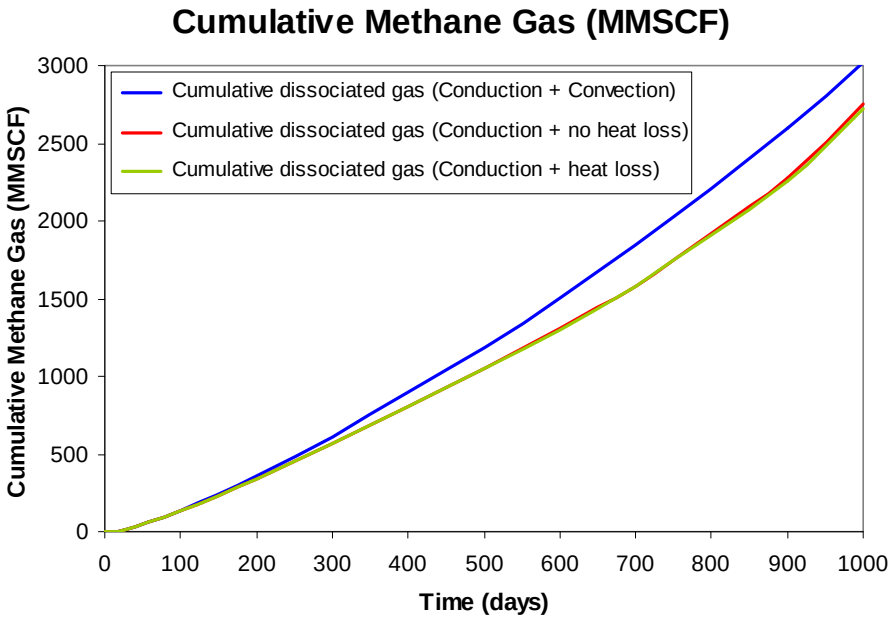

(b) The effect of heat transfer mechanism on the simulation results

Figure 6-12: Cumulative methane gas

The dark blue line in Figure 6-12 (b) represents the cumulative dissociated gas when heat conduction, heat convection, and heat loss from the production are taken into account. In the same figure, the red line represents the cumulative dissociated gas when only heat conduction is taken into account and the green line represents the cumulative dissociated gas when heat conduction and heat loss by taking fluids out of the system are taken into account. The red and the green lines are not significantly different indicating that the effect of heat loss by taking the fluids out of the system does not significantly affect the simulation results. However, it shows that the simulation results change when heat convection is taken into account indicating the needs of incorporation of heat convection into the model for more accurate results. The result indicates higher dissociation when heat of convection is taken into account because the model predicts more effective heat transfer between hot and cold regions for this case. Consequently, the model predicts higher heat support for the dissociation resulting in the higher dissociation rate in this case. Note that, according to the simulation results generated, the difference of the predicted cumulative dissociated gases of the two cases was up to 9.5 percents (for 1,000 days of production period).

The two comparisons show the consistency of the simulation results of the model developed in this work and those from the models developed in previous studies indicating the reliability of the model developed in this work.

6.5 Study of Production Characteristics

In this section, the gas production characteristics from a class 1 methane hydrate reservoir are studied using the simulator developed in this work. Note that the initial condition and rock and fluid properties from the validation (with Burshears' work) section are used as the input data for all of the further simulation studies in this work.

6.5.1 Production Characteristics of Conventional Gas and Gas-Hydrate Systems

In this section, the production characteristics from a methane-hydrate reservoir is studied and compared against the production characteristics of conventional gas (methane) reservoirs. The two systems have the same initial conditions for the free-gas zone. The thickness of free-gas zone is 50 feet. The conventional gas reservoir has no hydrate zone and it is also treated as a non-isothermal system. For each system, there is only one production well located at the center of the system and it is completed in the middle of the initial free-gas zone. The production well is operated with constant bottom-hole pressure at 14.7 psia. The reservoir properties of the two systems are summarized in Table 6-18 and Figure 6-13 shows the structure of the two reservoirs.

Figures 6-14 and 6-15 show the gas and water production characteristics of the two systems. Note that the simulator developed in this study was also validated by comparing the obtained simulation results for a conventional methane gas reservoir with the simulation results (for the same reservoir) from a commercial reservoir simulator (CMG). The details of the system used in this comparison and the compared results are shown in Appendix B. The slight differences of the results are attributed to the use of

different correlations for calculating fluid properties (such as density and viscosity) in the two simulators.

Table 6-18: Reservoir properties of the conventional and methane hydrate reservoirs

Properties	Methane-hydrate reservoir	Conventional gas reservoir
Reservoir thickness	100 ft	50 ft
Gas zone thickness	50 ft	50 ft
Hydrate zone thickness	50 ft	0 ft
Reservoir porosity	30%	30%
Reservoir permeability	44 mD	44 mD
Initial pressure	3,000 psia	3,000 psia
Intial temperature	65.8 ^{o}F	65.8 ^{o}F
Gas composition	100% CH_4	100% CH_4
Thermal conductivity	1.56 BTU/ft-Hr-^{o}F	1.56 BTU/ft-Hr-^{o}F

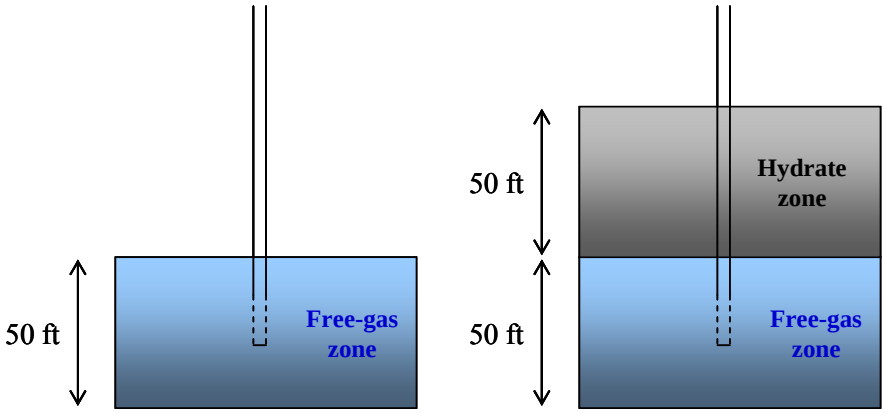

(a) Conventional gas reservoir (b) gas-hydrate reservoir

Figure 6-13: Structure of a conventional gas and gas-hydrate reservoirs

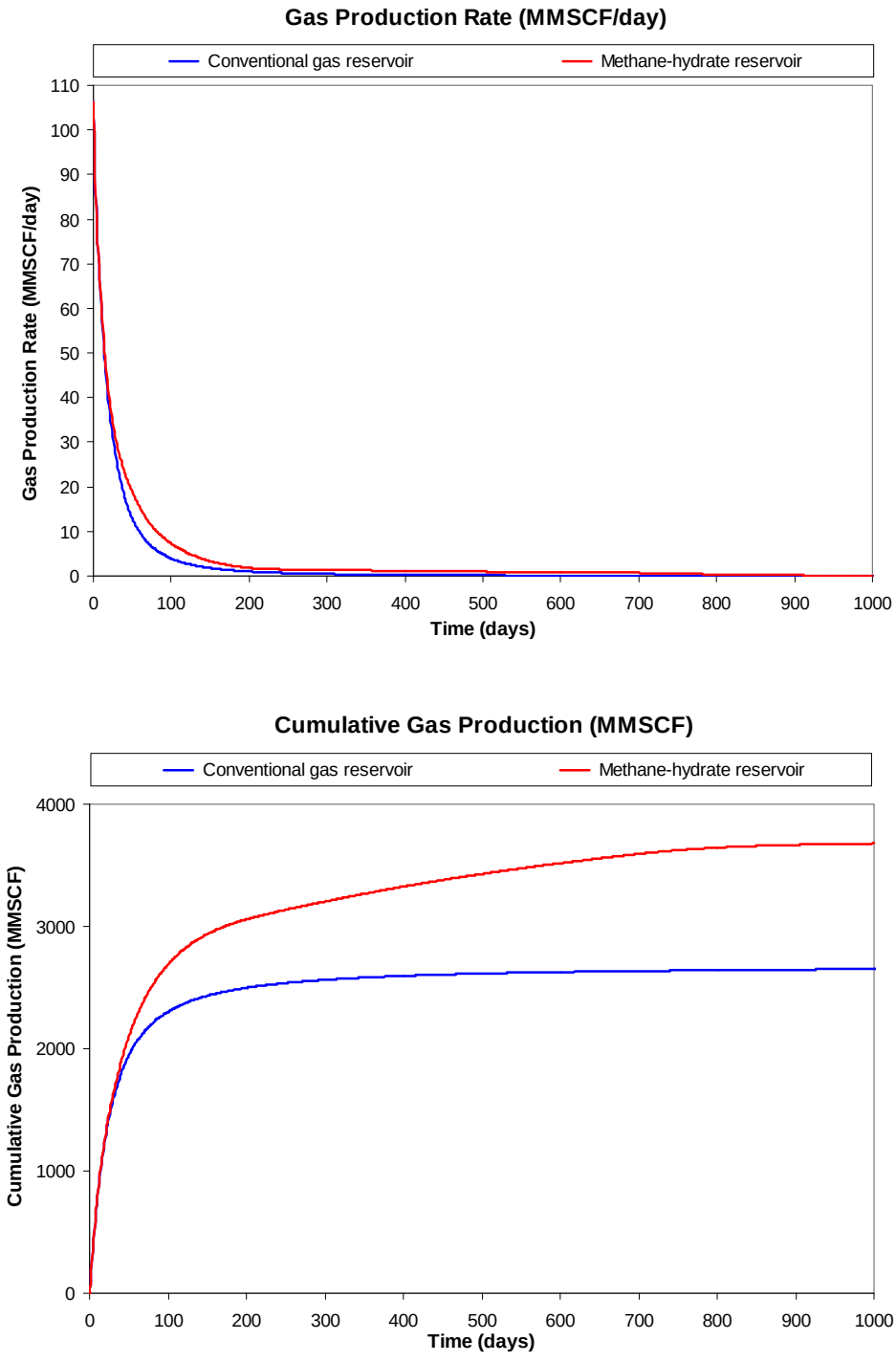

Figure 6-14: Gas Production characteristics of hydrate and conventional gas systems

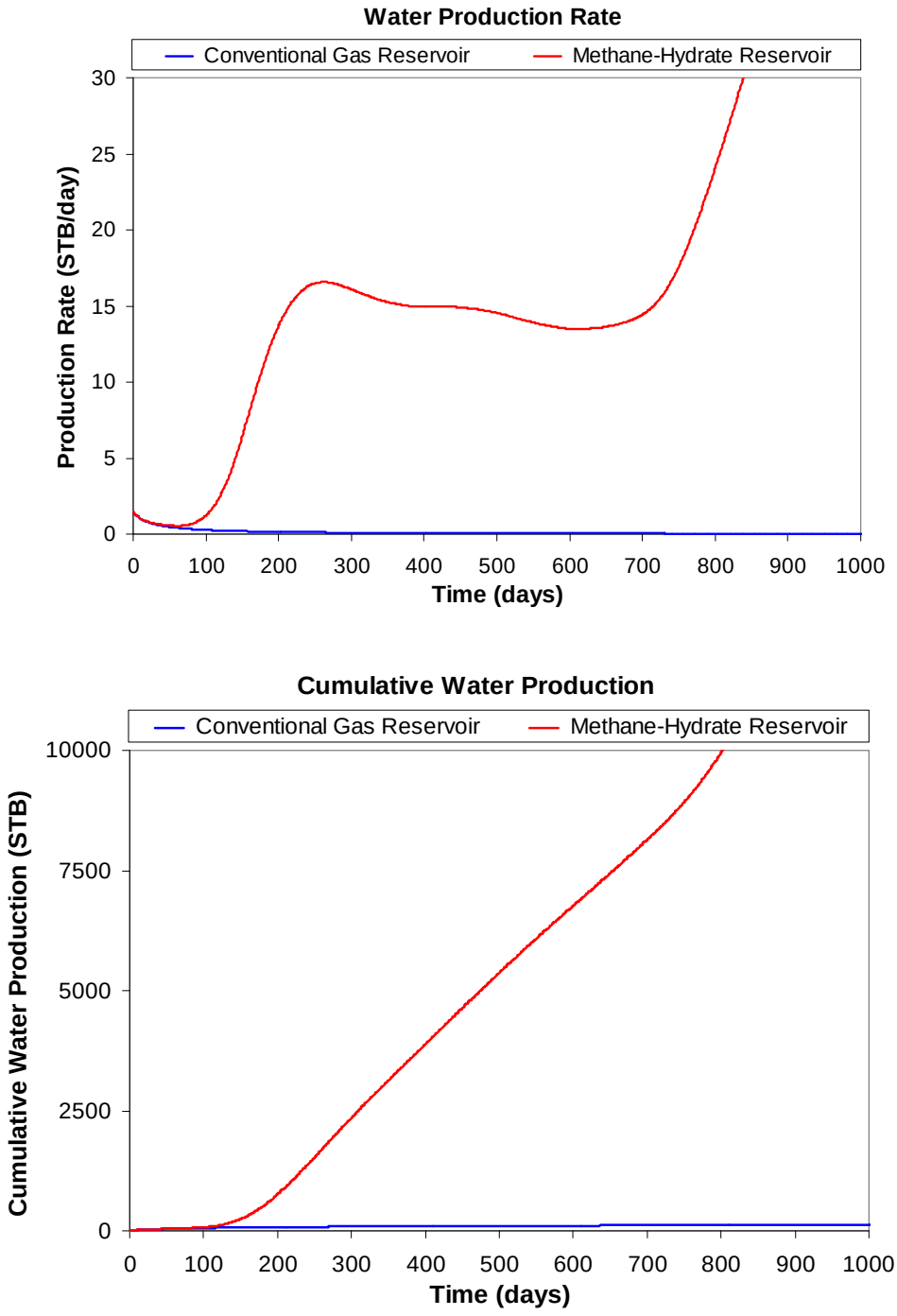

Figure 6-15: Water Production characteristics of hydrate and conventional gas systems

According to the simulation results, gas production rate from the gas-hydrate reservoir is higher than that from the conventional gas reservoir because gas hydrate phase is capable of providing additional amount of gas to the system. From this simulation exercise, the cumulative gas production at the end of 1,000 days from the methane hydrate reservoir (3,678.4 MMSCF) was higher than the cumulative gas production from the conventional gas reservoir (2,651.4 MMSCF) by about 38.74 percent and the gas production rate from the methane hydrate reservoir is still higher than that from the conventional gas reservoir after 1,000 days of operation.

It can be seen that both gas and water production rates exponentially decline with time for a conventional gas reservoir. However, for a methane-hydrate reservoir, gas production rate decreases with time whereas water production rate increases with time. This is because the dissociation of methane hydrate releases both free gas and water to the system. The released water flows down from the hydrate zone to the lower part of the reservoir due to the gravitational forces resulting in the increase of aqueous saturation in the lower part of the free-gas zone. Figure 6-16 shows the significant increase of aqueous saturation of the well block (for the gas-hydrate system) resulting in the increase of the mobility of aqueous phase. On the other hand, aqueous phase saturation for the conventional gas reservoir increased in the early period of production and gradually decreased after approximately 300 days of production. One can see that, for the gas hydrate reservoir, the shapes of water production rate and aqueous phase saturation plots are consistent.

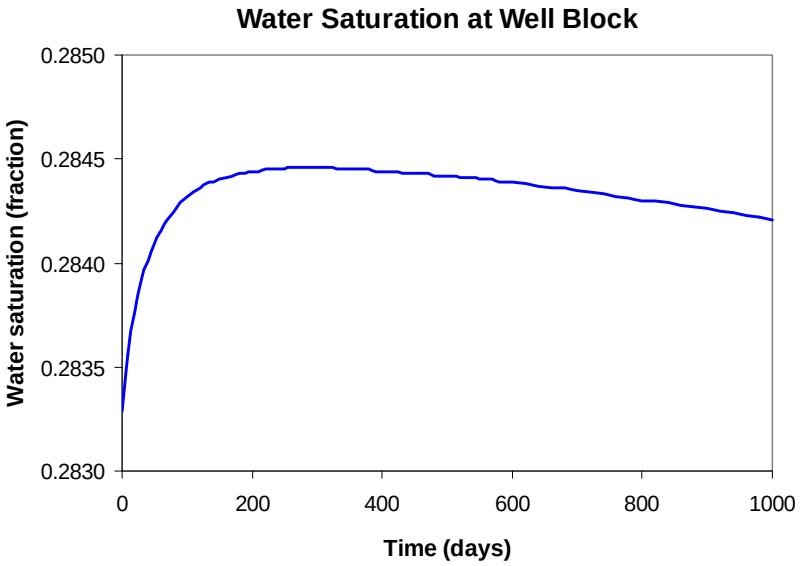

(a) Conventional gas reservoir

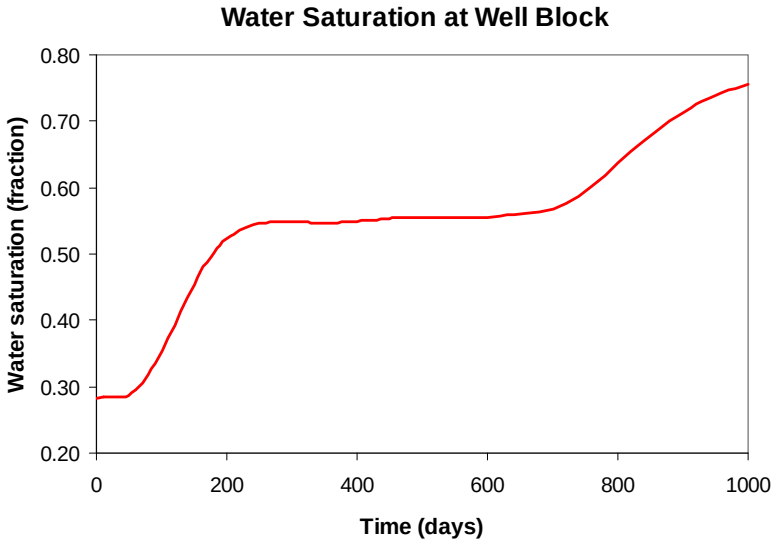

(b) Methane-hydrate reservoir

Figure 6-16: Water saturation of well block of conventional gas and hydrate systems

For the gas hydrate reservoir, aqueous phase saturation at the well block decreases during the early period of production because some of aqueous phase is taken out from the system through the production well. Aqueous phase saturation starts increasing at the

end of 60 days because the released water from the dissociation in the hydrate zone flows downward and reaches the well block. The amount of water entering to the well block is higher than the amount of water leaving out from the block (some water flows down to the lower portion and some water is taken out through the production well) resulting in the increase of aqueous phase saturation in this block. The increase of aqueous phase mobility yields the higher water production rate resulting in the decrease of the difference between the amount of water entering and leaving the well block. Consequently, the aqueous phase saturation increases with the lower rate and becomes more or less constant. This approximately happens during the first 250 to 700 days of production. Meanwhile the aqueous phase saturations as well as pressures of the blocks below the well block keep increasing causing aqueous phase in the well block more difficult to flow downward whereas the amount of water (from the dissociation) entering to the well block does not decrease at the same rate. Consequently, the aqueous phase in the well block starts accumulating. As a result, aqueous phase saturation in the well block starts increasing which can be seen in the late production period in Figure 6-16.

Figure 6-17 shows the well block pressure at various times of the conventional and methane-hydrate reservoirs. As expected, the well-block pressure of the conventional gas reservoir more rapidly decreases than the block pressure of the methane-hydrate reservoir resulting in the more rapid decrease of gas production rate in the conventional gas reservoir. This is because the hydrate decomposition releases methane gas and water to the system. Accordingly, the well-block pressure of the methane hydrate system is higher than the well-block pressure of the conventional gas system at any particular time. From this simulation study, the gas pressure of the well block at the end of 1,000 days in

the methane hydrate reservoir is about 378 psia whereas the well block pressure in the conventional gas system at the end of 1,000 days is 28.65 psia.

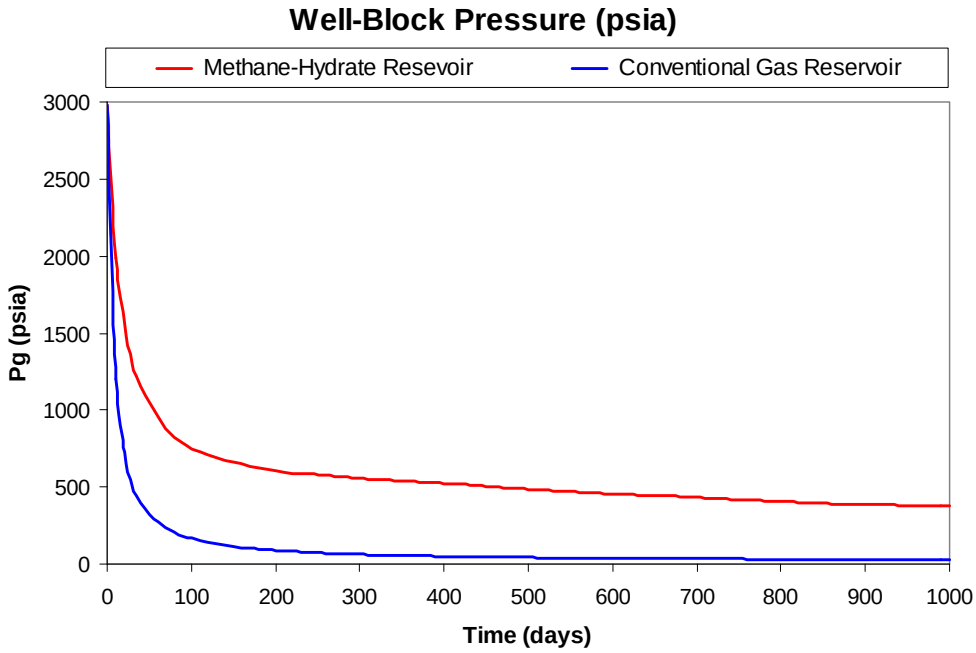

Figure 6-17: Well-block pressure of the conventional gas and methane-hydrate reservoirs

As expected, the cumulative gas production from the methane-hydrate reservoir is higher because there is more amount of gas available (free gas in the free-gas zone plus methane gas in methane hydrates). For this particular example, if the thickness of the conventional gas reservoir becomes 70 feet, the cumulative gas production at the end of 1,000 days of the new conventional gas reservoir and the methane-hydrate reservoirs will be approximately the same. Figure 6-18 shows the cumulative gas productions of the two systems. The cumulative gas production curves of the two systems are different even though their cumulative gas productions at the end of 1,000 days are approximately the same. This is because the initial thickness of free gas zone of the gas hydrate reservoir is 50 feet and the thickness of this zone increases with time due to the dissociation of gas

hydrate in the hydrate zone. On the other hand, the initial thickness of free gas zone of the conventional gas reservoir is 70 feet and it never changes with time. Therefore, there is more gas available to be produced for the conventional gas reservoir resulting in the higher gas production rate during the early period of production. Note that the same cumulative gas production in the case of conventional gas reservoir achieved approximately two times faster (at about 500 days of operation).

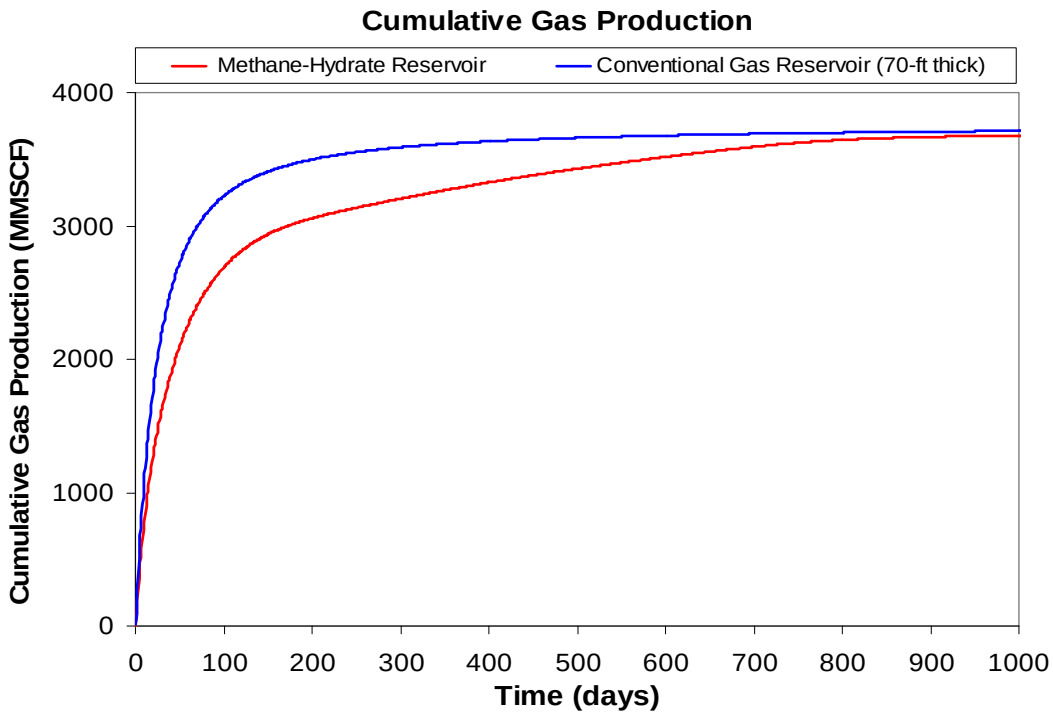

Figure 6-18: Gas production of the conventional gas and methane-hydrate reservoirs

One can conclude from this simulation study that the presence of gas hydrate on the top of free-gas reservoir can significantly improve the productivity of the underlying gas reservoir. The production characteristics of gas-hydrate reservoirs and conventional gas reservoirs (using a constant bottom-hole pressure production scheme) are different. For a conventional gas reservoir, both gas and water production rates decrease with time,

whereas, for a gas-hydrate reservoir, gas production rate decreases with time meanwhile water production rate increases with time.

The depressurization paths at three different locations in the reservoir on the *P-T* diagram of methane-hydrate equilibrium are shown in Figure 6-19.

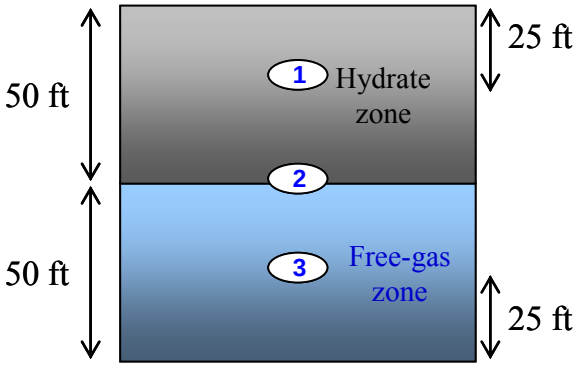

(a) Investigated points

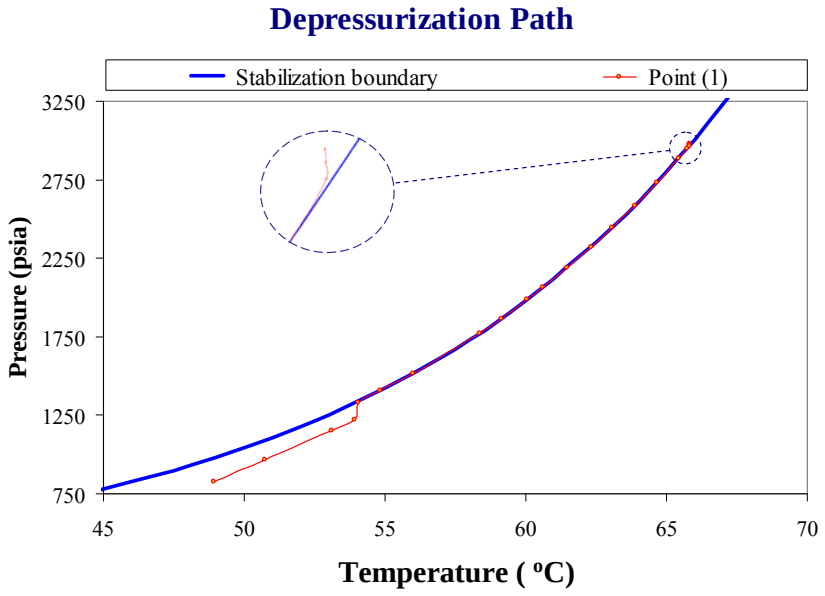

(b) Depressurization path at point 1

Figure 6-13: Depressurization paths of the different points in Class 1 of methane-hydrate reservoir

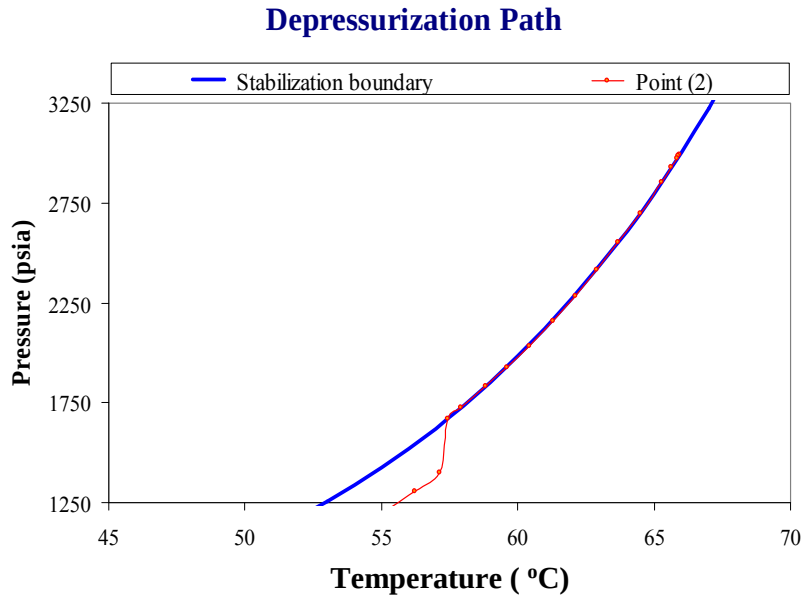

(c) Depressurization path at point 2

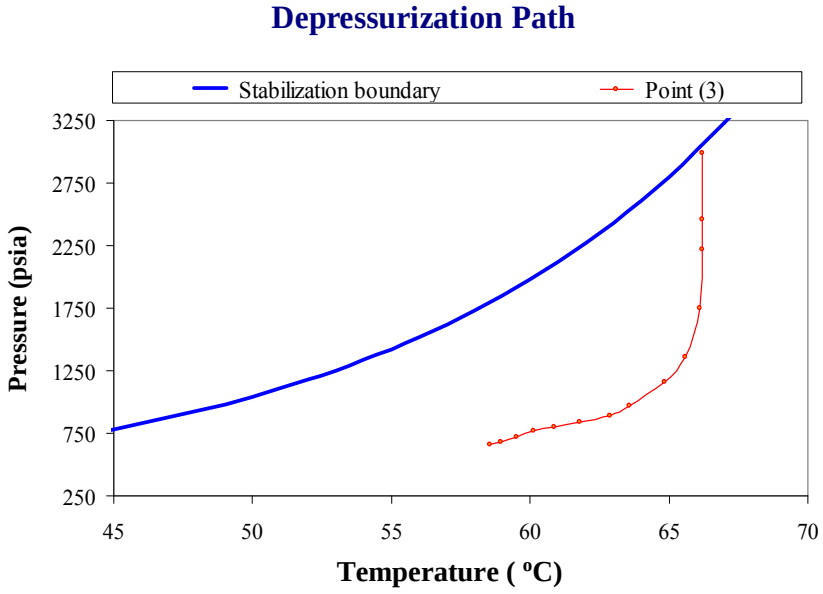

(d) Depressurization path at point 3

Figure 6-19 (cont.): Depressurization paths of the different points in Class 1 of methane-hydrate reservoir

Figure 6-19 (b) represents the depressurization path of point 1 for 1,000 days of production. For this point, the depressurization path starts from the point inside the hydrate stabilization zone. Once the dissociation of hydrate phase at this point takes place, the *T*-*P* condition at that point is on the 3-phase equilibrium line and after that the change of *P*-*T* conditions at that point follows the equilibrium line. The *P*-*T* condition at this point will go outside the hydrate stabilization zone when all the hydrate phase at that point dissociates. At point 2 (Figure 6-19 (c)), the similar path as point 1 is obtained but the starting point of this path is on the equilibrium line as the three phases coexist at the initial condition. Similarly, at point 3 (Figure 6-19 (d)), the dissociation path starts from the point outside the hydrate stabilization zone and it does not move into the hydrate stabilization zone because no hydrate formation takes place at this point for the entire simulation time.

6.5.2 Effect of Well-Completion Locations

Penetration location of a production well can affect the characteristics and performance of the production. In this section, the effects of four different well-completion locations shown in Figure 6-20 on production characteristics and performance are examined. The height of the completion zone in every case is 10 feet. In this study, three well-completion locations are in the free-gas zone and one well-completion location is in the dissociation front layer. The penetrating zone of the production wells for Cases 1, 2, and 3 are located at the middle, top, and bottom of the initial free-gas zone, respectively. For Case 4, the well is completed in the initial dissociation layer (the bottom

of the initial hydrate zone). Note that the well-completion locations in each case do not change for the entire simulation. The production well is operated with a constant bottom-hole pressure at 14.7 psia for every case. Figures 6-21 and 6-22 show the characteristics of gas and water productions from different well-completion locations, respectively.

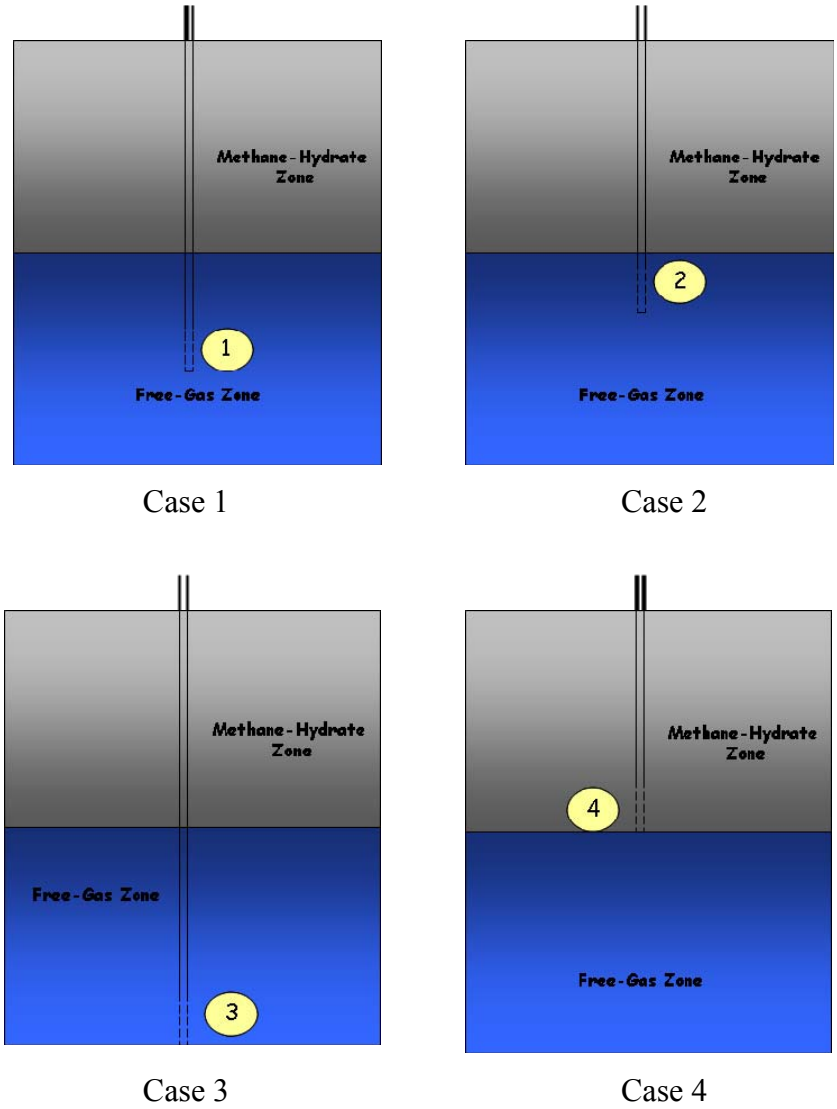

Figure 6-20: Well-completion locations

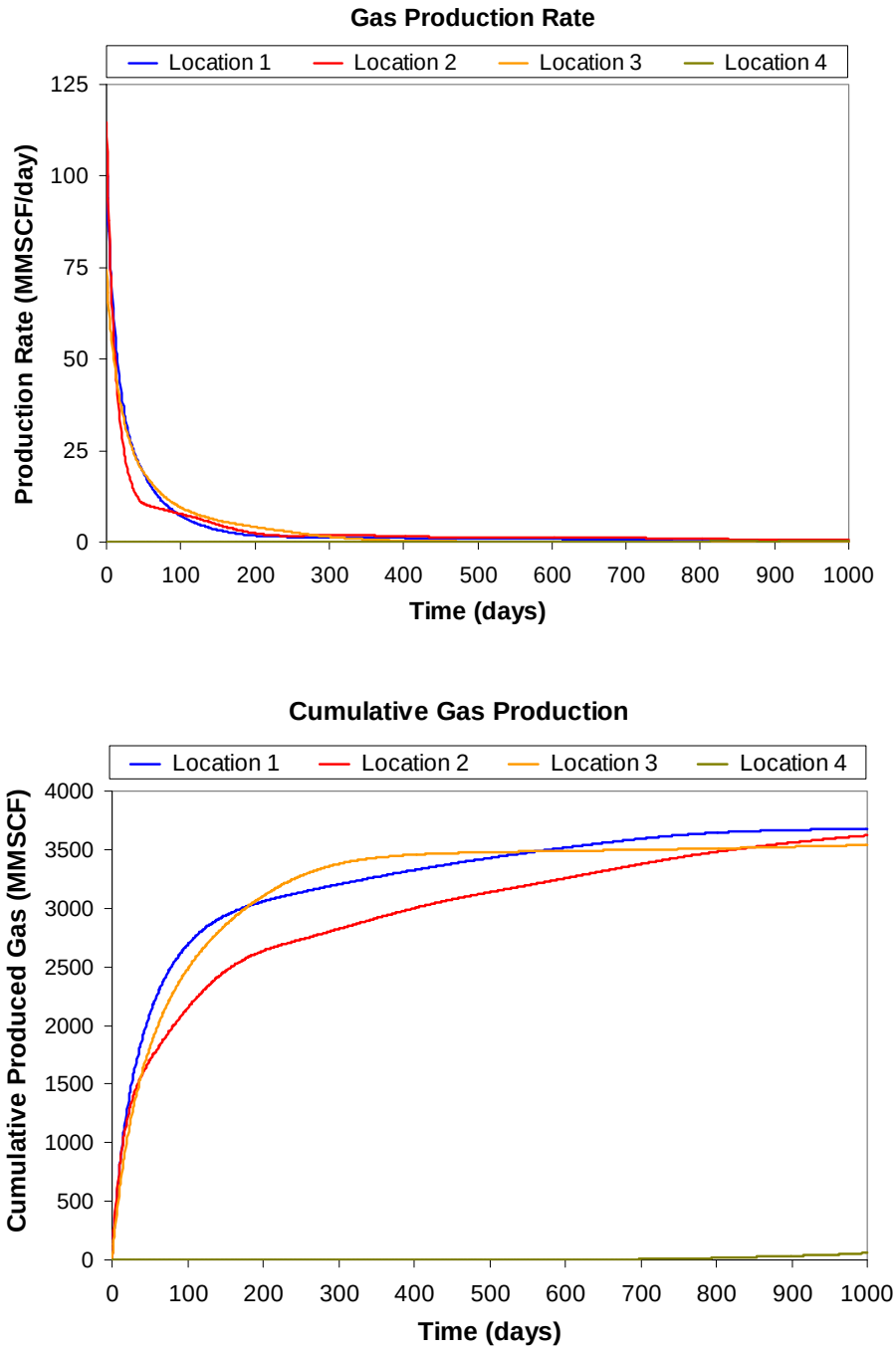

Figure 6-21: Gas production for different well-completion locations

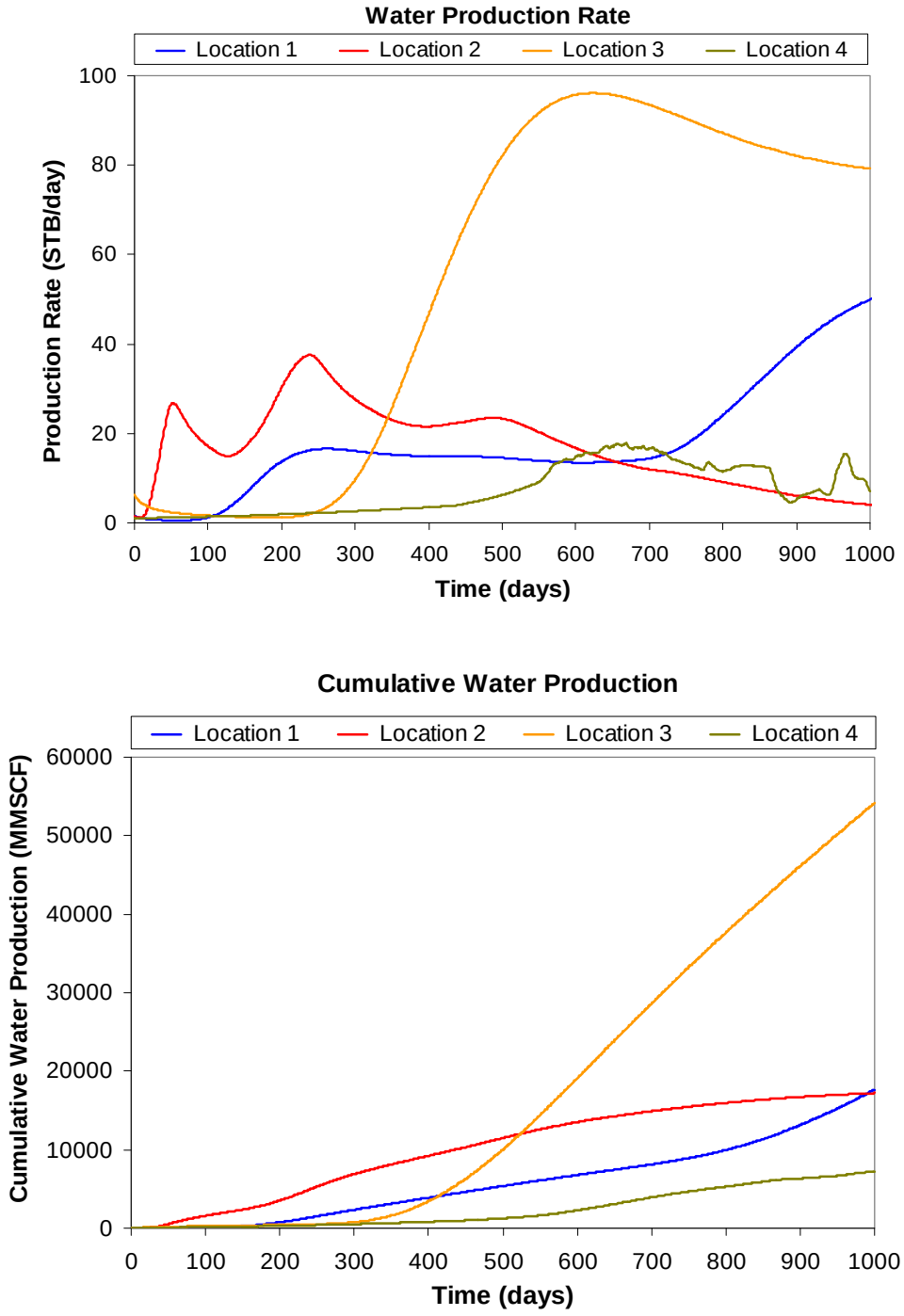

Figure 6-22: Water production for different well-completion locations

The simulation results shows that gas production rates exponentially decrease with time for every case, meanwhile the water production rates for each case have different characteristics because the change of aqueous saturation at the well block with time for each case are different. The water production characteristic for Case 1 has been discussed in the previous section (6.5.1). For Case 2, the increase of aqueous saturation of the well block happened earlier than Case 1 because the well block is just below the dissociation front. Hence, the released water from the dissociation at the front requires less time to flow to the well block. The increase of the aqueous phase saturation improves the mobility of aqueous phase resulting in the increase of water production rate.

The change of aqueous phase saturation of the well block is controlled by the amount of released water (from the dissociation) entering to the well block, the amount of water leaving the well block through the production well, and the amount of water flowing down to the lower part of the free-gas zone. This difference controls the change of aqueous phase saturation and, consequently, water production rate. At about the end of 500 days of production, aqueous phase saturation started decreasing because the amount of aqueous phase leaving the well block was higher than the amount of aqueous phase entering the well block. Consequently, water production rate declined after 500 days of production in this case. For Case 3, it is similar to Case 2 but the increase of aqueous phase saturation required more time because the well block location of this case is lower than the well block location in Case 2. Again, the change of aqueous phase saturation of the well block is controlled by the difference of the amount of water entering and leaving the well block. It can be seen that the water production rate at late time in Case 3 is higher than that in Cases 1 and 2 because the well-completion location in Case 3 is lower

than the locations in the other two cases, which means that aqueous phase saturation of the well block in Case 3 is higher than the aqueous saturations in the other two cases. Consequently, the water production rate in Case 3 is the highest. Similarly, the water production rate of Case 1 is higher than the water production rate of Case 2 because the well-completion location in Case 1 is lower than the well-completion location in Case 2.

For Case 4, the water and gas production rates are less than the rates in the other three cases because the permeability of the well block in this case is significantly smaller (causing by the presence of methane hydrate) than the permeabilities in the other cases. The water production rate increased with time because of the increase of the rock permeability caused by the decrease of hydrate saturation (due to the dissociation). Therefore, it is suggested that one should not complete a well (either producer or injector or both) in the hydrate zone because of the aforementioned permeability issue.

The gas production rates in Cases 2 and 3 decrease more rapidly than the gas production rate in Case 1 because of the effects of low permeability region above the completion zone (for Case 2) and the effects of no flow boundary below the completion zone (for Case 3). The gas production rate in Case 4 is significantly lower than the gas production rates in the other cases due to the permeability issue discussed before.

The gas production rate in Case 2 drops more rapidly than that of Case 1 during the early period of production. Hence, the cumulative gas production in Case 1 is higher than that of Case 2 during 1,000 days of production (see Figure 6-21). However, the cumulative gas production in Case 2 was, eventually, a bit higher than Case 1 (see Figure 6-23). This is because the completion zone of the well in Case 2 is higher than the completion zone in Case 1 providing that the gas saturation of the well block in Case 2 is

higher than the gas saturation of the well block in Case 1. Accordingly, more gas is available to be produced in Case 2.

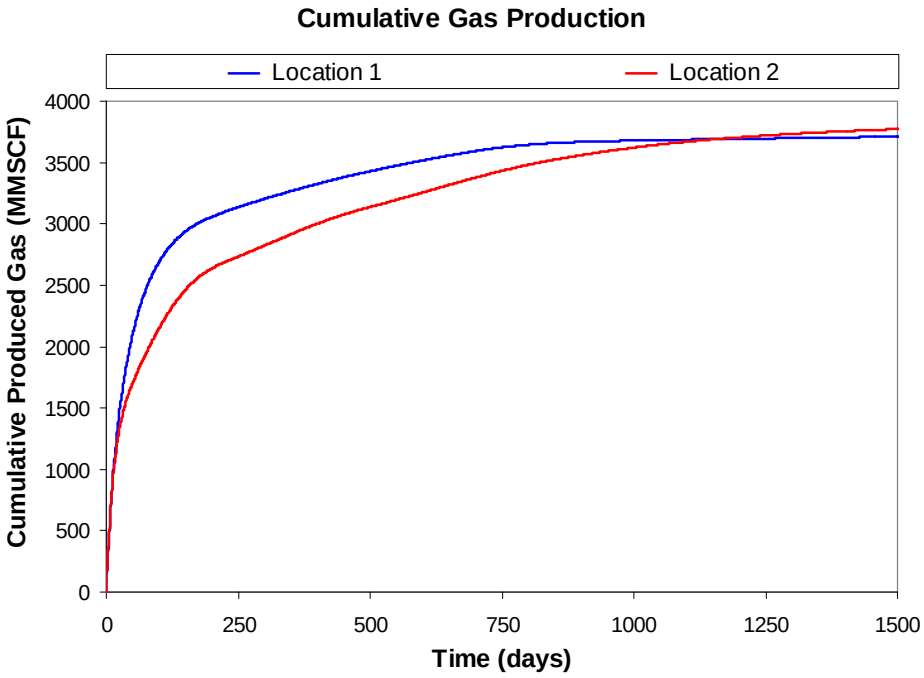

Figure 6-23: Cumulative produced gas during 1,500 days of operation

Figure 6-24 shows percent hydrate recovery and cumulative dissociated gas. Case 1 can dissociate methane-hydrate faster than the other cases during the first 500 days of operation. However, at the end, Case 2 can dissociate all the methane-hydrate a bit sooner than Case 1. Case 4 requires much more time than the other cases to dissociate all methane-hydrate in the reservoir because it is harder to take the fluids out of the reservoir (through the production well) due to low permeability issue previously mentioned.

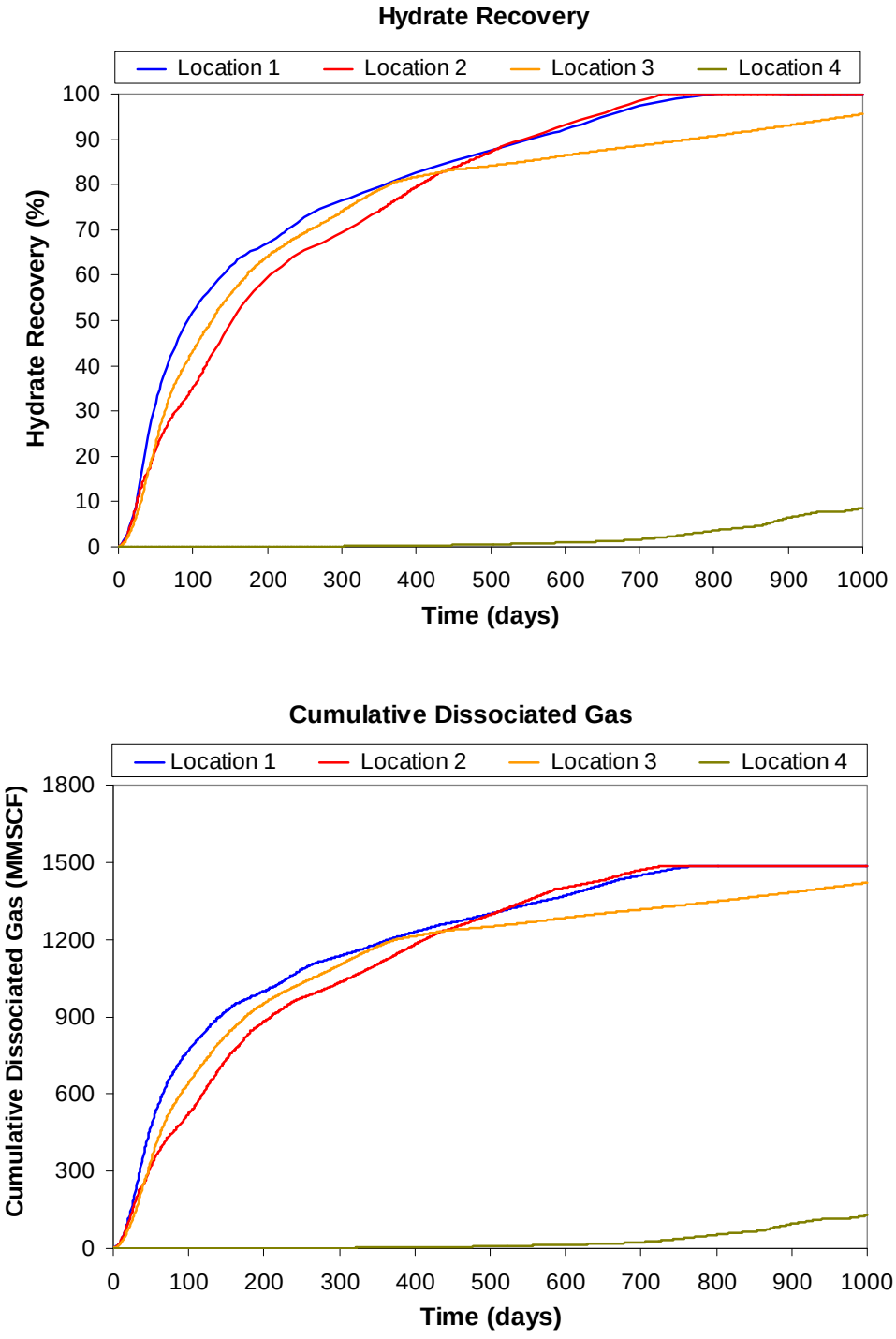

Figure 6-24: Hydrate recovery and cumulative dissociated gas for different well-completion locations

For the previous four cases, the well-completion locations do not move with respect to the location of dissociation front which moves upward during the dissociation process. The following additional cases in which the well-completion locations are moved with respect to the dissociation front are examined. In Case A, a production well is initially completed in the middle of the initial free gas zone. The thickness of free-gas zone increases with time because the dissociation front moves upward during the dissociation process. Therefore, the completion location must be moved upward with respect to the dissociation front location so that the completion location is always in the middle of free-gas zone. In Case B, a production well is initially completed at the top of the initial free-gas zone and just below the initial dissociation front. Similarly, the completion location must be moved with respect to the location of the dissociation front so that the completion location is always at the top of free-gas zone. Figure 6-25 shows the cumulative gas and water productions of these two cases as compared to the production plots of Case 1. Figure 6-25 shows that Cases A and B yield higher cumulative gas production than Case 1 (by 6.75 and 3.36 percents, respectively) indicating that moving the completion location improves gas production performance. This is because the completion locations in cases A and B are moved to higher locations which have larger gas saturation resulting in higher gas production rate and cumulative gas production and lower water production (Figure 6-25). Case B yields lower gas production than Case A (by 3.28 percent) because the completion location in Case B is just below the dissociation front which releases water from the dissociation process at the time, resulting in the high water saturation just below the dissociation front.

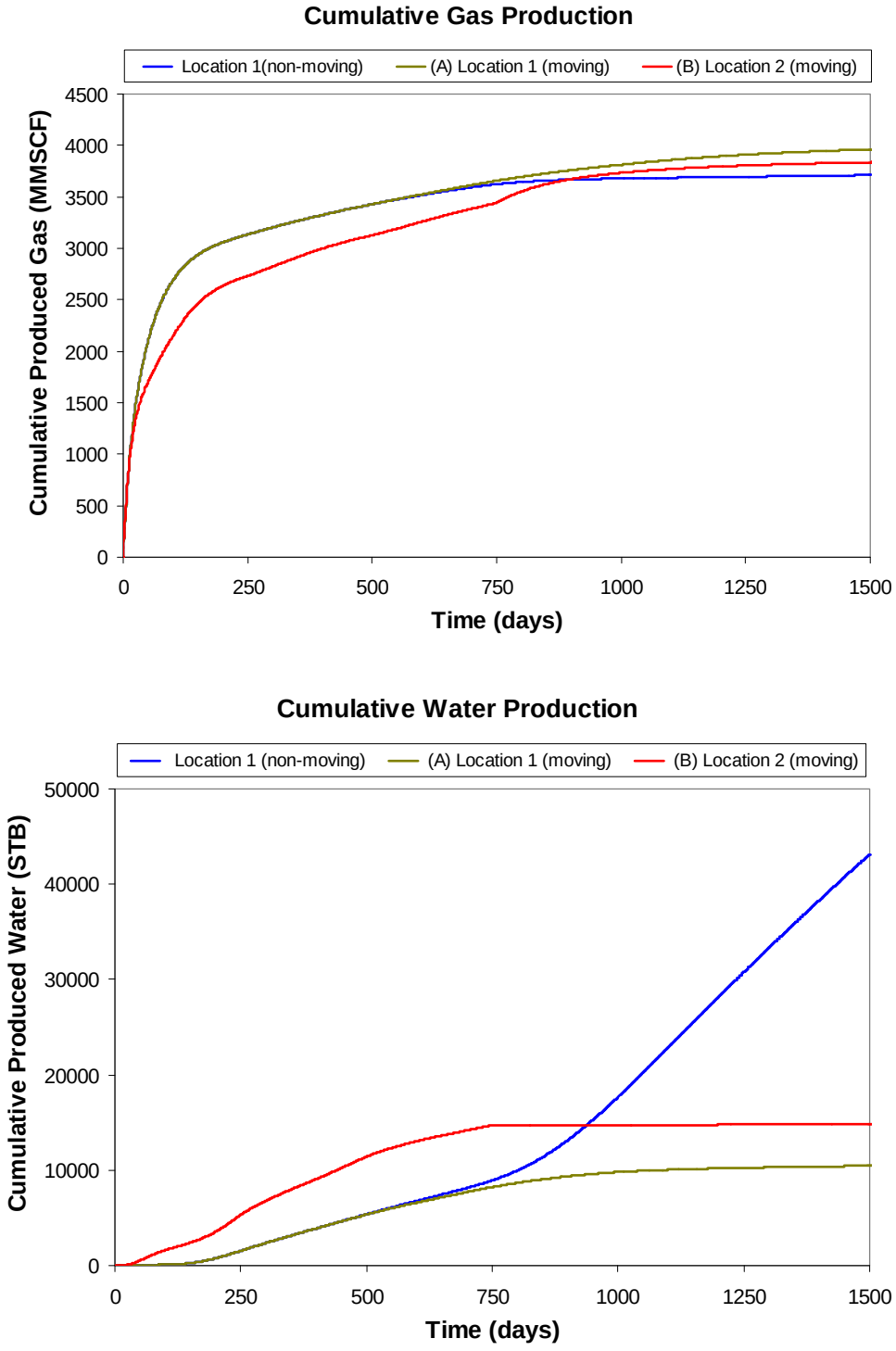

Figure 6-25: Gas and water productions of Cases 1 and 2

As a result, Case B yields higher water production and lower gas production than the completion location in Case A as shown in Figure 6-25.

It can be concluded from this examination that one should not complete a well in the hydrate zone because permeability in this zone is significantly lower than the permeability in free-gas zone. The simulation results show that a moving well-completion location strategy yields better gas production performance than a fixed well-completion location strategy. Completing a production well in the middle of free-gas zone with a moving completion location strategy yields the best gas production performance.

6.5.3 Effect of Well Spacing/or Well Drainage Area

In this section, the effect of well spacing on the production performances from a class 1 methane-hydrate reservoir shown in Figure 6-26 is examined. There are a number of production wells in this system. Considering a well located in a gray square in Figure 6-26, the interferences from the production wells surrounding this well causes the no flow boundary around the center well (dash line in Figure 6-26). Due to the symmetry of the reservoir, each portion (square area) has the same pressure, temperature, and saturation distributions at any time. Therefore, the simulation study of the entire system can be performed by studying only one unit (gray square) of the reservoir.

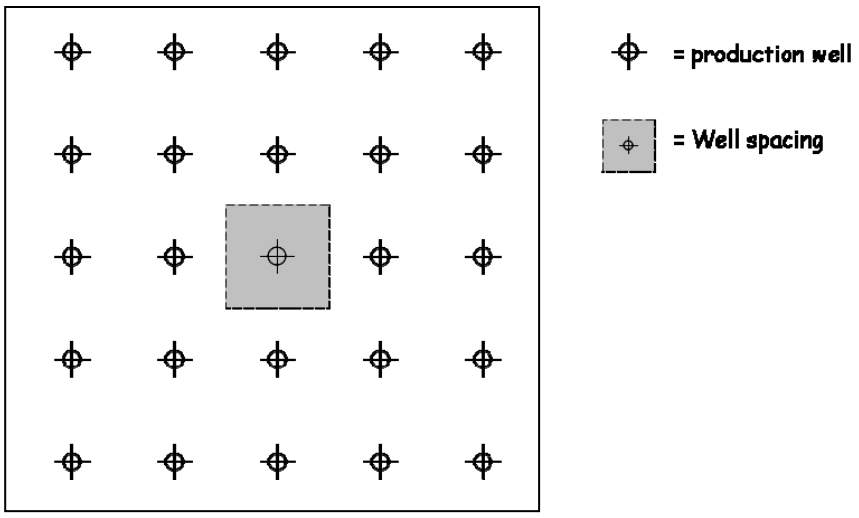

Figure 6-26: System configuration of the production characteristics study

In this study, the production well is operated at a constant bottom-hole pressure at 14.7 psia. The production characteristics of a reservoir using three different well-drainage areas are examined. The gas production rate and cumulative produced gas from one well for different well-spacing systems are shown in Figure 6-27. Figure 6-28 shows the cumulative dissociated gas and percent hydrate recovery for the three different systems.

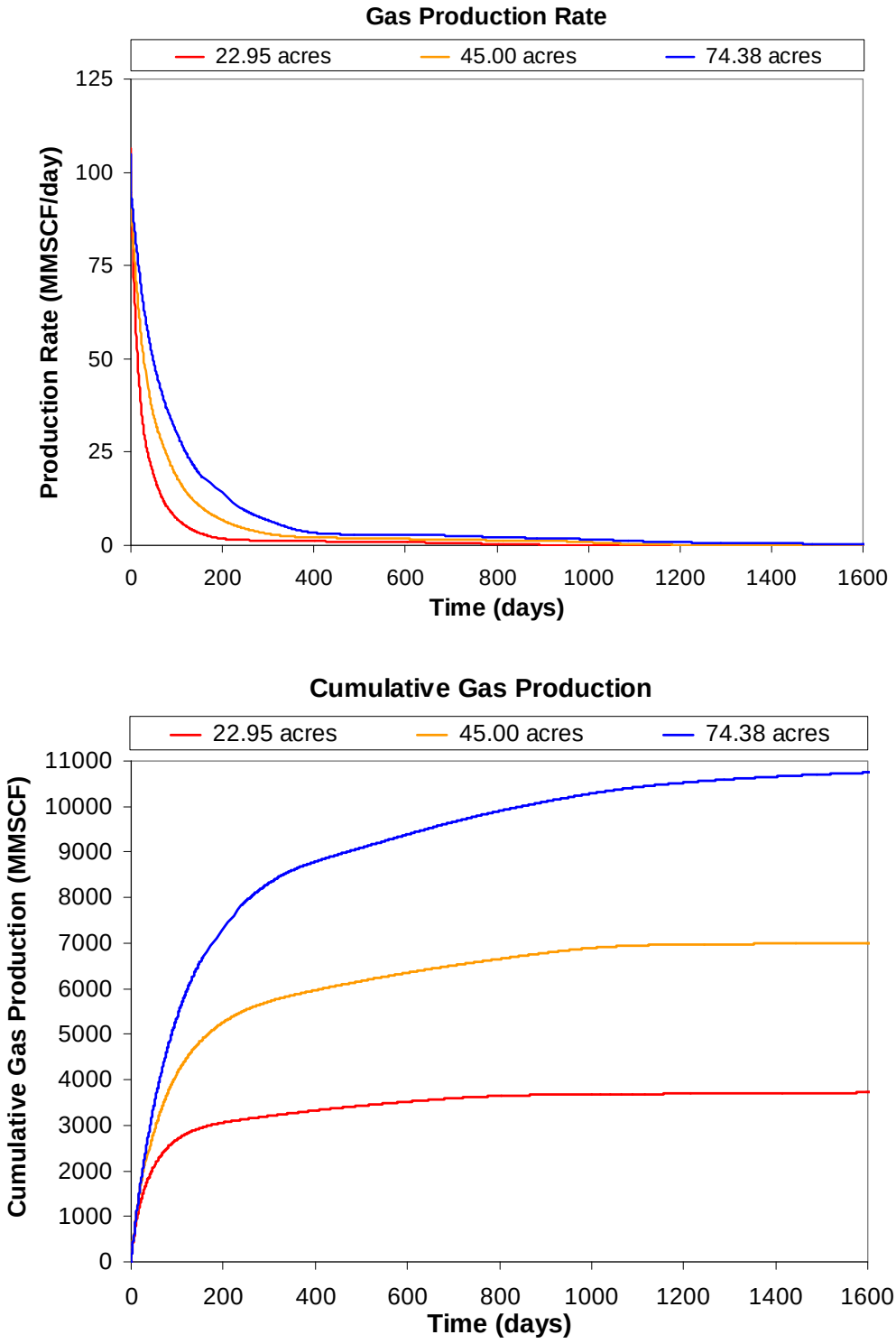

Figure 6-27: Gas production from one well for different well-spacing systems

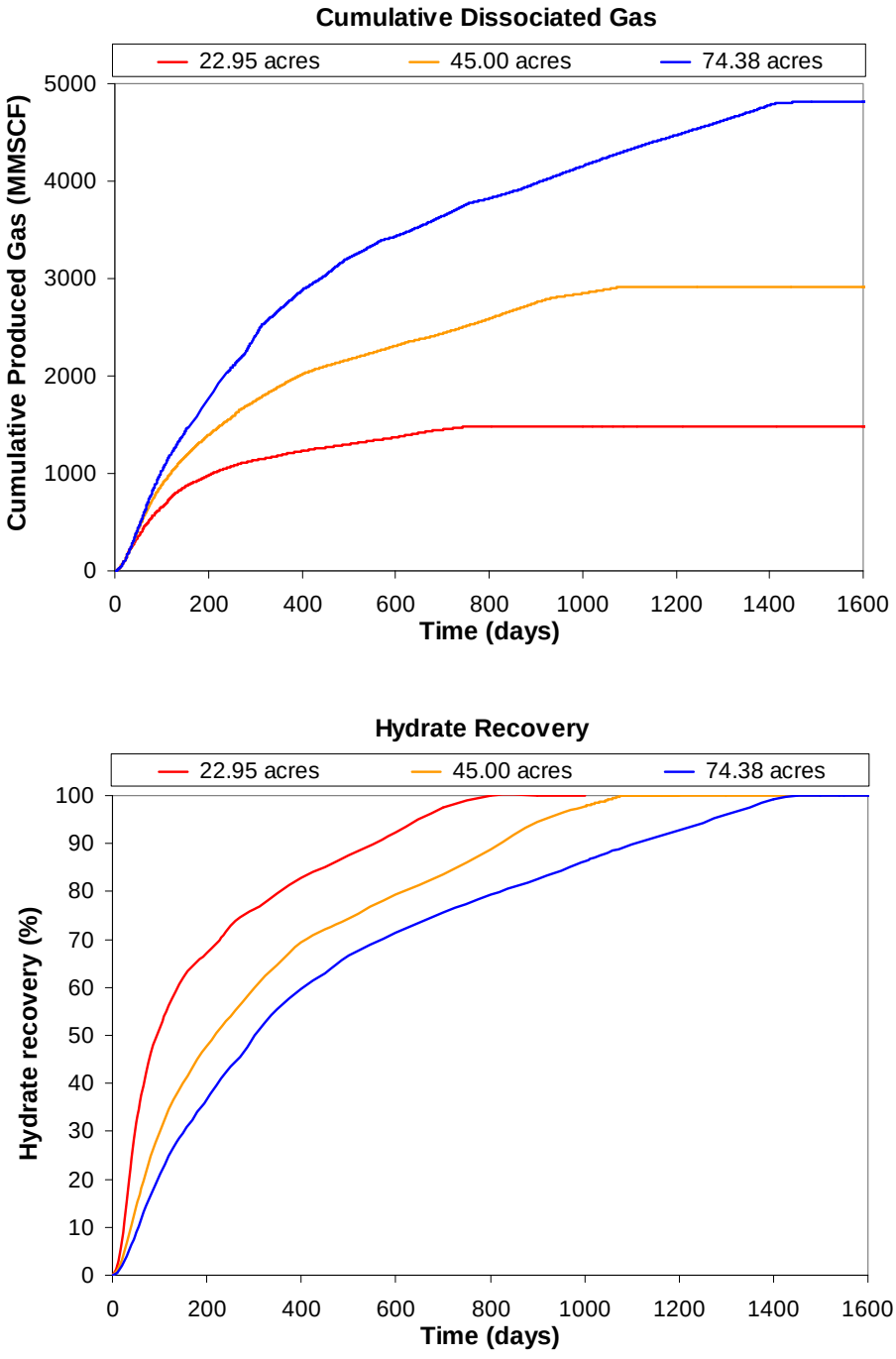

Figure 6-28: Cumulative dissociated gas and percent hydrate recovery for different well-spacing systems

During the very early production period, the cumulative gas production lines from the three systems are the same because the pressure transient has not reached the boundary of the system. The cumulative gas production line of the smallest well spacing system (22.95 acre) deviates from the cumulative gas production lines of the other two systems indicating the effect of the system boundaries on the gas production. The deviation of the cumulative gas production lines of the other two systems happen later because the pressure transient takes more time to reach the boundary of the 45-acre system. The plots of cumulative dissociated gas show the same characteristics.

The gas production rate (from one well) of the larger well-drainage area is higher because the amount of gas and methane hydrate available is higher. Thus, the cumulative produced gas (from one well) of the larger well-spacing system is higher. The results indicate that the smaller well-spacing system requires less time to dissociate 100 percent of methane-hydrate. From this simulation study, it required approximately 750, 1,080, and 1,540 days to dissociate 100 percent of methane hydrate for the 22.95, 45.00, and 74.38 acres of well spacing systems, respectively. Figure 6-29 shows percent hydrate recovery of the three systems at 750 and 1,080 days.

In order to compare the production efficiency of these three systems, the system must have the same drainage area. In this comparison, the cumulative gas production and hydrate recovery from a 450-acre reservoir using these three different well spacings are investigated. In this case, the number of production wells for the 22.95, 45.00, and 74.83 acre well-spacing systems are approximately 20, 10, and 6, respectively. The cumulative produced gas and hydrate recovery of the three cases for this reservoir are shown in Figure 6-30.

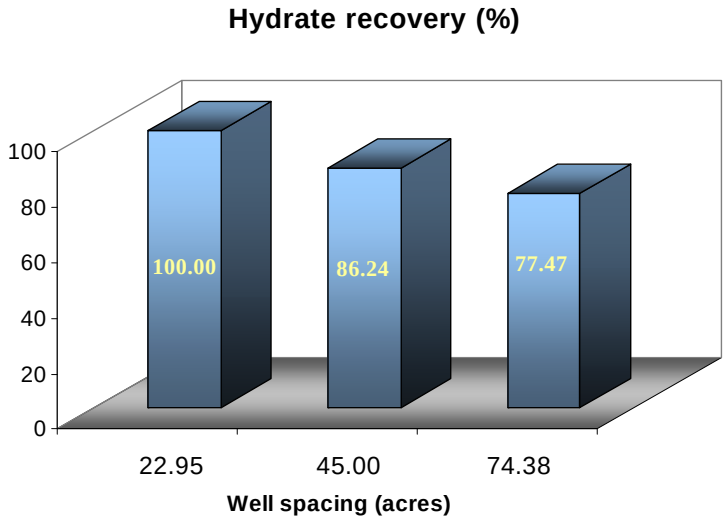

(a) Hydrate recovery of different well spacing systems at 750 days

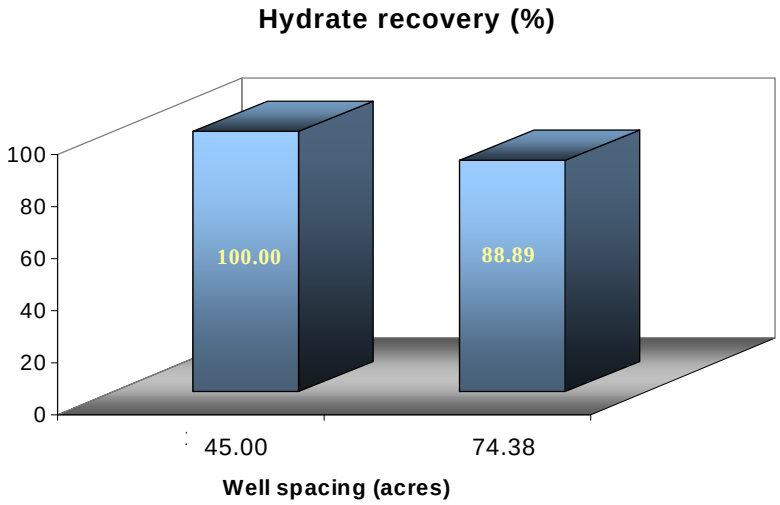

(b) Hydrate recovery of different well spacing systems at 1,080 days

Figure 6-29: Hydrate recovery of different well-spacing at 750 and 1,080 days

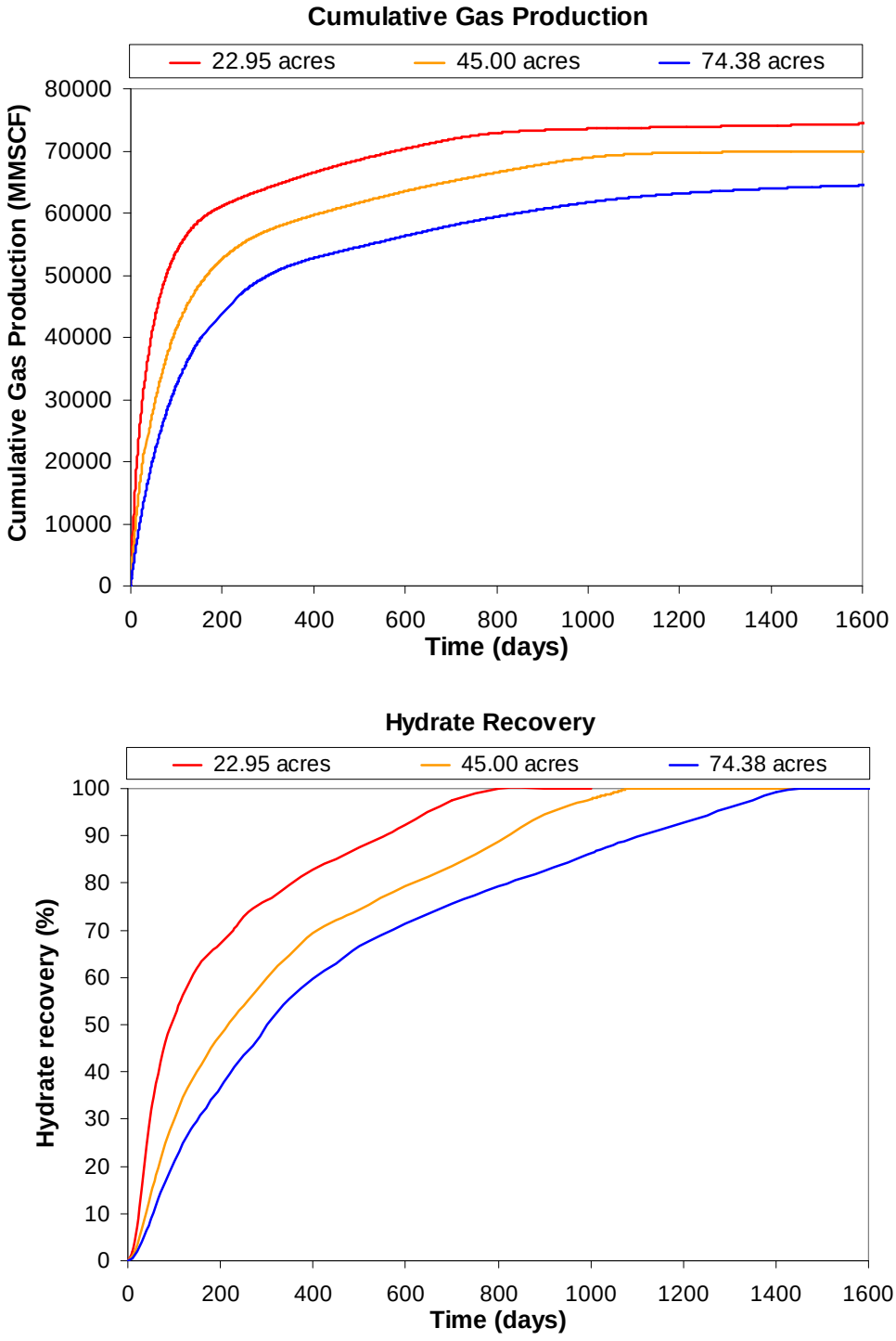

Figure 6-30: Cumulative gas production and hydrate recovery of the three different well spacings for a 450 acre reservoir

As expected, the smaller well spacing system yields higher cumulative produced gas and faster hydrate dissociation. This indicates that the gas production performance and hydrate recovery efficiency can be improved by increasing the number of wells in the system (or reduce well spacing). However, increasing the number of wells require higher investment. The cumulative produced gases (at the end of 1,600 days of operation) of the three cases are shown in Table 6-19. Note that in this simulation study, the gas production rates of all cases become very small at the end of 1,600 days of production indicating that the ultimate cumulative gas productions of the three cases do not significantly differ from the values shown in Table 6-19.

Table 6-19: Cumulative produced gases for three different well spacings

Well spacing (acres)	Number of well	Gas Production (MMSCF)	Improvement (%)
22.95	20	74365	15.34
45.00	10	69891	8.40
74.38*	6	64474	0.00

* Reference case

Note that the values shown in Table 6-19 may change from one system to the other system. Therefore, these values shall not provide the accurate optimum well spacing for systems different from the one studied in this work.

6.5.4 Implementation of a Different Production Schedule

The production performances from a methane-hydrate reservoir with 4 production wells as shown in Figure 6-31 using four different production schedules are examined in this section. All production wells are operated at 14.7 psia (constant bottom-hole pressure scheme) but they are put on production at different times. Four different production schedules shown in Table 6-20 are examined in this study.

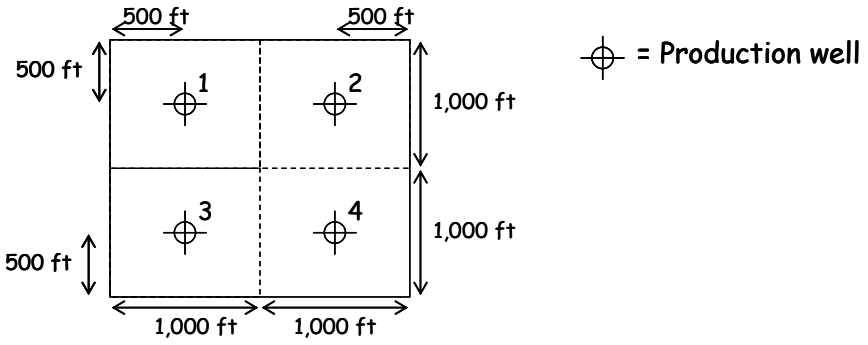

Figure 6-31: Well structure in the methane-hydrate reservoir used in this study

Table 6-20: Production schedules used in this study

Case	Starting time of operation (days)			
	well no.1	well no.2	well no.3	well no.4
a	t = 0	t = 0	t = 0	t = 0
b	t = 0	t = 90	t = 90	t = 180
c	t = 0	t = 60	t = 60	t = 180
d	t = 0	t = 90	t = 90	t = 0

Figure 6-32 shows the percent methane-hydrate recovery and cumulative dissociated gas for each of these four production schedules and the plots of gas and water productions for these cases are shown in Figures 6-33 and 6-34, respectively.

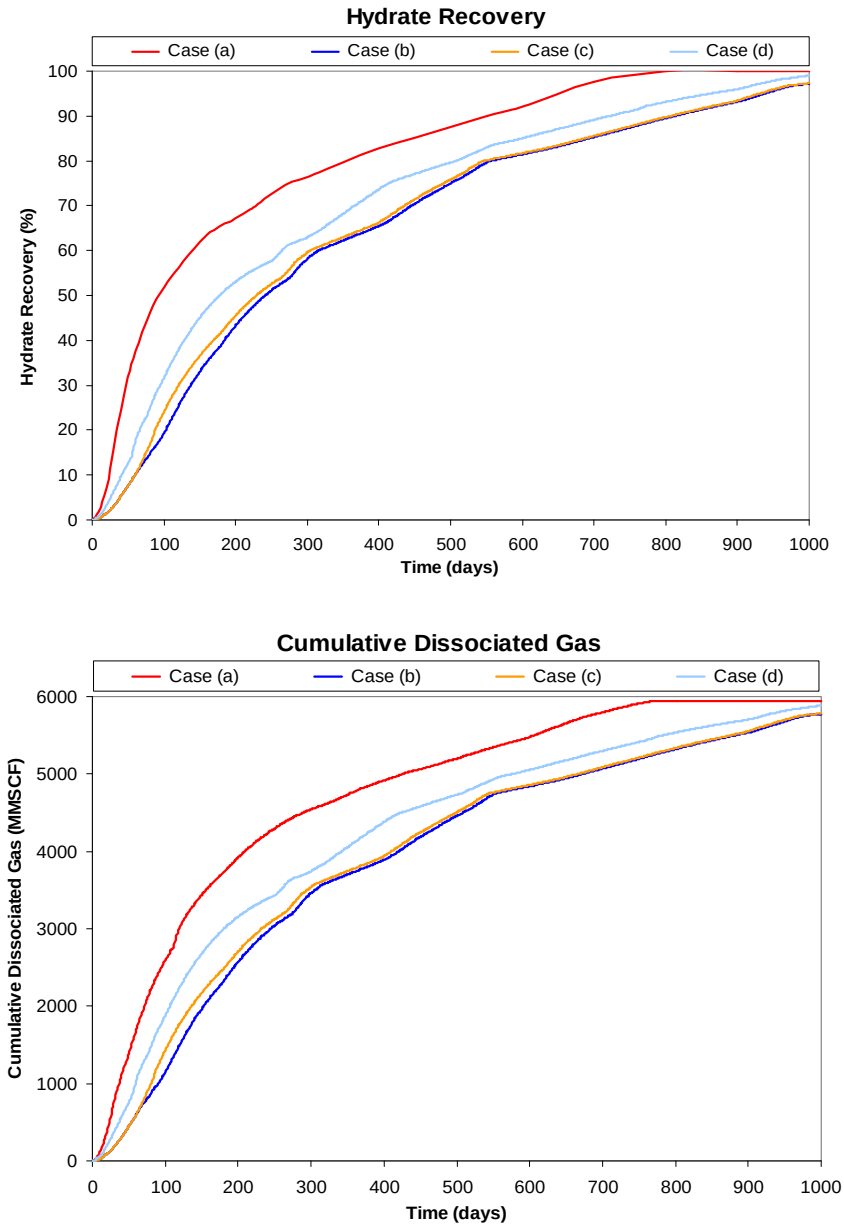

Figure 6-32: Hydrate recovery and cumulative dissociated gas for each case

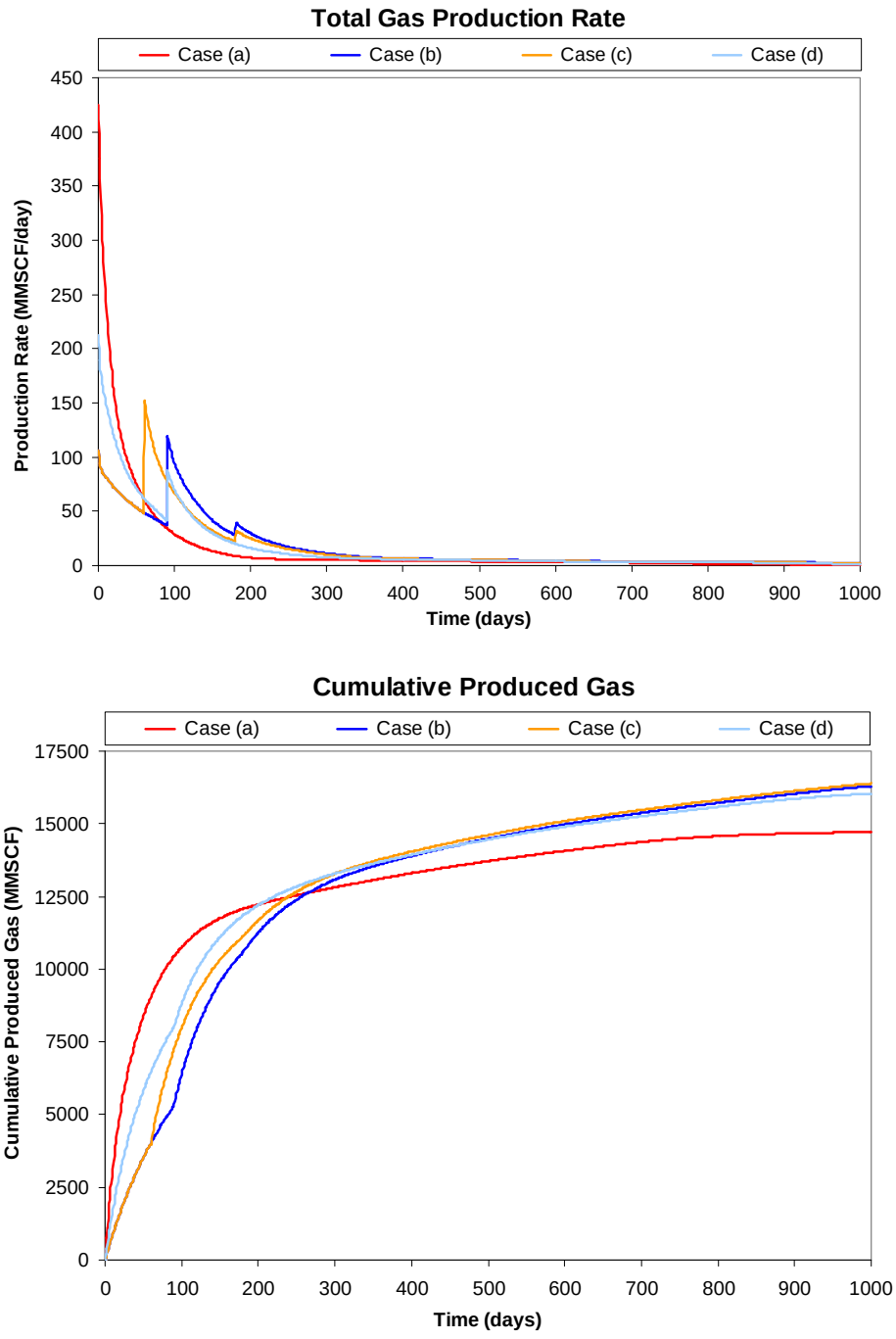

Figure 6-33: Gas production of different production schedules

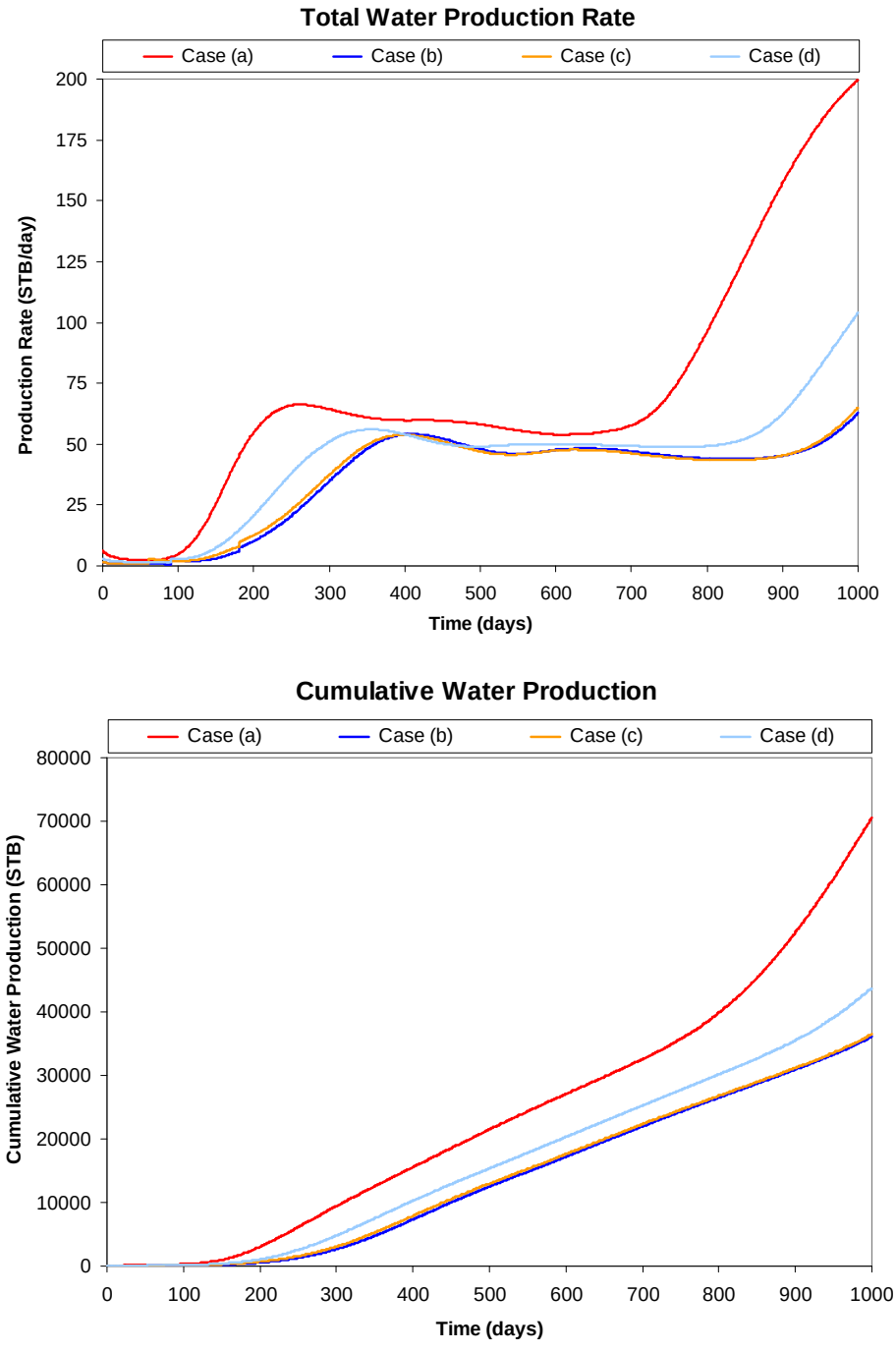

Figure 6-34: Water production of different production schedules

The results show that Case (a) can dissociate 100 percent of methane-hydrate earlier than the other four cases providing the higher cumulative dissociated gas in Case (a). On the other hand, the cumulative gas production of Case (a) is lower than the cumulative gas productions of Cases (b), (c), and (d). As shown in Figure 6-34, the cumulative production and production rate of water in Case (a) is higher than that of the other cases.

The plots of water saturation of the well blocks for these four cases are shown in Figure 6-35. The increase of water saturation at the well blocks in Case (a) is higher than that in the other cases resulting in the higher increase of water production rate in Case (a). The change of aqueous phase saturation for these cases can be explained by the discussion of the saturation change in section 6.5.1 because the shapes of the water saturation plots shown in Figure 6-35 are similar to the shape of the saturation plot in Figure 6-17 (b).

For Case (a), the changes of aqueous phase saturations at each well block are the same because of the system's symmetry (the system can be symmetrically divided into 4 parts). According to Figures 6-32 and 6-35, methane hydrate can be dissociated more rapidly in Case (a) because all the production wells are put on production at the beginning of the operation. Consequently, more water is released (from hydrate dissociation) into the system in this case resulting in the higher (and sooner) increase of aqueous phase saturations as shown in Figure 6-35. Thus, water production rate in Case (a) is the highest. On the other hand, higher increase of aqueous phase saturation implies higher decrease for free-gas phase saturation. Hence, the mobility of free-gas phase in Case (a) more rapidly decreases than the other cases. Therefore, the gas production rate in

Case (a) drops more rapidly than the production rate in the other cases resulting in a lower gas production in Case (a).

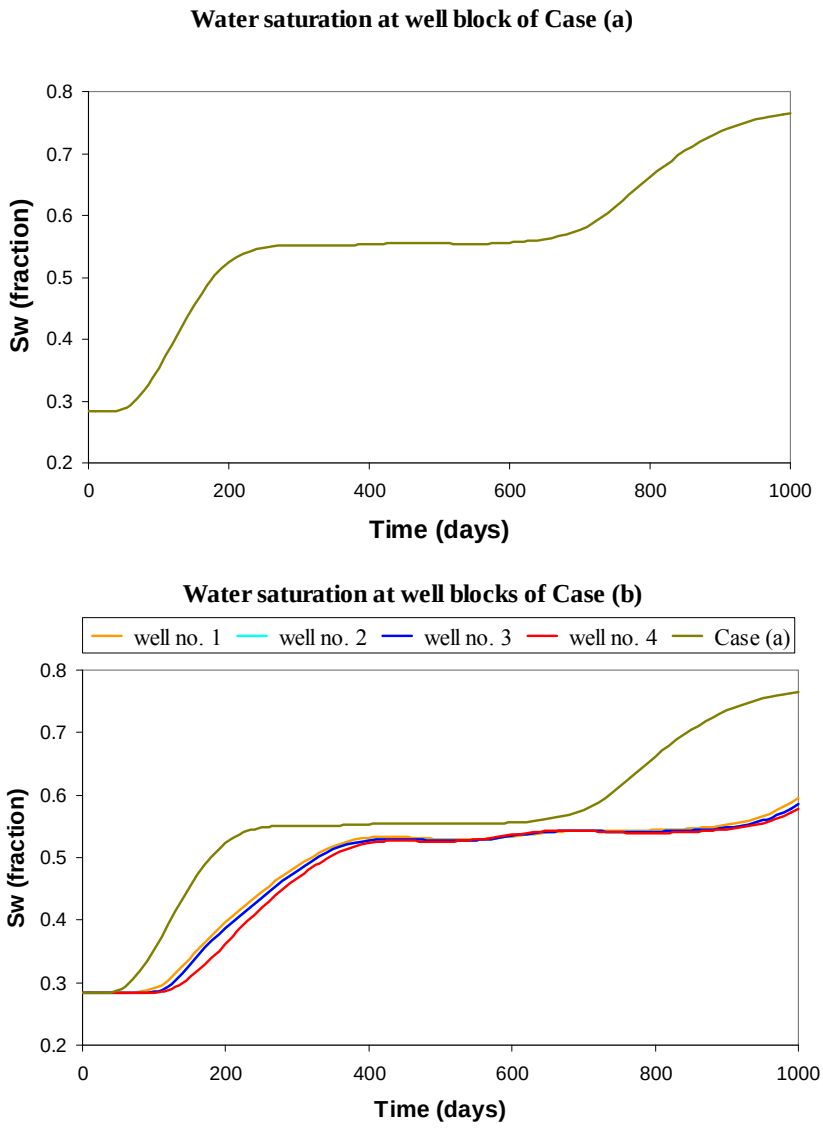

Figure 6-35: Aqueous phase saturation of the well blocks for different production schedules

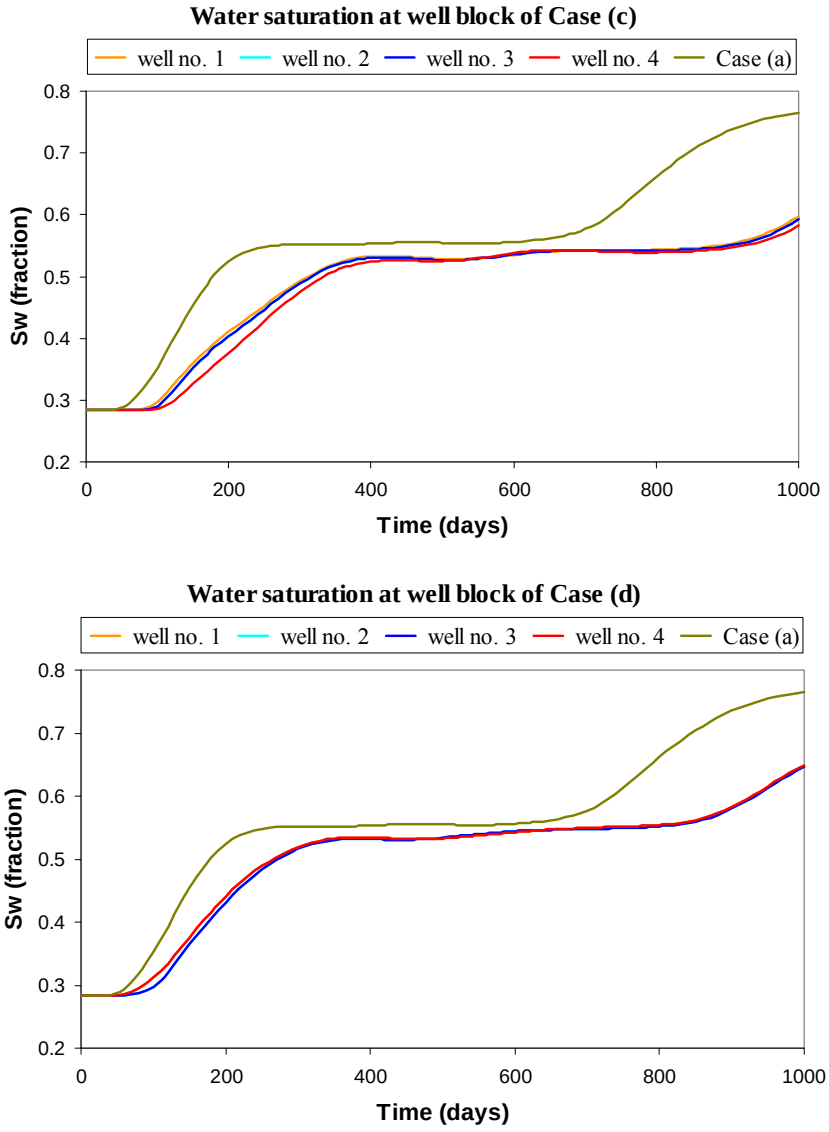

Figure 6-35 (cont.): Aqueous phase saturation of the well blocks for different production schedules

Among the remaining cases (Cases b, c, and d), the hydrate dissociation rate in Case (d) is higher than that in the other two cases. As a result, the water production in this case is higher whereas the gas production is lower than those in the other two cases.

Hydrate dissociation rate in cases (b) and (c) are slightly different. Therefore, gas and water production from these two cases are not significantly different. The plots of water saturation distribution on the well block layer (on the *x*-*y* plane) at various times for these four production schedules are shown in Figure 6-36 to Figure 6-39.

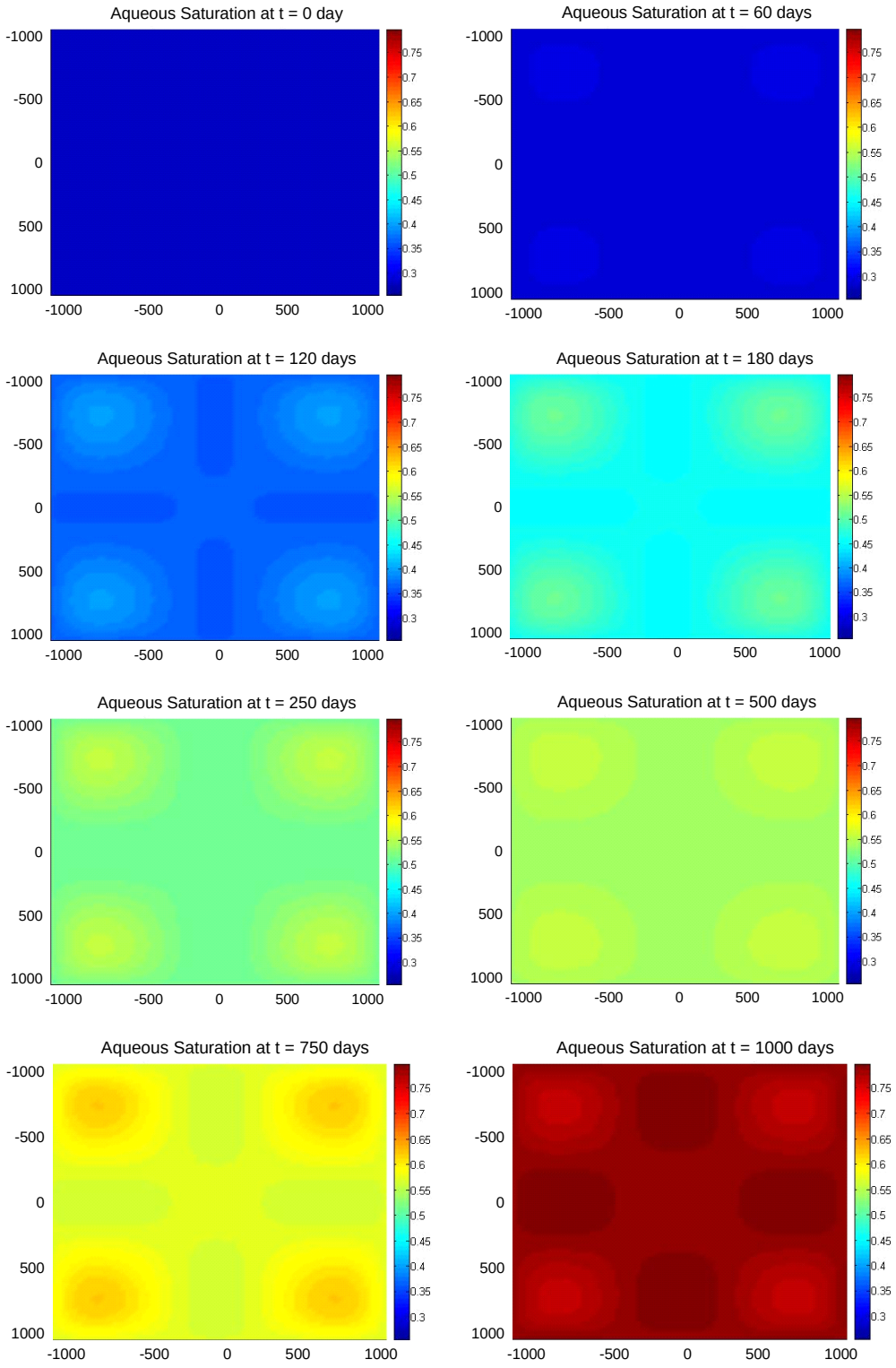

Figure 6-36: Aqueous phase saturation of well block layer for Case (a)

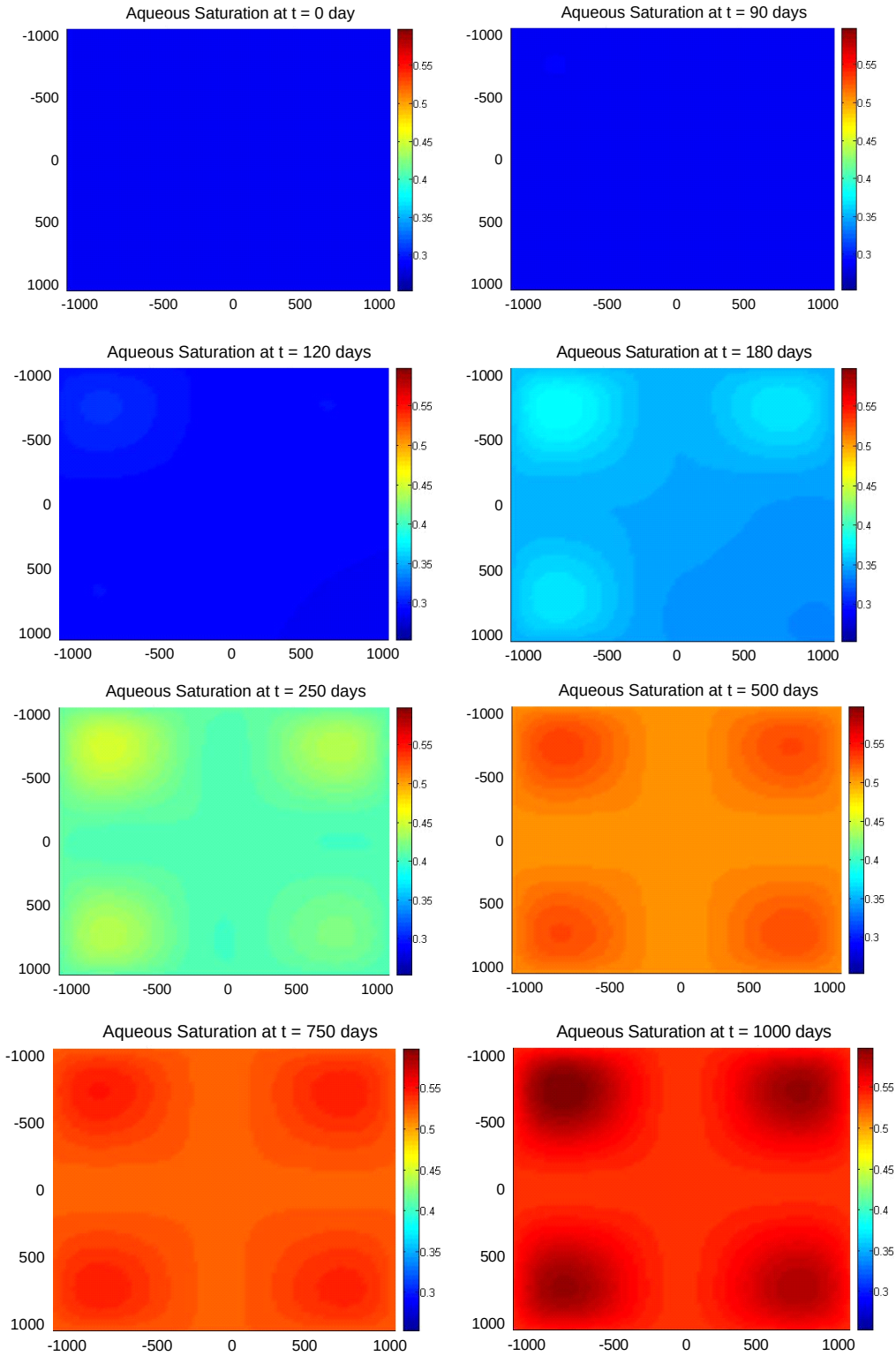

Figure 6-37: Aqueous phase saturation of well block layer for Case (b)

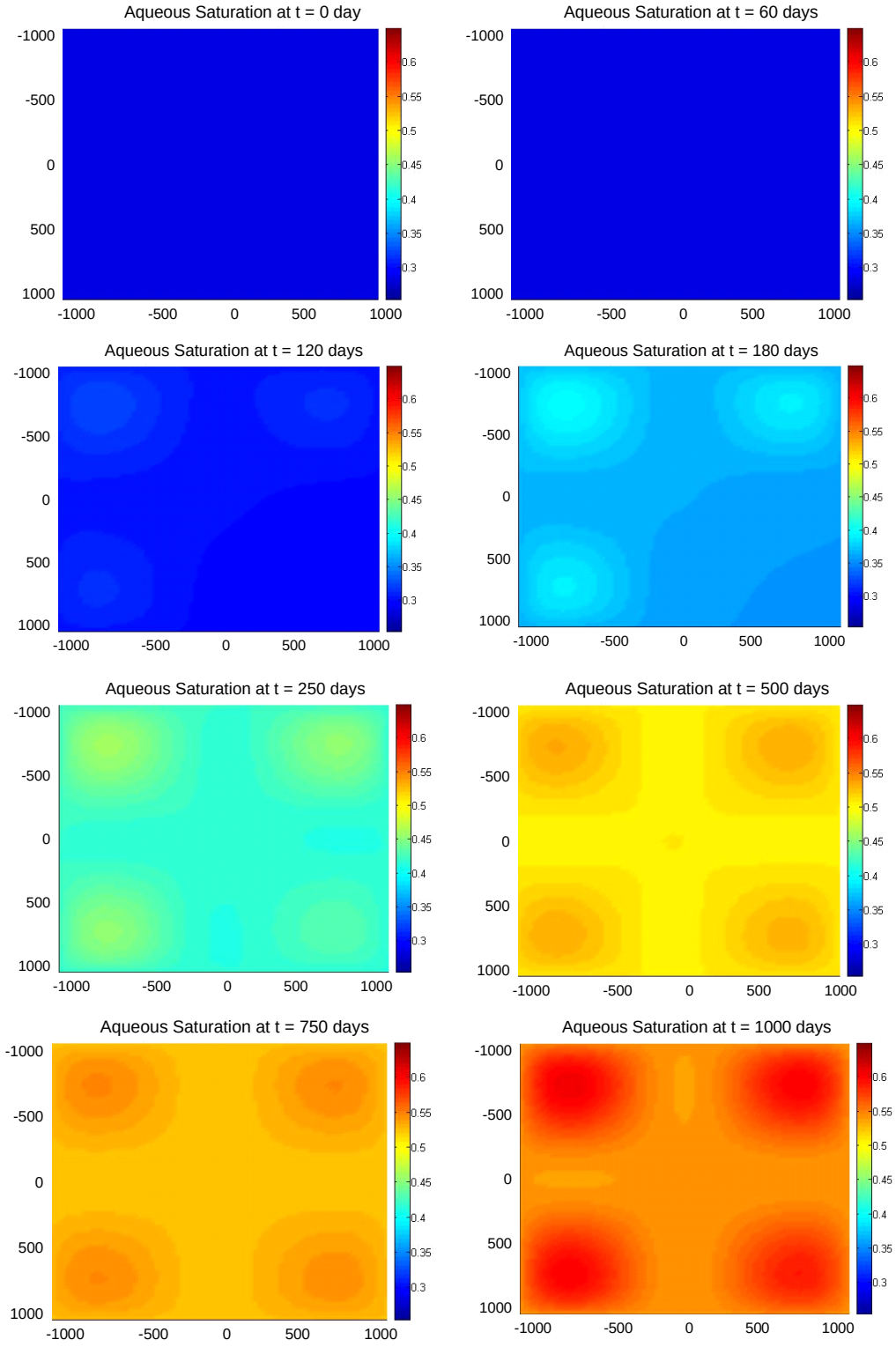

Figure 6-38: Aqueous phase saturation of well block layer for Case (c)

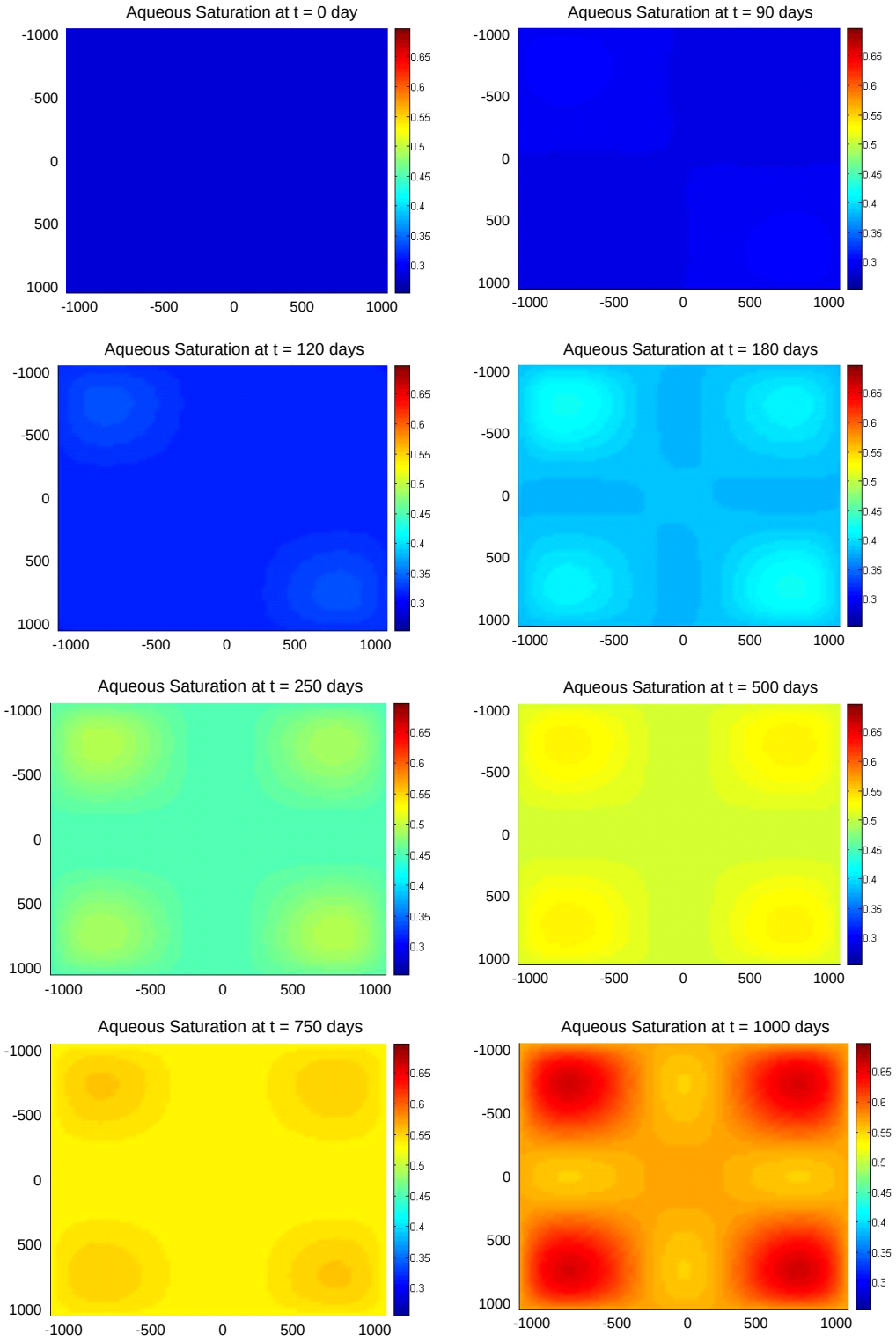

Figure 6-39: Aqueous phase saturation of well block layer for Case (d)

Figure 6-40 to Figure 6-43 show hydrate saturation distribution of the initial dissociation front layer (layer no. 9 in Table 6-17) at various times for the four production schedules. As expected, Case (a) requires less time (160 days) than the other cases for dissociating all the hydrate phase in the initial dissociation front layer because all the wells are operated at the same time. Case (d) requires less time (270 days) than the other two remaining cases because two wells are put on production at t = 0 and Cases (b) and (c) need approximately the same amount of time (300 days) for dissociating all the hydrate phase in the initial dissociation front layer.

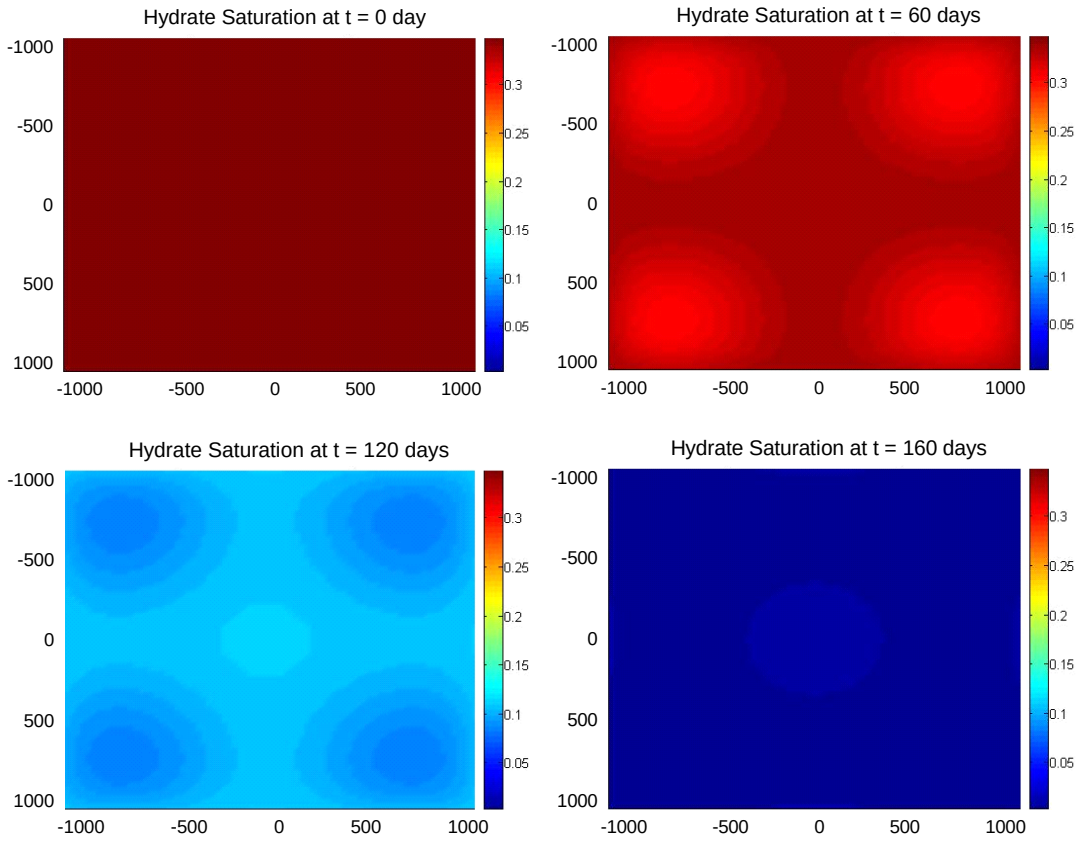

Figure 6-40: Hydrate saturation of the initial dissociation front layer for Case (a)

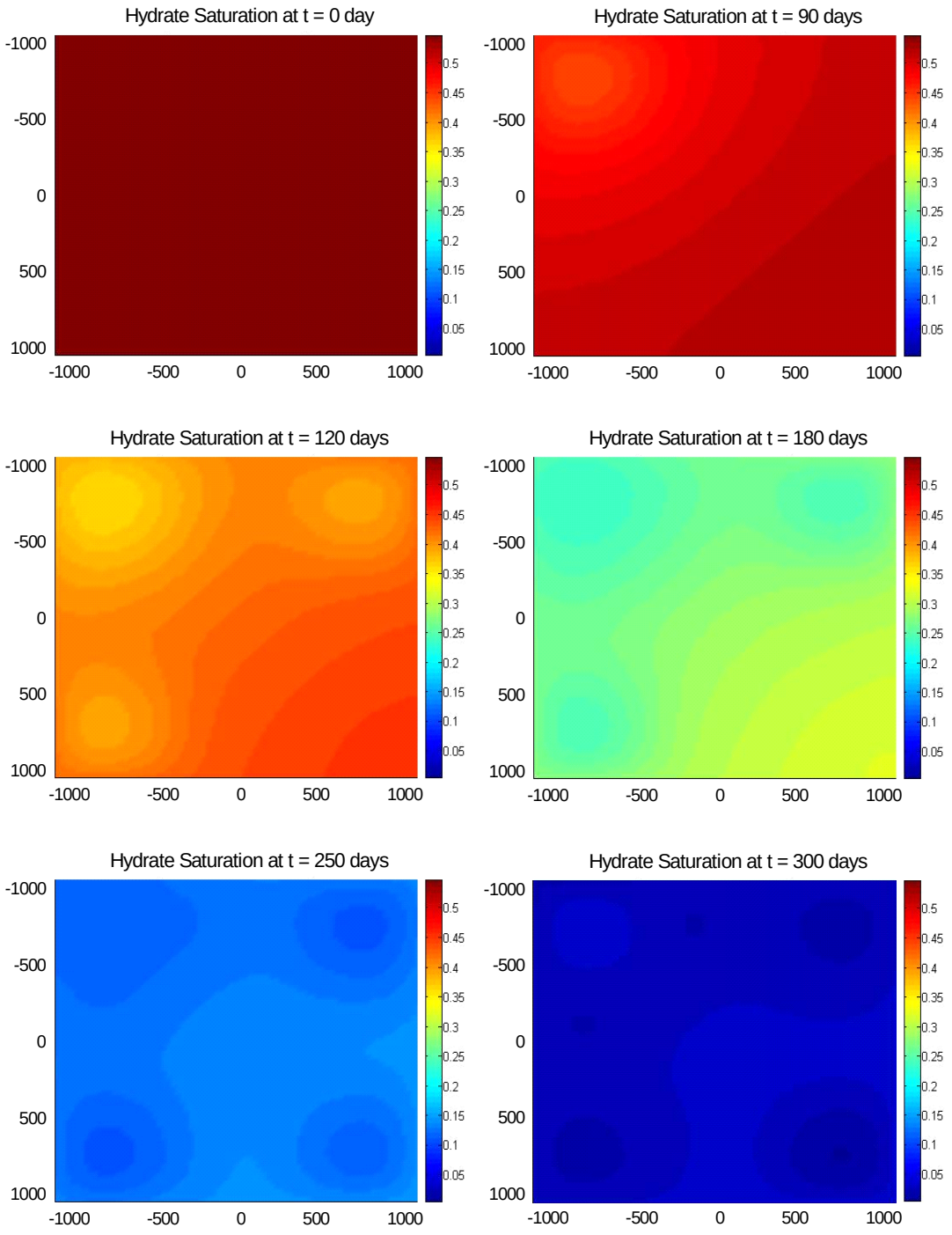

Figure 6-41: Hydrate saturation of the initial dissociation front layer for Case (b)

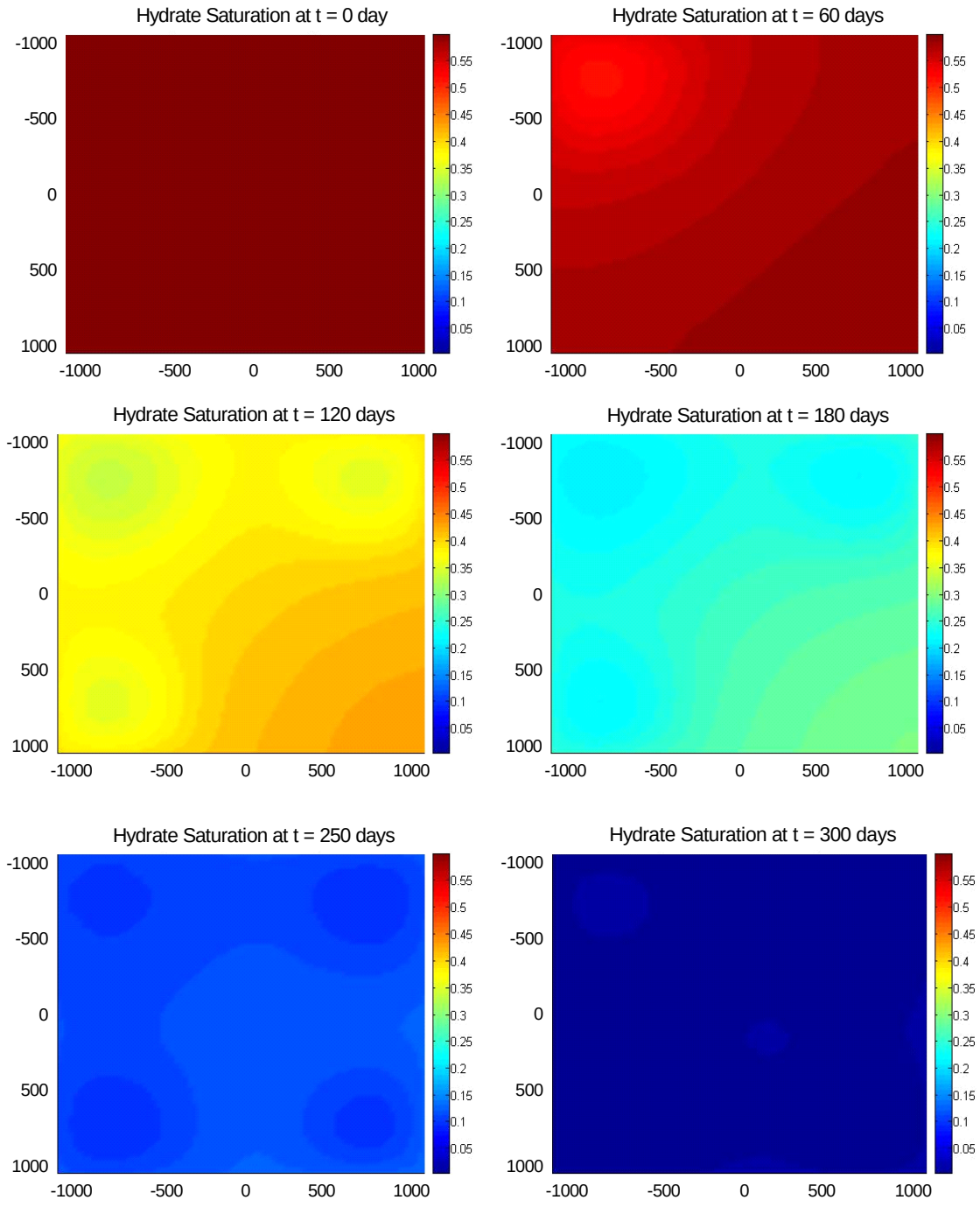

Figure 6-42: Hydrate saturation of the initial dissociation front layer for Case (c)

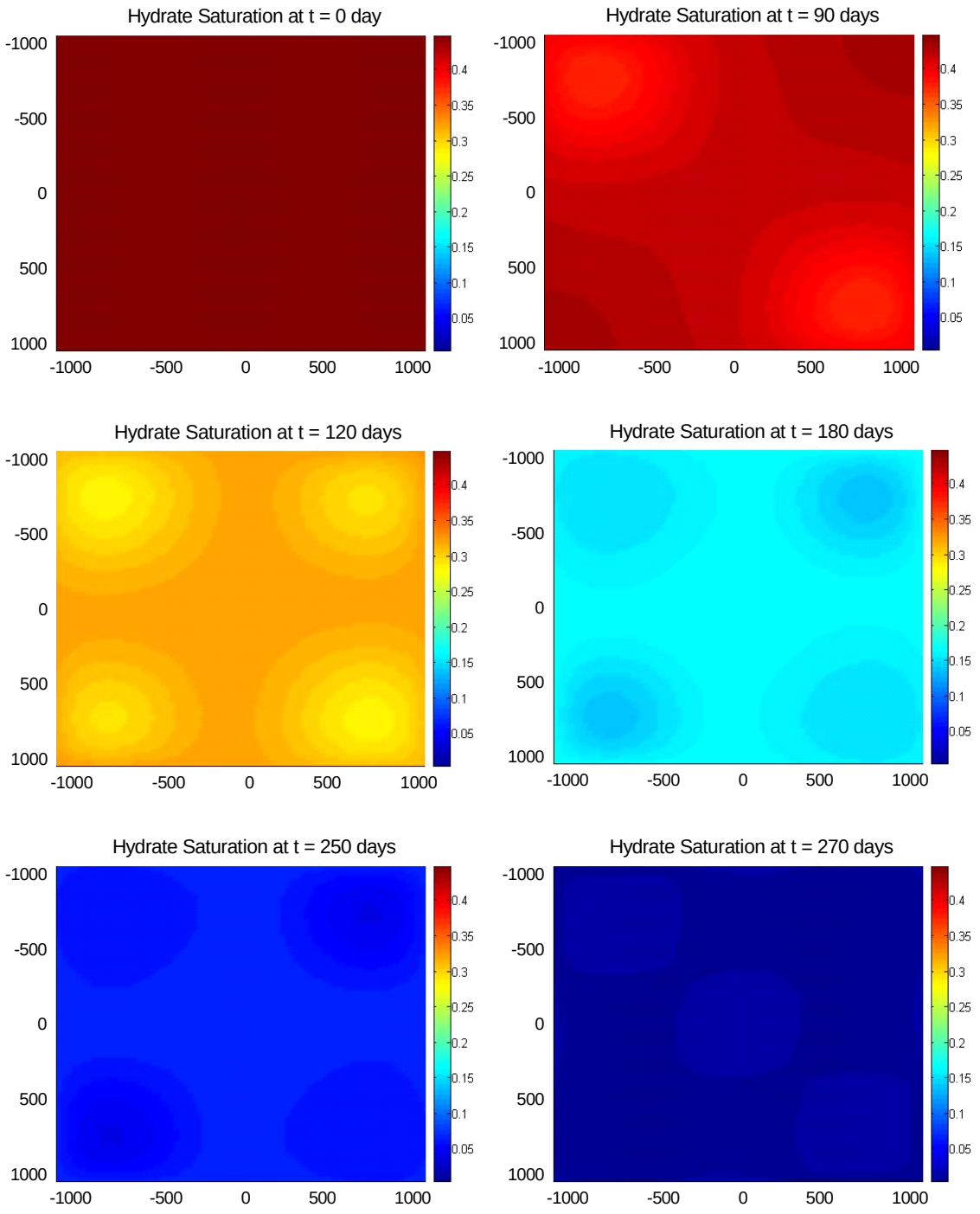

Figure 6-43: Hydrate saturation of the initial dissociation front layer for Case (d)

Figure 6-44 shows the gas to water ratio and the cumulative gas to water ratio for these four cases. The gas to water ratio is calculated by dividing total gas production rate by total water production rate at any particular time. Similarly, the cumulative gas to water ratio is the ratio of the total cumulative gas production to the total cumulative water production. They represent the amount of produced gas per unit volume of produced water which means that the higher value is preferred.

Both gas to water and cumulative gas to water ratios for Case (a) decrease more rapidly than the ratios for the other cases because of the higher increase of water production rate and decrease of gas production rate as previously discussed, meanwhile the ratios for Cases (b) and (c) are higher than the other two cases, and the ratios for Case (b) is a bit higher than the ratio for Case (c). The cumulative gas to water ratio (MMSCF/STB) and cumulative produced gas (MMSCF) at the end of 1,000 days for the four cases are shown in Table 6-21.

The results indicate that the ratio for Case (b) is the highest among the four cases and it shows that the ratio could improve 119 percent by delaying the operation of production wells. However, the cumulative gas production in Case (b) is higher than that of Case (a) just about 10.8 percent, not 119 percent. This is because the cumulative water production in Case (a) is higher than that of Case (b). When considering about the cumulative gas production, Case (c) represents the best production schedule among the four cases examined.

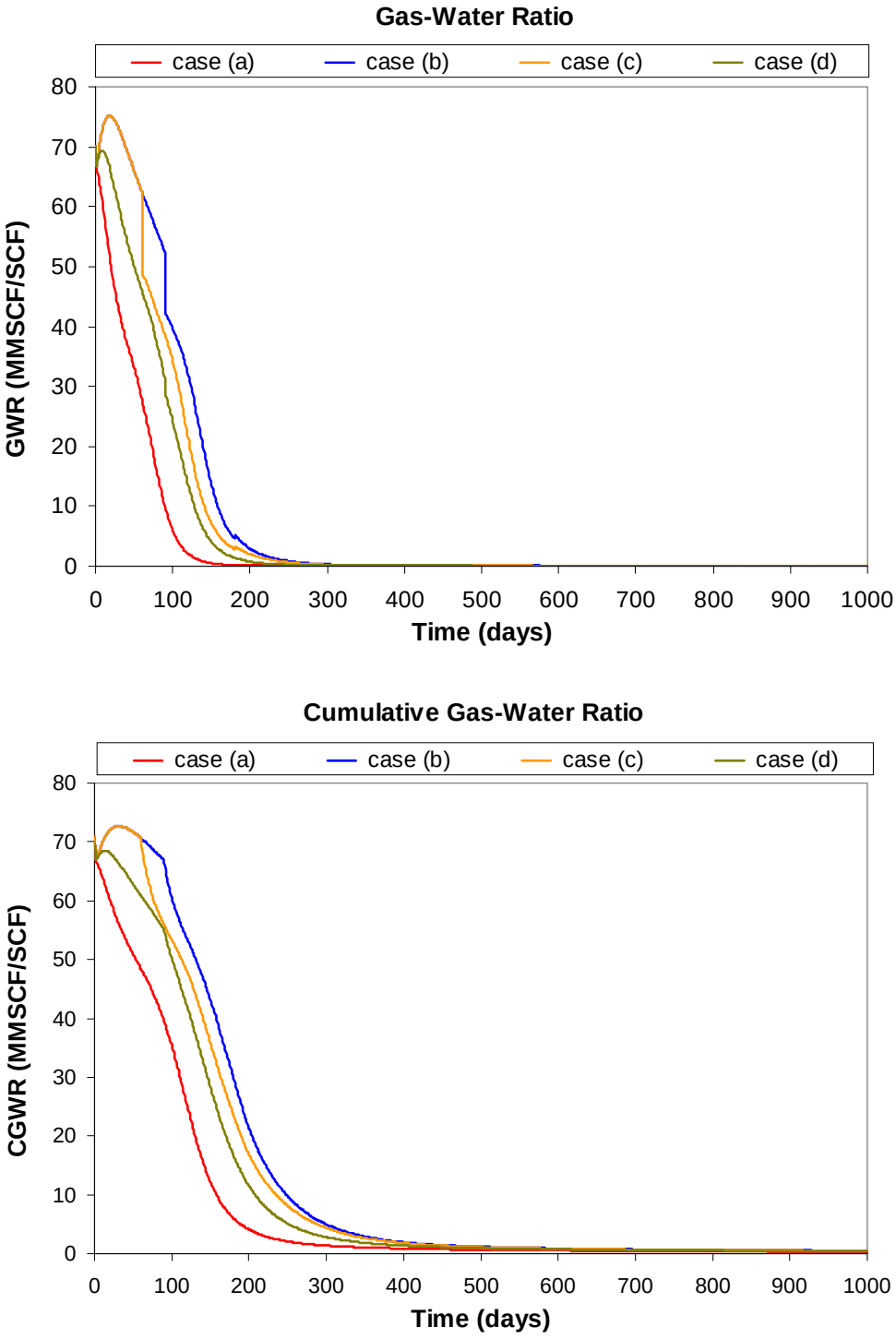

Figure 6-44: Gas to water ratio for different production schedules

Table 6-21: Cumulative Gas to Water Ratio at 1,000 days for each case

Case	Ratio		Amount	
	CGWR	% Improvement	Qg	% Improvement
a*	0.208	0.0	14714	0.0
b	0.456	119.0	16297	10.8
c	0.449	115.6	16383	11.3
d	0.367	75.9	16040	9.0

* Reference case

The percent hydrate recovery, cumulative gas production, and cumulative gas to water ratio obtained from this simulation study indicate that Cases (b) and (c) are the best production schemes (the production efficiencies of these two cases are not significantly different) among the four cases. They yield higher gas production even though less hydrate is dissociated in the system and as thereby leaving still more hydrate to be recovered.

The results shows that lowering hydrate dissociation rate by putting production wells on production at different times yields better production efficiency. However, as shown in section 6.5.3, lowering the hydrate dissociation rate by reducing number of production wells in the system should not necessarily improve production efficiency. The following simulation exercise has been performed to verify this observation. The two different production strategies for the system shown in Figure 6-31 are investigated. In Case 1, all wells are put on production at the same time whereas only wells no. 1 and 4 are put on production (at the same time) in Case 2. The plots of percent hydrate recovery and cumulative produced gas of these two cases are shown in Figure 6-45.

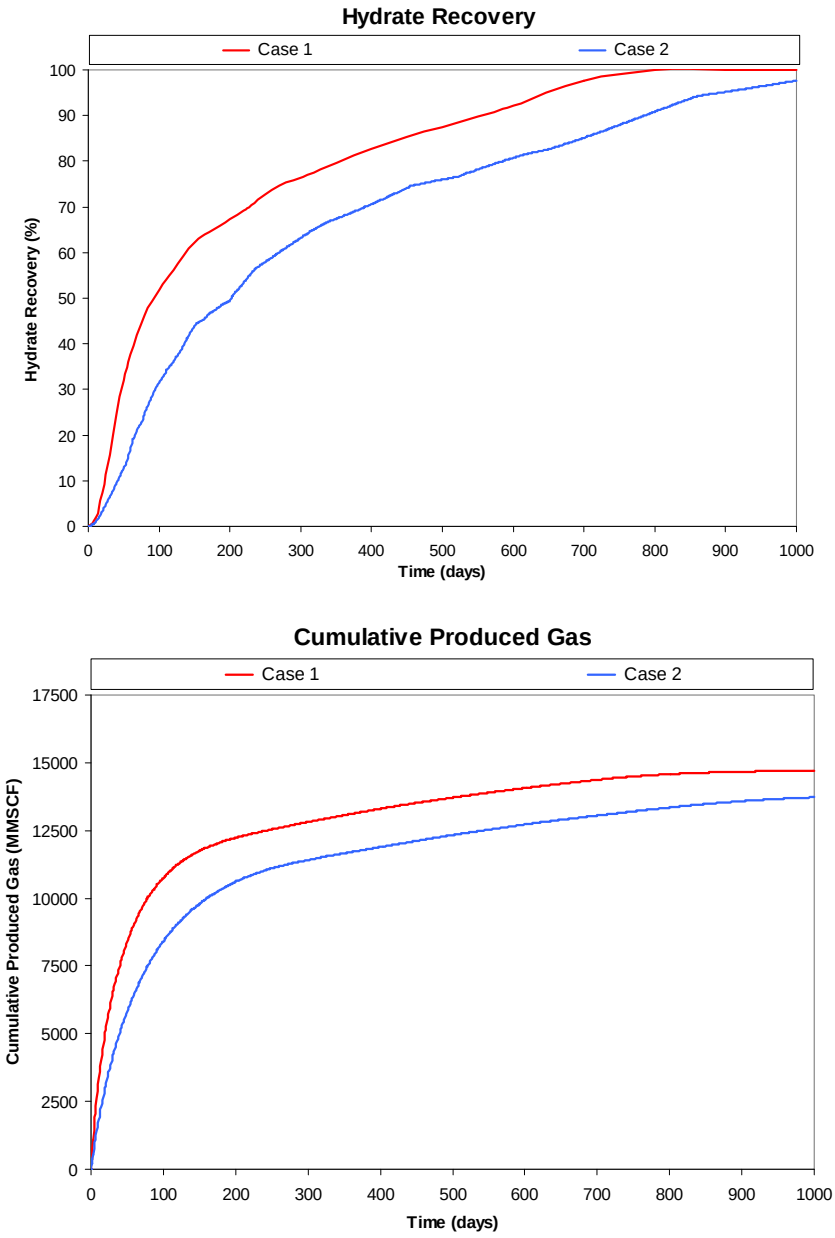

Figure 6-45: Hydrate recovery and cumulative produced gas of Cases 1 and 2.

As expected, Case 2 provides lower dissociation rate (lower hydrate recovery) than Case 1, and the cumulative gas production at the end of 1,000 days of Case 1 (14,714 MMSCF) is higher than the cumulative gas production at the end of 1,000 days of Case 2 (13,729 MMSCF) by about 7.17 percent.

From this simulation study, it could be concluded that in a multiple-well system, putting every well on production at the same time yields the higher dissociation rate but it would result in lower gas production. Putting the wells on production at different times reduces hydrate dissociation rate but it seems to improve the recovery efficiency. Decreasing hydrate dissociation rate by reducing the number of production wells does not improve gas production efficiency.

CHAPTER 7

SUMMARY AND CONCLUSIONS

A three-dimensional, rectangular, compositional simulator for methane-hydrate system has been developed to examine the production characteristics from methane-hydrate reservoirs. The model accounts for heat transfer due to conduction and convection processes. The effects of hydrate saturation on formation permeability and capillary pressure between free-gas and aqueous phases are also taken into account. The study focuses on the production characteristics (by conventional depressurization technique) from Class 1 methane-hydrate reservoirs. In this study, the constant bottom-hole pressure production scheme is examined. The production performances of different production strategies are investigated. The following observations on the production characteristics of Class 1 methane-hydrate reservoirs have been derived from this work:

- Unlike conventional gas reservoirs in which both gas and water production rates exponentially decline with time when the well is operated at a constant bottom-hole pressure, gas production rate exponentially decreases with time meanwhile water production rate increases with time for gas-hydrate reservoirs. Because gas-hydrate dissociation releases both free-gas and aqueous phases to the system, the released aqueous phase flows down to the free-gas zone (due to the gravitational force) resulting in the increase of aqueous phase saturation in the free-gas zone. As a result, water production rate increases.

- The effect of well-completion location on gas production performance has been investigated. The moving well-completion location implementation provides better gas production performance than all the cases of fixed well-completion location strategy. Completing a production well in the middle of free-gas zone (using a moving completion location strategy) yields the best gas production performance (it provides the highest gas production and lowest water production).
- The effect of well spacing on the production efficiency was also investigated. The larger well spacing provides higher gas production per well because more gas and gas hydrate are available. However, the total gas production rate and cumulative gas production (for a specific reservoir) of the larger well-spacing system are lower than the total gas production rate and cumulative gas production of a smaller well-spacing system. This implies that, for a specific reservoir, drilling more well yields higher gas production but it requires higher investment. Based on the simulation results in this study, the cumulative gas production decreased just about 8.4 percent when the well spacing increases from 45.0 acre to 74.38 acre. This value could change depending upon the rock and fluid properties and reservoir structure.
- The effect of well scheduling in a multiple-well system on the production performance has also been examined. The simulation results show that starting all production wells at the same time provides faster hydrate dissociation. However, the more effective gas production is observed when starting production wells at different times. This is because the faster hydrate dissociation yields higher rate of water released from gas hydrate phase to the system. The released water flows

down to the free-gas zone due to the gravitational effect resulting in the increase of water saturation in the production region. Consequently, mobility of water phase increases meanwhile the mobility of free gas decreases. Therefore, the faster dissociation rate does not necessarily improve gas production efficiency. The simulation results show the improvement of gas production efficiency when the production wells are put on production at different time (which yields lower dissociation rate than the case when all wells are put on production at the same time). However, reducing hydrate dissociation rate by decreasing the number of production wells does not improve gas production efficiency.

BIBLIOGRAPHY

1. Makogon Y. and Holditch S., *"Gas Hydrates as a Resource and a Mechanism for Transmission",* SPE Paper 77334 presented at the SPE Annual Technical Conference and Exhibition held in San Antonio, Texas, 29 September-2 October (2002)
2. Moridis G.J., "*Numerical Studies of Gas Production from Methane Hydrates",* SPE Paper 75691 presented in the SPE Gas Technology Symposium held in Calgary, Alberta (2002)
3. Sloan E.D. JR, *"Clathrate Hydrates of Natural Gases"*, 2nd Marcel Dekker, Inc, New York, (1998)
4. Moridis G.J. and Collett T.S., *"Strategies for Gas Production From Hydrate accumulations Under Various Geologic Conditions"*, Report LBNL-52568, Lawrence Berkeley Natl. Laboratory, Berkeley, California (2003)
5. Holder G. and Angert P., *"Simulation of Gas Production from a Reservoir Containing both Gas and Free Natural Gas"*, SPE paper 11105 presented at the 57th SPE Annual Technical Conference and Exhibition in New Orleans, LA, September 26-29, (1982)
6. Burshears M., O'Brien T., and Malone R., *"A Multi-Phase, Multi-Dimensional, Variable Composition Simulation of Gas Production from a Conventional Gas Reservoir in Contact with Hydrates"*, SPE paper 15246 (1986)

7. Yousif M.H., Abass H.H., Selim M.S., and Sloan E.D, *"Experimental and Theoretical Investigation of Methane-Gas-Hydrate Dissociation in Porous Media"*, SPE paper 18320 (1991)
8. Chuang Ji, Goodarz Ahmadi, and Duane H. Smith, *"Natural Gas Production from Hydrate Decomposition by Depressurization",* Chemical Enigneering Science 56, pp. 5801-5814 (2001)
9. Sun X., Nanchary N., and Mohanty K.K., *"1-D Modeling of Hydrate Depressurization in Porous Media"*, Department of Chemical Engineering, University of Houston, Houston, Texas (2004)
10. Sun X. and Mohanty K.K., "*Simulation of Methane Hydrate Reservoirs*", University of Houston, SPE Paper 93015 (2005)
11. Moridis G.J., Kowalsky M.B., and Pruess K., "*Depressurization-Induced Gas Production from Class-1 Hydrate Deposits*", Lawrence Berkeley National Laboratory, University of Califrnia, SPE Paper 97266 (2005)
12. Hong H. and Pooladi-Darvis M., *"Simulation of Depressurization for Gas Production from Gas Hydrate Reservoir"*, University of Calagy, Journal of Canadian Petroleum Technology. vol. 44, pp. 39-46, November 2005.
13. Gerami S. and Pooladi-Darvis M., *"Material balance and Boundary-Dominated Flow Models for Hydrate-Capped Gas Reservoirs"*, University of Calgary, SPE Paper 102234 (2006)
14. Ozisic M.N., *"Heat Conduction"*, 2nd ed., John Wiley&Sons, Inc., (1993)

15. Phale H.A., Zhu T., White M.D., and McGrail B.P., *"Simulation Study on Injection of CO_2-Microemulsion for Methane Recovery from Gas-Hydrate Reservoirs"*, University of Alaska Fairbanks and Pacific Northwest Natl. Laboratory, SPE Paper 100541 (2006)
16. White M.D. and Oostrom M., *"STOMP-Subsurface Transport Over Multiple Phases"*, Version 3.0 User's Guide (2003)
17. Udding M., Alberta Research Council Inc., Coombe, D.A., Computer Modeling Group Ltd., Law, D.A., Schlumberger Reservoir Fluid Center, and Gunter, W.D., Alberta Research Council Inc., *"Numerical Studies of Gas-Hydrates Formation and Decomposition in a Geological Reservoir"*, SPE Paper 100460 (2006)
18. *http://www.pet.hw.ac.uk/research/hydrate/hydrates_what.html*
19. Van der Waals J.H. and Platteeuw J.C., *"Clathrate Solutions"*, Adv. In Chem. Phys., (1959), 2, 1-57
20. Holder G.D., Zetts S.P., Pradham N., "*Phase Behavior in Systems Containing Clathrate Hydrates"*, Rev. Chem. Eng. (1988)
21. Tarek Ahmed, *"Hydrocarbon Phase Behavior"*, Gulf Publishing Company, Houston, Texas, (1989)
22. Kamath V.A., *"Study of heat transfer characteristics during dissociation of gas hydrates in porous media"*, Ph.D. dissertation, University of Pittsburgh, Pittsburgh, PA (1984)
23. Makogon Y.F., *"Hydrates of Hydrocarbons"*, Penn Well, Tulsa, OK. (1997)

24. Moridis G.J., *"Numerical Studies of Gas Production From Methane Hydrates"*, Lawrence Berkeley National Laboratory, University of California, SPE Paper 75691 (2002)

25. Verma A., and Pruess K., Tsang C.F., and Witerspoon P.A., "*A Study of Two-Phase Concurrent Flow of Steam and Water in an Unconsolidated Porous Medium*", Proc 23rd National Heat Transfer Conference, Am. Society of Mechanical Engineers, Denver, CO, 135-143, (1985)

26. Xu T., Ontoy Y., Molling P., Spycher N., Parini M., and Pruess K., "*Reactive Transport Modeling of Injection Well Scaling and Acidizing at Tiwi Field, Philippines*", Geothermics, Vol.33, No.4, pp.477-491 (2004)

27. Somerton W.H., et al., *"Thermal Behavior of Unconsolidated Oil Sands"*, SPE Paper 4506 (1973)

28. Lee A. L., Gonzalez M. H., and Eakin B. E., *"The viscosity of Natural Gases"*, JPT, (1996)

29. *"Perry's chemical engineers' handbook"*, sixth edition, McGraw-Hill (1984)

30. Alp Doruk, *"Gas Production from Hydrate Reservoirs"*, Master Thesis, Middle East Technical University (2005)

31. Tassios D.P.,*"Applied Chemical Engineering Thermodynamics"*, Springer-Verlag (1993)

APPENDIX A

DERIVATION OF THE MOLAR BALANCE EQUATIION

Let us consider the elemental control volume (CV) in a rectangular coordinate system shown in Figure A-1. The control volume has a volume $\Delta x \Delta y \Delta z$, porosity ϕ, and permeabilities k_x, k_y, k_z in the x, y, and z directions, respectively. This control volume hosts up to two mobile phases (aqueous and free gas) and two immobile phases (gas hydrate and ice) at saturations S_a, S_g, S_h and S_i, respectively. Figure A-1 shows the molar flow rates for component *i*. Variable Q_i^* represents the external sink or source term of component *i*.

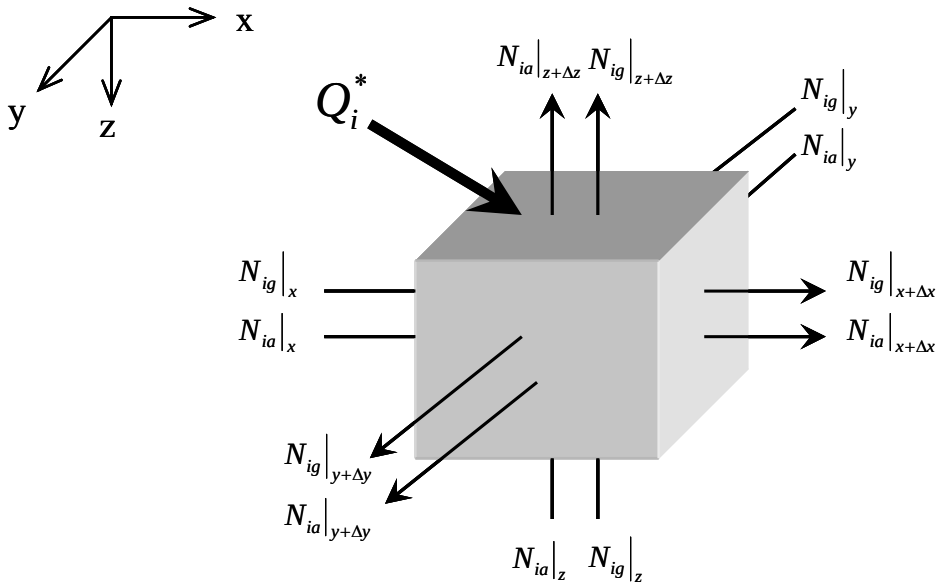

Figure A-1: Elementary control volume

The change in the amount of component *i* within the elementary volume is a results of fluid leaving and entering the elementary volume. Over a period of time Δt, one can writ the molar balance of the i^{th} component:

$$\begin{pmatrix} Moles\,of \\ component\ "i" \\ entering\,the\,CV \end{pmatrix} - \begin{pmatrix} Moles\,of \\ component\ "i" \\ leaving\,the\,CV \end{pmatrix} + \begin{pmatrix} Molar \\ Source/Sink\,of \\ component\ "i" \end{pmatrix} = \begin{pmatrix} Accumulation \\ of\ component\ "i" \\ from\ time\ t\ to\ \Delta t \end{pmatrix} \quad \text{A.1}$$

The units of each of the terms used in this derivation are lbmole/day. In this derivation, a positive sign is assigned to flow entering the elementary volume whereas a negative sign to flow leaving the elementary volume. Accordingly, the molar balance of component "*i*" can be written as:

$$-\left[\sum_{l=a,g}(N_{ilx})_{x+\Delta x}+\sum_{l=a,g}(N_{ily})_{y+\Delta y}+\sum_{l=a,g}(N_{ilz})_{z+\Delta z}\right]+\left[\sum_{l=a,g}(N_{ilx})_{x}+\sum_{l=a,g}(N_{ily})_{y}+\sum_{l=a,g}(N_{ilz})_{z}\right]$$
$$+\,Q_i^{*}=\Delta x\cdot\Delta y\cdot\Delta z\,\frac{\left[\phi\sum_{l=a,g,h}(S_lC_{il})\right]_{t+\Delta t}-\left[\phi\sum_{l=a,g,h}(S_lC_{il})\right]_{t}}{\Delta t} \quad \text{A.2}$$

Here, $(N_{ils})_s$ is the number of mole of component "*i*" in "*l*" phase entering the elementary volume in the s direction at position "*s*" and $(N_{ils})_{s+\Delta s}$ is the number of mole of component "*i*" in "*l*" phase leaving the elementary volume in the s direction at position "$s+\Delta s$".

The molar flow of the i^{th} component is a function of velocity of the phase, the concentration of the component in the phase, and the area perpendicular to the flow as the following expression:

$$N_{ils}\big|_{s=x,y,z}=C_l\,x_{il}\,v_{ls}\big|_{s=x,y,z}\,A_s\big|_{s=x,y,z}$$
$$N_{ils}\big|_{s=x+\Delta x,y+\Delta y,z+\Delta z}=C_l\,x_{il}\,v_{ls}\big|_{s=x+\Delta x,y+\Delta y,z+\Delta z}\,A_s\big|_{s=x+\Delta x,y+\Delta y,z+\Delta z} \quad \text{A.3}$$

where: v_{ls} is superficial velocities of the "*l*" phase in the "*s*" direction

C_l is concentration of the "*l*" phase

x_{il} is the mole fraction of the i^{th} component in the "*l*" phase

A_s is the area perpendicular to the flow in the "*s*" direction, therefore,

$$A_x = \Delta y \cdot \Delta z;\ A_y = \Delta x \cdot \Delta z;\ and\ A_z = \Delta x \cdot \Delta y \qquad \text{A.4}$$

Substitution equation (A.3) into equation (A.2) gives,

$$\begin{aligned} &-\left[\Big(\sum_{l=a,g} (C_l\, x_{il}\, v_{lx}\, A_x)_{x+\Delta x} - \sum_{l=a,g} (C_l\, x_{il}\, v_{lx}\, A_x)_x \right] \frac{\Delta x}{\Delta x} \\ &-\left[\Big(\sum_{l=a,g} (C_l\, x_{il}\, v_{ly}\, A_y)_{y+\Delta y} - \sum_{l=a,g} (C_l\, x_{il}\, v_{ly}\, A_y)_y \right] \frac{\Delta y}{\Delta y} \\ &-\left[\Big(\sum_{l=a,g} (C_l\, x_{il}\, v_{lz}\, A_z)_{z+\Delta z} - \sum_{l=a,g} (C_l\, x_{il}\, v_{lz}\, A_z)_z \right] \frac{\Delta z}{\Delta z} \\ &+ Q_i^* = V_b \frac{\left[\phi \sum_{l=a,g,h} (S_l x_{il} C_l) \right]_{t+\Delta t} - \left[\phi \sum_{l=a,g,h} (S_l x_{il} C_l) \right]_t}{\Delta t} \end{aligned} \qquad \text{A.5}$$

Diving equation (A.5) by ΔxΔyΔz and then taking the limits of *Δx, Δy, Δz, and Δt* approach zeroes yields:

$$\begin{aligned} &-\frac{\partial}{\partial x}\left[\sum_{l=a,g} \left(C_l\, x_{il}\, v_{lx}\, A_x\right) \right] \Delta x - \frac{\partial}{\partial y}\left[\sum_{l=a,g} \left(C_l\, x_{il}\, v_{ly}\, A_y\right) \right] \Delta y - \frac{\partial}{\partial z}\left[\sum_{l=a,g} \left(C_l\, x_{il}\, v_{lz}\, A_z\right) \right] \Delta z \\ &+ Q_i^* = V_b \frac{\partial}{\partial t}\left(\phi \sum_{l=a,g,h} (S_l x_{il} C_l) \right) \end{aligned} \qquad \text{A.6}$$

The fluid flow mechanic in porous media can be described by Darcy's law as shown in the following equation:

$$v_{ls} = -5.615 \frac{k_s k_{rl}}{\mu_l} \frac{\partial \Phi_l}{\partial s} \qquad \text{A.7}$$

where k_s is the absolute permeability in the "s" direction

k_{rl} is the relative permeability to the "*l*" phase

μ_l is the viscosity of the "*l*" phase

Φ_l is the flow potential of the "*l*" phase

The value of C_l can be calculated from:

$$C_l = \frac{\rho_l}{MW_l} = \overline{\rho}_l \qquad \text{A.8}$$

where $\overline{\rho}_l$ is molar density of the "*l*" phase

Substitution of equation (A.7) into equation (A.6) yields:

$$\frac{\partial}{\partial x}\left[\sum_{l=a,g}\left(\frac{x_{il}\,\overline{\rho}_l\,A_x k_x k_{rl}}{\mu_l}\frac{\partial\Phi_l}{\partial x}\right)\right]\Delta x+\frac{\partial}{\partial y}\left[\sum_{l=a,g}\left(\frac{x_{il}\,\overline{\rho}_l\,A_y k_y k_{rl}}{\mu_l}\frac{\partial\Phi_l}{\partial y}\right)\right]\Delta y$$
$$-\frac{\partial}{\partial z}\left[\frac{x_{il}\,\overline{\rho}_l\,A_z k_z k_{rl}}{\mu_l}\frac{\partial\Phi_l}{\partial z}\right]\Delta z+\frac{Q_i^*}{5.615}=\frac{V_b}{5.615}\frac{\partial}{\partial t}\left(\phi\sum_{l=a,g,h}(S_l x_{il}\overline{\rho}_l)\right) \qquad \text{A.9}$$

Equation (A.9) is the general compositional mole balance equation. The mole balance equations for methane and water components can be written as:

Methane:

$$\frac{\partial}{\partial x}\left[y_m\overline{\rho}_g\frac{A_x k_x k_{rg}}{\mu_g}\left(\frac{\partial\Phi_g}{\partial x}\right)+x_m\overline{\rho}_a\frac{A_x k_x k_{ra}}{\mu_a}\left(\frac{\partial\Phi_a}{\partial x}\right)\right]\Delta x$$
$$+\frac{\partial}{\partial y}\left[y_m\overline{\rho}_g\frac{A_y k_y k_{rg}}{\mu_g}\left(\frac{\partial\Phi_g}{\partial y}\right)+x_m\overline{\rho}_a\frac{A_y k_y k_{ra}}{\mu_a}\left(\frac{\partial\Phi_a}{\partial y}\right)\right]\Delta y$$
$$+\frac{\partial}{\partial z}\left[y_m\overline{\rho}_g\frac{A_z k_z k_{rg}}{\mu_g}\left(\frac{\partial\Phi_g}{\partial z}\right)+x_m\overline{\rho}_a\frac{A_z k_z k_{ra}}{\mu_a}\left(\frac{\partial\Phi_a}{\partial z}\right)\right]\Delta z+\frac{Q_m}{5.615}$$
$$=\left(\frac{V_b}{5.615}\right)\frac{\partial}{\partial t}\left(y_m\phi S_g\overline{\rho}_g+x_m\phi S_a\overline{\rho}_a+N_m\phi S_H\overline{\rho}_H\right) \qquad \text{A.10}$$

Water:

$$\frac{\partial}{\partial x}\left[(1-y_m)\,\overline{\rho}_g\,\frac{A_x k_x k_{rg}}{\mu_g}\left(\frac{\partial \Phi_g}{\partial x}\right)+(1-x_m)\,\overline{\rho}_a\,\frac{A_x k_x k_{ra}}{\mu_a}\left(\frac{\partial \Phi_a}{\partial x}\right)\right]\Delta x$$
$$+\frac{\partial}{\partial y}\left[(1-y_m)\,\overline{\rho}_g\,\frac{A_y k_y k_{rg}}{\mu_g}\left(\frac{\partial \Phi_g}{\partial y}\right)+(1-x_m)\,\overline{\rho}_a\,\frac{A_y k_y k_{ra}}{\mu_a}\left(\frac{\partial \Phi_a}{\partial y}\right)\right]\Delta y$$
$$+\frac{\partial}{\partial z}\left[(1-y_m)\,\overline{\rho}_g\,\frac{A_z k_z k_{rg}}{\mu_g}\left(\frac{\partial \Phi_g}{\partial z}\right)+(1-x_m)\,\overline{\rho}_a\,\frac{A_z k_z k_{ra}}{\mu_a}\left(\frac{\partial \Phi_a}{\partial z}\right)\right]\Delta z+\frac{Q_w}{5.615}$$
$$=\left(\frac{V_b}{5.615}\right)\frac{\partial}{\partial t}\left((1-y_m)\,\phi S_g\overline{\rho}_g+(1-x_m)\,\phi S_a\overline{\rho}_a+\phi S_I\overline{\rho}_I+N_w\phi S_H\overline{\rho}_H\right) \qquad \text{A.11}$$

where x_m is the mole fraction of methane in aqueous phase

y_m is the mole fraction of methane in free-gas phase

N_w is the number of water molecule in methane hydrate crystal ($N_w = 46$)

N_m is the number of methane molecule in methane hydrate crystal (N_m = 6-8)

APPENDIX B

COMPARISONS OF THE SIMULATION RESULTS FOR A CONVENTIONAL GAS RESERVOIR

In this section, the simulation results (for a conventional gas system) from the model developed in this work are compared with the results from a commercial reservoir simulator (CMG) for validating the developed model.

The developed model is used for simulating the gas production from a two-dimensional, homogeneous, isotropic reservoir with a production well located at the center of the reservoir as shown in Figure B-1 and the reservoir properties are shown in Table B-1.

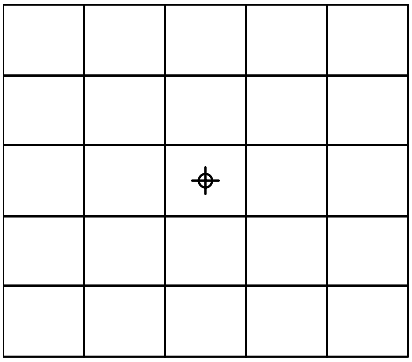

Figure AB-1: Reservoir structure for model verification

Table B-1: Reservoir and grid block properties for model validation

Reservoir porosity	0.2
Top depth (ft)	1,000
Reservoir thickness (ft)	100
dx, dy (ft)	500
k_x,k_y (md)	100
Initial Pressure (psi)	800
Initial water saturation	0.6
Reservoir temperature (^oF)	40
Well bore radius (ft)	0.25

The comparison for the isothermal system between the results from the model and commercial simulator of various well specification values are shown in Figure B-2 to Figure B-4.

The comparisons show the very good matches of the results from the developed model and the commercial simulator. It indicates the robustness of the simulator developed in this study.

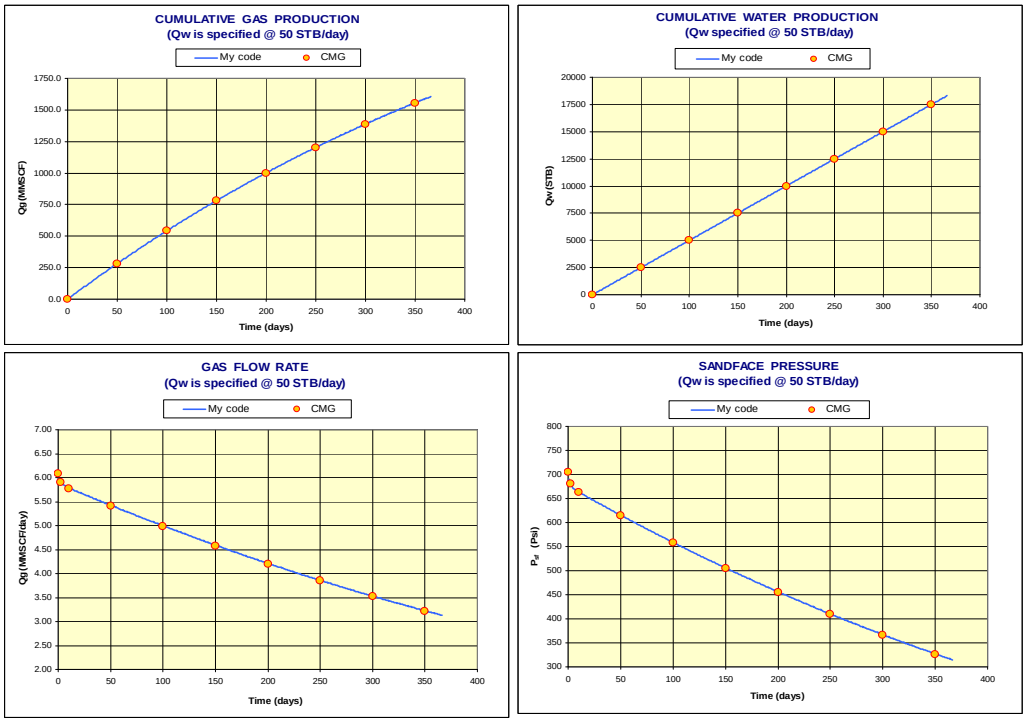

Figure B-2: The comparison when water flow rate was specified at 50 STB/day

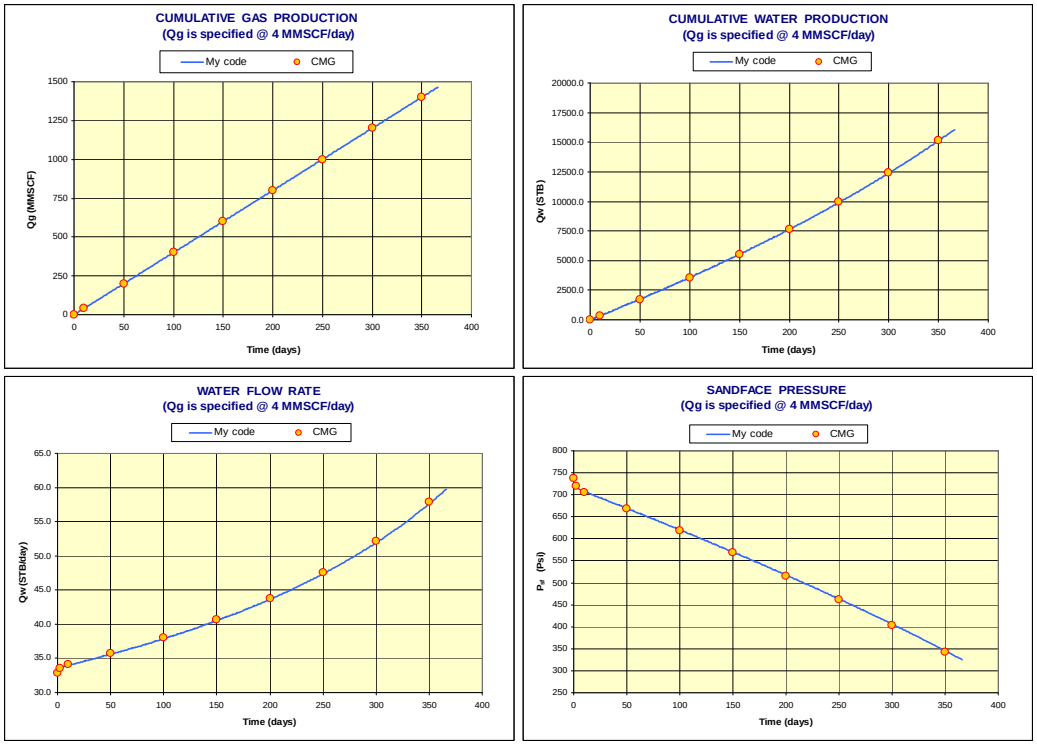

Figure B-3: The comparison when gas flow rate was specified at 4 MMSCF/day

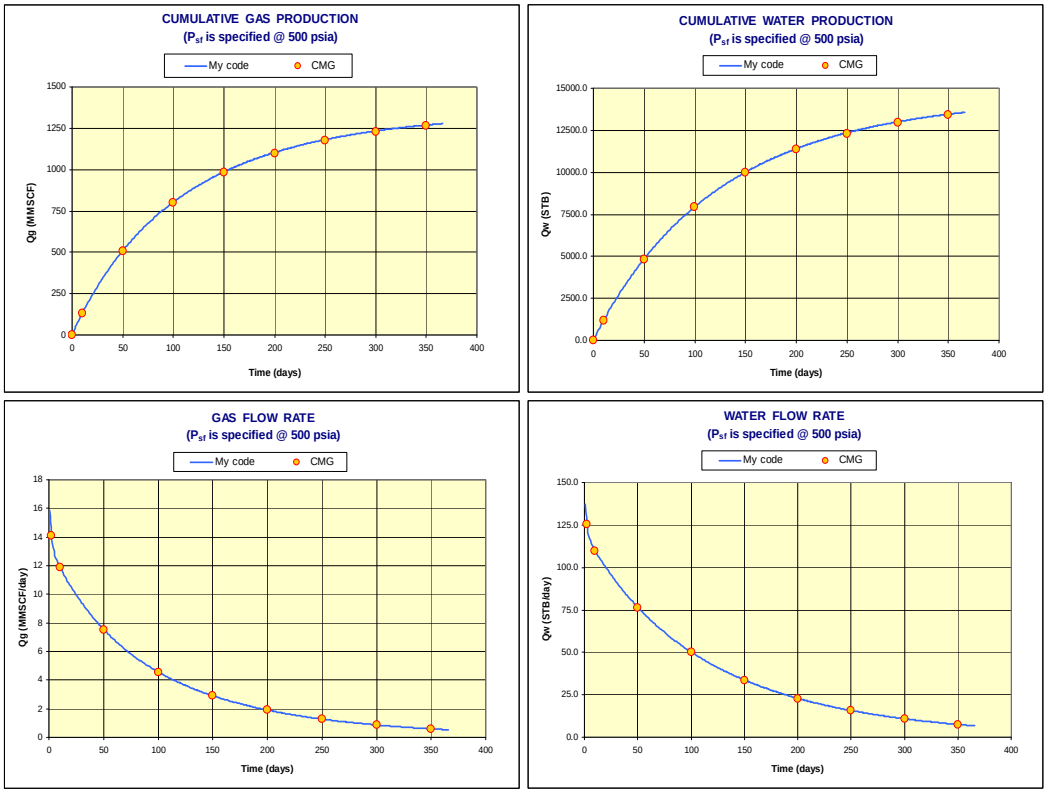

Figure B-4: The comparison when sand face pressure was specified at 500 psia

VITA

SUNTICHAI SILPNGARMLERT

Personal Information

Birth Date: August 12, 1974

Birth Place: Bangkok, Thailand

E-mail: ssilpngarmlert@yahoo.com, szs160@psu.edu

Education

2003–2007

Ph.D., Petroleum and Natural Gas Engineering
The Pennsylvania State University, University Park, PA, U.S.A.
Thesis: *"Numerical Modeling of Gas Recovery from Methane Hydrate Reservoirs "*
G.P.A. 3.81/4.0

1997–1999

M.S., Chemical Engineering (International program in collaboration with MIT)
King's Mongkut University of Technology Thonburi, Bangkok, Thailand
Thesis: *"The Development of the Computational Engine for Air Pollution Model on Cluster Computer"*
G.P.A. 3.66/4.0

1993–1996

B.Eng., Chemical Engineering (Second Class Honor)
Kasetsart University, Bangkok, Thailand
G.P.A. 3.40/4.0

Honors & Activities

- Research Assistantship at the Pennsylvania State University, PA, USA. (2003-present)
- Member of the Society of Petroleum Engineers (2003 – present)
- Recipient of the National Science and Technology Development Agency Scholarship (1997 – 1999)